

---

# Applied Research Laboratory

## Technical Report

### **Advanced Antennas Enabled By Electromagnetic Metamaterials**

by

Clinton P. Scarborough, Dr. Douglas H.  
Werner and Dr. Douglas E. Wolfe

Approved for public release, distribution unlimited.

# PENNSTATE

---



**The Pennsylvania State University  
The Applied Research Laboratory  
P.O. Box 30  
State College, PA 16804**

**Advanced Antennas Enabled By Electromagnetic Metamaterials**

By  
Clinton P. Scarborough and Dr. Douglas E. Wolfe

Technical Report No. TR 14-009  
December 2014

Supported By:

Penn State Applied Research Laboratory, Exploratory and Foundational Research Program

Approved for public release, distribution unlimited

20151210102

REPORT DOCUMENTATION PAGE				Form Approved OMB No. 0704-0188	
<small>The public reporting burden for this collection of information is estimated to average 1 hour per response, including the time for reviewing instructions, searching existing data sources, gathering and maintaining the data needed, and completing and reviewing the collection of information. Send comments regarding this burden estimate or any other aspect of this collection of information, including suggestions for reducing the burden, to the Department of Defense, Executive Service Directorate (0704-0188). Respondents should be aware that notwithstanding any other provision of law, no person shall be subject to any penalty for failing to comply with a collection of information if it does not display a currently valid OMB control number.</small> <b>PLEASE DO NOT RETURN YOUR FORM TO THE ABOVE ORGANIZATION.</b>					
1. REPORT DATE (DD-MM-YYYY) 06-18-15		2. REPORT TYPE Technical Report		3. DATES COVERED (From - To) December 14-June 2015	
4. TITLE AND SUBTITLE Advanced Antennas Enabled By Electromagnetic Metamaterials				5a. CONTRACT NUMBER	
				5b. GRANT NUMBER	
				5c. PROGRAM ELEMENT NUMBER	
6. AUTHOR(S) Clinton P. Scarborough Douglas E. Wolfe				5d. PROJECT NUMBER	
				5e. TASK NUMBER	
				5f. WORK UNIT NUMBER	
7. PERFORMING ORGANIZATION NAME(S) AND ADDRESS(ES) Applied Research Laboratory The Pennsylvania State University PO Box 30 State College, PA 16804				8. PERFORMING ORGANIZATION REPORT NUMBER  TR 14-009	
9. SPONSORING/MONITORING AGENCY NAME(S) AND ADDRESS(ES) Defense Advance Research Projects Agency Tactical Technology Office 675 N. Randolph Street Arlington, VA 22203-2114 Attn: Kevin Massey				10. SPONSOR/MONITOR'S ACRONYM(S)  DARPA	
				11. SPONSOR/MONITOR'S REPORT NUMBER(S)	
12. DISTRIBUTION/AVAILABILITY STATEMENT Approved for Public Release: distribution unlimited					
13. SUPPLEMENTARY NOTES					
14. ABSTRACT See attached					
15. SUBJECT TERMS					
16. SECURITY CLASSIFICATION OF:			17. LIMITATION OF ABSTRACT  UU	18. NUMBER OF PAGES  132	19a. NAME OF RESPONSIBLE PERSON Douglas E. Wolfe
a. REPORT Unclassified	b. ABSTRACT Unclassified	c. THIS PAGE Unclassified			19b. TELEPHONE NUMBER (Include area code) 814-865-0316

The Pennsylvania State University  
The Graduate School

ADVANCED ANTENNAS ENABLED  
BY ELECTROMAGNETIC METAMATERIALS

A Dissertation in  
Electrical Engineering  
by  
Clinton Post Scarborough

© 2014 Clinton Post Scarborough

Submitted in Partial Fulfillment  
of the Requirements  
for the Degree of

Doctor of Philosophy

December 2014

Approved for public release; distribution unlimited



The dissertation of Clinton Post Scarborough was reviewed and approved\* by the following:

Douglas H. Werner  
Professor of Electrical Engineering  
Dissertation Advisor

Pingjuan L. Werner  
Professor of Electrical Engineering

Julio V. Urbina  
Professor of Electrical Engineering

Douglas E. Wolfe  
Associate Professor of Material Science and Engineering

Kultegin Aydin  
Professor of Electrical Engineering  
Department Chair

\*Signatures are on file in the Graduate School.

# Abstract

Much attention has been given to electromagnetic metamaterials over the past decade, as researchers have investigated promises of invisibility cloaks and flat lenses, along with other dramatic claims. More recent work has focused on improving existing devices by employing metamaterials in their design and construction. These recent efforts have begun to show truly practical applications of metamaterials in real-world devices, giving such benefits as increased operating bandwidth and reduced weight. Specifically, metamaterial surfaces, or “metasurfaces” show great promise in improving the performance of radio-frequency (RF) and microwave antennas.

Properly designed metasurfaces can be included as liners for horn antennas to support hybrid modes, which yield rotationally symmetric radiation patterns with minimal cross-polarization. Such radiation characteristics are desirable for satellite reflector antennas, where reducing the size and weight of antennas corresponds to a dramatic reduction in costs. These satellite antennas often use separate polarizations as separate communication channels, effectively providing nearly double the communications data bandwidth through a single antenna. Traditionally, corrugated horns provide low cross-polarization, but they are very expensive to manufacture and are very heavy. Here we show a conical horn antenna with metamaterial liners operating over an octave bandwidth including the  $K_u$ -band with cross-polarization better than  $-30$  dB. The metamaterials add virtually no loss to the horn, while exceeding the bandwidth of a corrugated horn and requiring a fraction of the weight. To achieve this excellent performance, we developed the metamaterial surface designs, mode analyses for circular metasurface-lined waveguides, as well as an analysis of metahorns with various methods for tapering the inhomogeneous metamaterial properties along the length of the horns.

The second antenna herein developed employs metamaterials for miniaturization while providing comparable performance to much larger existing antennas.

Conventionally, efficient antennas operating over more than a few percent bandwidth require dimensions approaching a wavelength or more. In the low UHF band, such antennas will have sizes on the order of a meter. Artificial magnetic conducting (AMC) substrates have been shown to reduce the height profile of these antennas, but at the expense of operating bandwidth. Adding tunability has restored the flexibility of dynamically adjusting the communication channel over a wide range, but the lateral dimensions of the antenna are still quite large. Here we introduce a miniaturized low-profile antenna system based on a tunable AMC substrate beneath a tunable small antenna element - specifically, crossed end-loaded dipoles. This system allows a channel bandwidth of a few percent with the flexibility of adjusting this channel over a range including 220 MHz to 270 MHz, all while using an antenna element that is still only a fraction of a wavelength in its largest dimension. In addition, the tunable end-loaded dipoles allow dynamic control of the antenna's polarization, allowing near arbitrary polarization control without the need for expensive phase shifters or complex feeding circuitry. While previous work has achieved several of these characteristics in isolation, we have achieved all of them from the combination of tunable AMC surfaces with a miniaturized unit cell and electrically-tunable crossed end-loaded dipoles with near-arbitrary polarization control. Measurements of a prototype showed excellent results. Since the antenna is nearly entirely based on standard printed circuit board manufacturing techniques with relatively inexpensive components, it promises to be an eminently practical antenna for vehicular and airborne applications requiring low-profile antennas for satellite connectivity.

# Table of Contents

List of Figures	viii
Acknowledgments	xv
Chapter 1	
A Brief History of Radio-Frequency Electromagnetic Metamaterials	1
1.1 Metamaterials . . . . .	1
1.2 Precursors to Metamaterials and Related Work . . . . .	2
1.3 Early Work with Metamaterials . . . . .	2
1.4 Where We Are Now . . . . .	3
1.5 Original Contributions . . . . .	3
1.5.1 Metamaterial Coatings for Hybrid-Mode Horn Antennas . . .	4
1.5.2 Miniaturized Tunable Low-Profile Antenna with an AMC Substrate . . . . .	4
Chapter 2	
Inhomogeneous Metamaterial Coatings for Lightweight, Broad-band Hybrid-Mode Horn Antennas	5
2.1 Metamaterial Surfaces . . . . .	5
2.2 Introduction to Hybrid-Mode Horn Antennas . . . . .	6
2.3 Soft and Hard Surfaces and Horns . . . . .	7
2.4 Design of Inhomogeneous Metasurfaces . . . . .	8
2.5 Metasurfaces Coating a Cylindrical Waveguide . . . . .	11
2.6 Metamaterial Horns with Homogeneous Metasurface Liners . . . . .	13
2.7 Metamaterial Horns with Spatially Tapering Liners . . . . .	17
2.8 Summary . . . . .	24

<b>Chapter 3</b>	
<b>Near-Arbitrary Polarization from Tunable Crossed End-Loaded Dipoles</b>	<b>26</b>
3.1 Introduction . . . . .	26
3.2 Preliminary Work . . . . .	27
3.3 Antenna Geometry . . . . .	35
3.4 Impedance Characteristics of End-Loaded Dipoles . . . . .	35
3.5 Polarization Characteristics of Crossed End-Loaded Dipoles . . . . .	39
3.6 Summary . . . . .	42
<b>Chapter 4</b>	
<b>Compact Low-Profile Tunable Metamaterial Antenna with Near-Arbitrary Polarization</b>	<b>46</b>
4.1 Introduction . . . . .	46
4.2 Preliminary Work . . . . .	47
4.2.1 Initial AMC Design . . . . .	47
4.2.2 Tunable End-Loaded Dipole (ELD) . . . . .	48
4.3 Final Antenna Geometry . . . . .	49
4.4 Simulated AMC Performance . . . . .	54
4.5 Simulated Antenna Performance . . . . .	57
4.5.1 AMC Tolerance Analysis . . . . .	57
4.5.2 Simulated Radiation Characteristics . . . . .	60
4.6 Measured Antenna Performance . . . . .	65
4.7 Summary . . . . .	72
<b>Chapter 5</b>	
<b>Antenna Testing with Satellite Carrier Signals</b>	<b>75</b>
5.1 Initial Reception Testing . . . . .	75
5.2 Bias Voltage Controlling Circuit . . . . .	76
5.2.1 Circuit Design . . . . .	76
5.2.2 Source Code Listing . . . . .	82
main.c . . . . .	82
5.3 Testing on a Combatant Craft Assault . . . . .	89
<b>Chapter 6</b>	
<b>Conclusions and Future Work</b>	<b>91</b>
6.1 Conclusions . . . . .	91
6.2 Future Work . . . . .	92
6.2.1 Inhomogeneous Liners for Horn Antennas . . . . .	92
6.2.2 Compact Tunable Metamaterial Antenna . . . . .	92

6.2.2.1	Power Handling . . . . .	92
6.2.2.2	Tuning Improvements . . . . .	93
6.2.2.3	Structural/Mechanical Evaluations . . . . .	93
6.2.2.4	Redesign for Additional Considerations . . . . .	93
<b>Appendix A</b>		
	<b>AMC Metamaterial Prototype Fabrication</b>	<b>94</b>
<b>Appendix B</b>		
	<b>Crossed ELD Antenna Characterization</b>	<b>105</b>
<b>Appendix C</b>		
	<b>Metamaterial Antenna Characterization</b>	<b>110</b>
<b>References</b>		<b>122</b>
<b>Publications</b>		<b>129</b>

# List of Figures

2.1	(a) The geometry of a soft metasurface composed of metallic patches and wires (yellow). The effective properties of the metasurfaces were characterized with a plane wave at near grazing incidence ( $80^\circ$ from broadside) in the y-z plane. (b) Normalized surface reactance of metasurfaces with patches of width $w = 2.0$ mm and varying length $l$ . (c) Normalized surface reactance of metasurfaces with patches of length $l = 2.3$ mm and varying width $w$ . The other dimensions of the metasurfaces are $t = 5.2$ mm, $s = 0.4$ mm, and $p = 3$ mm. . . . .	10
2.2	(a) The schematic of one section of metasurface inside the straight waveguide of a metahorn. The periodicity of the metasurface structure along the wave propagation direction ( $\hat{\beta}$ ) is $p = 3$ mm. The outer and inner boundaries of the metasurface liner have diameters of $D_1 = 30.4$ mm and $D_2 = 20.0$ mm, respectively. (b) The dispersion diagrams of circular waveguides containing metasurfaces with different dimensions. The dispersion of a circular waveguide with a diameter of 20 mm (dashed, pink) is shown as a reference. The light line is indicated by the dash-dotted black line. (c) The electric-field mode patterns of the three circular waveguides coated with metasurfaces at 12 GHz. . . . .	12
2.3	The interior view of a metahorn antenna with homogeneous metasurface liners covering both the flared horn section and the straight waveguide section. The metahorn is fed by a circular waveguide with a diameter of 20 mm. . . . .	14
2.4	$S_{11}$ for three soft horn antennas composed of homogeneous metasurface liners with varying patch dimensions. . . . .	15

2.5	Peak relative cross-polarized radiation with respect to the maximum co-polarized field in the radiation patterns of a conical horn antenna and three soft horns with various homogeneous metasurface liners. The maximum cross-polarization level was evaluated at a $45^\circ$ $\phi$ -plane cut where the metahorn exhibits the highest cross-polarized radiation. The relative cross-polarization of a conventional conical horn with the same dimensions (dash-dotted, purple) is shown as a reference. . . . .	16
2.6	(a) The interior view of a metahorn antenna with inhomogeneous metasurface liners covering both the flared horn section and the straight waveguide section. The metahorn is fed by a circular waveguide with a diameter of 20 mm. (b) The sizes of the metallic patches at each row of the metasurface in the flared horn section. Both the length and width of the patches follow an exponentially decaying function and decrease in size towards the aperture of the metahorn. . . . .	18
2.7	Calculated $S_{11}$ of the soft metahorn antenna with inhomogeneous metasurface liners. . . . .	19
2.8	Peak relative cross-polarized radiation with respect to the maximum co-polarized field in the radiation patterns of the soft metahorn with inhomogeneous metasurface liners. The maximum cross-polarization level was evaluated at a $45^\circ$ $\phi$ -plane cut where the metahorn exhibits the highest cross-polarized radiation. The relative cross-polarization of a conical corrugated horn with the same dimensions (dash-dotted, purple) is shown as a reference. . . . .	20
2.9	Simulated E-plane, H-plane, and $45^\circ$ $\phi$ -plane cut co- and cross-polarized radiation patterns of the soft metahorn with inhomogeneous metasurface liners at various frequencies across the band. Note that the copolarized patterns are approximately identical in both planes within the main beam, producing radiation patterns that are nearly independent of polarization. . . . .	21
2.10	Peak relative sidelobe level with respect to the maximum copolarized field in the radiation patterns of the soft metahorn with inhomogeneous metasurface liners. The $E$ -plane relative sidelobe level of a conventional conical horn and a corrugated horn with the same dimensions (dashed, red and dash-dotted, purple) are shown for comparison. . . . .	22



2.11	(a) Calculated co-polarized electric field distributions at the aperture of the soft metahorn with inhomogeneous metasurface liners at 10 and 20 GHz. The fields are tapered towards zero at the wall of the metahorn because of the soft metasurface coatings. (b) Calculated co-polarized electric field distributions at the aperture of a conventional conical horn. (c) Calculated copolarized electric field distributions at the aperture of a corrugated horn. . . . .	23
2.12	Calculated (a) $S_{11}$ and (b) peak relative cross-polarized radiation of soft metahorn antennas with semi-flare angles of $10^\circ$ , $12.3^\circ$ and $15^\circ$ , respectively. . . . .	25
3.1	Geometry of the preliminary crossed ELD design. The trace width is 0.100" and the substrate is 0.050" thick Rogers 5880LZ, which has a dielectric constant of 1.96. . . . .	27
3.2	Input admittance of an ELD with varying tuning capacitance. Note that at the two marked capacitances, there is a $90^\circ$ phase difference but identical real parts. . . . .	28
3.3	Realized gain for three different tuning capacitor configurations. The red curve is the total gain, purple is the left-hand circularly-polarized (LHCP) gain, and blue is the desired right-hand circularly-polarized (RHCP) gain. The ELD achieves 1 dB of realized gain from a circularly-polarized beam with instantaneous bandwidths of approximately 1% over a total tunable bandwidth of more than 25%. (a) $C_1 = 8.5$ pF, $C_2 = 20$ pF (b) $C_1 = 2.64$ pF, $C_2 = 3.85$ pF (c) $C_1 = 0.83$ pF, $C_2 = 1.13$ pF . . . . .	29
3.4	Input reflection coefficient $S_{11}$ for the three configurations shown in Fig. 3.3. Note that, at the respective operating frequencies, $ S_{11} $ is below $-15$ dB across the entire tunable range. . . . .	30
3.5	Printed circuit board layout for the ELD prototype (a), including connection pads for the RF transformer at the feed point (b) and for the inductors as RF chokes (c) to connect a DC bias to the end-loads (for tuning the varactors). . . . .	32
3.6	(a) Photograph of the initial crossed-ELD prototype above a 24 in. square cavity. (b) Close-up view of the crossed ELDs. (c) Measured antenna input reflection coefficient (solid) compared to the simulated reflection coefficient for the antenna 6 in. above the cavity. (d) Measured antenna input reflection coefficient (solid) compared to the simulated reflection coefficient for the antenna 8 in. above the cavity. . . . .	33

3.7	Geometry (top) and simulated results (bottom) to reduce power flow to the DC biasing lines from the ELDs. Various combinations of series inductance $L$ and shunt-to-ground capacitance $C$ are shown.	34
3.8	End-loaded dipole geometry and photograph of the prototype. Top: Detailed dimensions of partial dipole with meandered end-load. Bottom: Photograph of the prototype and remaining dimensions. The dipoles consist of 1 oz. copper traces on a 0.020 in. thick FR4 substrate.	36
3.9	Top: Simulated antenna input reflection coefficient $S_{11}$ versus tuning capacitance for various frequencies. Bottom: Simulated antenna input impedance magnitude and phase at representative frequencies.	38
3.10	$S$ -parameter measurements of a Skyworks SMV1265 varactor diode. (a) Photographs of the test board, including the calibration standards. (b) Varactor capacitance as a function of reverse bias voltage, taken from the varactor datasheet. (c)-(f) Magnitude and phase of the reflection and transmission coefficients for the measured varactor (solid) and ideal capacitor with capacitance determined by the curve in (b).	40
3.11	$S$ -parameter measurements of an Infineon BB857 varactor diode. (a) Photographs of the test board, including the calibration standards. (b) Varactor capacitance as a function of reverse bias voltage, taken from the varactor datasheet. (c)-(f) Magnitude and phase of the reflection and transmission coefficients for the measured varactor (solid) and ideal capacitor with capacitance determined by the curve in (b).	41
3.12	Simulated reflection coefficient for the crossed ELDs with ideal capacitors (solid) and measured Skyworks SMV1265 varactor properties (dashed).	42
3.13	Top: Measured boresight antenna realized gain versus frequency for representative tuning configurations. Solid curves represent the left-handed circular component while dashed curves represent the right-handed component. Bottom: Measured boresight axial ratio versus frequency for various tuning configurations. Colored curves correspond to their counterparts above.	43
3.14	Top: Realized gain pattern at 250 MHz for various azimuth angles. Bottom: Axial ratio pattern at 250 MHz for various azimuth angles.	44
4.1	Initial AMC unit cell structure and dimensions. The unit cell consists of a patterned copper layer with vias through a Rogers 5880LZ substrate to a conducting ground plane.	48

4.2	Simulated AMC tuning performance as the varactor capacitance changes from 2 to 18 pF. Reflection coefficient (a) phase and (b) magnitude. The AMC channel can be tuned from approximately 150 to 435 MHz with instantaneous bandwidths ( $\pm 45^\circ$ ) ranging from 2 to 17 MHz (1.3-3.9%). Absorption becomes quite significant at the lower frequencies, but more than half of the incident power is reflected above about 250 MHz. . . . .	49
4.3	End-loaded dipole (ELD) geometry when placed over a small section of a perfect magnetic conductor (PMC) embedded in a larger section of a perfect electric conductor (PEC). The entire ground plane is about 50 cm across. . . . .	50
4.4	Simulation results corresponding to the geometry in Fig. 4.3. (a) Radiation pattern. The pattern is very similar in the absence of the PEC. (b) Reflection coefficient magnitude with tuning. As the varactors are tuned from 1 to 10 pF, the operating frequency shifts from over 400 MHz down close to 300 MHz. These curves assume that a matching network can transform from a standard transmission line to an impedance with a real part around 15-20 $\Omega$ . . . . .	50
4.5	Antenna geometry and photographs. (a)-(b) Overview dimensions of the antenna. While the thickness from the ground plane to the ELDs is 4 cm, the total antenna thickness approaches 4.5 cm when including circuit components on both the top and bottom circuit boards. (c)-(d) Photographs of details of the tunable AMC. . . . .	52
4.6	Detailed dimensions of the ELD (top) and AMC unit cell pattern (bottom). The AMC pattern was initially designed as a 32 pixel square unit cell, but the corners were beveled and the capacitor connection pads sized appropriately for manufacturing, as shown. The blue patches represent the locations of the tunable capacitors (varactor diodes). . . . .	53
4.7	Simulated AMC unit cell reflection phase (top) and magnitude (bottom) for various tuning capacitance values and various total thicknesses of the structure. The AMC can be tuned to operate over a range of one to two octaves, depending on its total thickness. The various tuning capacitance values are represented by various line styles and colors, while the curves for the various thicknesses have varying shadings. . . . .	55
4.8	Geometry (top) and simulated results (bottom) of a set of four unit cells including the biasing ground planes. . . . .	56

4.9	Model view showing the imperfect symmetry in the HFSS impedance simulations; the diagonal black lines correspond to the symmetry planes. This view shows the ELDs atop a 24" square AMC so that the AMC is visible. . . . .	58
4.10	Simulated antenna input impedance magnitude (top) and phase (bottom) versus ELD tuning capacitance at representative frequencies and their respective AMC tuning capacitances. . . . .	59
4.11	ELD input reflection coefficient (a, c, and e) and input admittance (b, d, and f) versus ELD tuning capacitance for ten random configurations with tolerances of 2% (a-b), 5% (c-d), and 10% (e-f). These curves are all for a frequency of 235 MHz, with a nominal AMC capacitance of 1.76 pF. . . . .	61
4.12	ELD input reflection coefficient (a, c, and e) and input admittance (b, d, and f) versus ELD tuning capacitance for ten random configurations with tolerances of 2% (a-b), 5% (c-d), and 10% (e-f). These curves are all for a frequency of 255 MHz, with a nominal AMC capacitance of 1.31 pF. . . . .	62
4.13	ELD input reflection coefficient (a, c, and e) and input admittance (b, d, and f) versus ELD tuning capacitance for ten random configurations with tolerances of 2% (a-b), 5% (c-d), and 10% (e-f). These curves are all for a frequency of 275 MHz, with a nominal AMC capacitance of 0.94 pF. . . . .	63
4.14	Skyworks SMV1265 varactor diode tuning characteristics. Capacitance versus bias voltage (top) and percent capacitance change versus change in bias voltage (bottom). . . . .	64
4.15	Simulated antenna left-hand circular polarized (solid) and right-hand circular polarized (dashed) realized gain versus zenith angle $\theta$ for azimuth angles in 45° increments at 250 MHz (top). Simulated axial ratio versus zenith angle $\theta$ (bottom). The breaks in the curves at $\theta = 90^\circ$ are an artifact of the use of the Green's function for the dielectrics in the simulated model. . . . .	66
4.16	Measured antenna input impedance magnitude (dashed) and phase (solid) versus ELD tuning capacitance at 245 MHz for an AMC tuning voltage of 12.5 V. . . . .	68
4.17	Measured radiation properties for the metamaterial antenna tuned to operate at 230 MHz. Left-hand circular polarized (solid) and right-hand circular polarized (dashed) realized gain versus frequency (top) and versus zenith angle $\theta$ (middle) for representative azimuth angles $\phi$ . Axial ratio versus zenith angle $\theta$ (bottom). . . . .	69

4.18	Measured radiation properties for the metamaterial antenna tuned to operate at 248 MHz. Left-hand circular polarized (solid) and right-hand circular polarized (dashed) realized gain versus frequency (top) and versus zenith angle $\theta$ (middle) for representative azimuth angles $\phi$ . Axial ratio versus zenith angle $\theta$ (bottom).	70
4.19	Measured radiation properties for the metamaterial antenna tuned to operate at 268 MHz. Left-hand circular polarized (solid) and right-hand circular polarized (dashed) realized gain versus frequency (top) and versus zenith angle $\theta$ (middle) for representative azimuth angles $\phi$ . Axial ratio versus zenith angle $\theta$ (bottom).	71
4.20	Measured boresight radiation properties for the metamaterial antenna tuned for various frequencies across the band. Left-hand circular polarized (solid) and right-hand circular polarized (dashed) realized gain versus frequency (top). Axial ratio versus frequency (middle). Tuning voltages for the AMC and ELDs to yield left-hand circular polarization at the marked frequencies (bottom).	73
5.1	Photograph of the metamaterial antenna and a conventional alternative, as well as the received power across the UHF satcom receive band.	77
5.2	Received power comparison between the metamaterial antenna and conventional alternatives. The metamaterial antenna's performance is comparable to the alternatives, but requires a mere third or less of their thicknesses.	78
5.3	Circuit board schematic for the bias voltage controlling circuit.	79
5.4	Printed circuit board layout for the bias voltage controlling circuit.	80
5.5	Photographs of the antenna controller box and constituent circuitry.	81
5.6	Photographs of a CCA (top), the metamaterial antenna mounted on the CCA (middle) and a comparison of the received power levels between the metamaterial antenna and a conventional antenna (bottom).	90

# Acknowledgments

The metamaterial-based horn antenna work was largely a collaboration with Dr. Qi Wu. Funding for the low-profile miniaturized antenna prototype manufacturing was provided through the Applied Research Laboratory at the Pennsylvania State University. Erik Lenzing at the Applied Research Lab gave direction to the project, specifically towards UHF satcom applications, as well as enabling and supervising the measurement comparisons to conventional alternatives. Jeffrey Miller at the Applied Research Lab's antenna measurement facility proved to be an invaluable help in debugging early prototypes, besides his assistance with antenna measurements.

*The buzz was all “metamaterial”  
But it seemed to remain quite ethereal;  
Until at Penn State  
The work had some weight  
And Ping ruled with air magisterial.*



# A Brief History of Radio-Frequency Electromagnetic Metamaterials

## 1.1 Metamaterials

For ages, mankind has relied on the variety of materials found naturally throughout the world to build homes and create tools to support and protect himself. In our age of rapid technological advances, the imaginations of scientists and engineers have ventured on to devices that would benefit from material properties that are not naturally available. Natural materials derive their electromagnetic properties from atomic and molecular structures that are much smaller than any radio-frequency wavelength. Several scientists and engineers of the past century realized that they could create material structures that were still much smaller than the wavelengths of interest that would mimic naturally occurring electromagnetic properties and even give rise to properties not typically found in nature. These novel properties are made possible by strategically placed resonances resulting from the specific shapes and dimensions of the subwavelength structures.

The term “metamaterial,” in the electromagnetic sense, refers to any material that derives its properties from manmade subwavelength inclusions, instead of from natural atomic, molecular, or crystal structures. Most of the work to engineer ma-



terial properties by subwavelength structures has been performed in the last decade or so, but several researchers from the 20<sup>th</sup> century controlled material properties by appropriately designing subwavelength and wavelength-scale structures.

## 1.2 Precursors to Metamaterials and Related Work

Kock introduced some of the earliest work to create artificial dielectric properties in the 1940s [1], [2]. Kock used conducting metallic structures to manipulate the phase velocity and thus create lenses for antenna systems. Corrugated metallic surfaces appeared for use in reflector antenna feeds in the 1960s [3]–[5]. Appropriately designed corrugations function as an electromagnetic soft-surface, forcing a perpendicular electric field to zero and supporting hybrid modes within the horn. This phenomenon leads to a polarization-independent radiation pattern with low side-lobes and a minimum of cross-polarized radiation, ideal for dual-polarization antenna systems, except for the large mass and high manufacturing cost.

Also in the 1960s, Veselago examined wave propagation in a hypothetical material with both the permittivity and permeability simultaneously negative [6]. This was the first thorough treatment of so called “left-handed materials” with the phenomena of backward wave propagation and negative refraction. More recent work (and more contemporary to metamaterials) that employs resonant structures with sizes on the order of either wavelength or subwavelength scales has fallen under the names of electromagnetic band gap structures [7] and frequency selective surfaces [8].

## 1.3 Early Work with Metamaterials

The renaissance of artificial dielectric and magnetic materials began with Pendry’s work on the perfect lens [9]. The general perfect lens requires a slab of material with electric permittivity and magnetic permeability both equal to negative unity. The resulting negative refraction restores the phase of the fields in the image plane, similar to traditional lenses. Unlike traditional lenses, the negative index lens also enhances the evanescent fields, restoring them to their levels at the source. With both the phase and evanescent field levels identical to the source plane, the perfect

lens avoids the problems of the diffraction limit, which applies to traditional lenses. Since the arrival of the theory of the perfect lens, many other applications of metamaterials have been proposed, ranging from lenses to invisibility cloaks [10], [11]. In contrast with the exotic new applications of the first metamaterials, as the field began to grow, researchers realized that metamaterials could be used to enhance existing devices, particularly antennas and optical devices. Here we will focus on antennas, as the challenges and capabilities of radio-frequency and microwave metamaterials are generally significantly different than optical metamaterials.

## 1.4 Where We Are Now

Electromagnetic metamaterials have been studied thoroughly for the past decade, and they are now on the verge of becoming a component in many commercial devices. The work presented here takes advantage of the advancements of the past decade to apply metamaterials to specific antennas. The first metamaterial we consider, a surface for lining horn antennas, builds on our earlier work reported in [12], which represented a leap forward in terms of both bandwidth and loss — the two factors that have limited nearly all metamaterial designs previously considered. The other major metamaterial here considered is an artificial magnetic conductor to reduce the profile of a miniaturized circularly-polarized crossed dipole for satellite communications in the VHF and low UHF bands. Current satcom antennas operating at these frequencies are large and unwieldy, but the new design reported here requires a small fraction of the thickness as well as reduced lateral dimensions. These size reductions are made possible by extending the radio's tuning circuitry to the antenna, which exhibits a small instantaneous channel bandwidth, but a large range over which the antenna system can be tuned.

## 1.5 Original Contributions

The following original contributions have resulted from this research.

### **1.5.1 Metamaterial Coatings for Hybrid-Mode Horn Antennas**

- Metamaterial surface designs enabling conical metahorns.
- Mode analyses for electromagnetic waves in metamaterial-lined circular waveguides.
- Tapering analyses for inhomogeneous metasurface-lined horns with low cross-polarization performance over an octave bandwidth.

### **1.5.2 Miniaturized Tunable Low-Profile Antenna with an AMC Substrate**

- Tunable AMC surfaces with a miniaturized unit cell and a tunable range of one to two octaves, depending on the AMC thickness, as well as an inherently lightweight structure resulting from using air as the principal dielectric material.
- End-loaded crossed-dipole antennas with dynamic near-arbitrary polarization operating over a tunable range of more than 20%.
- A miniature low-profile antenna combining the antennas and AMC surface, providing an arbitrarily-polarized beam with a tunable range of at least 35%.

# Inhomogeneous Metamaterial Coatings for Lightweight, Broadband Hybrid-Mode Horn Antennas

## 2.1 Metamaterial Surfaces

The introduction of metamaterial surfaces, or “metasurfaces,” by Sievenpiper [13] and Yang [14] initiated a storm of research into their various incarnations, including “high-impedance surfaces,” “artificial magnetic conductors (AMCs),” and “electromagnetic band-gap (EBG) structures.” One useful perspective when considering metasurfaces is that they comprise a two-dimensional version of a volumetric metamaterial [15], [16]. The reflection phase and dispersion properties of metasurfaces can be tailored for special characteristics under illumination by either surface or guided waves [7], [17]. Incident electromagnetic fields are controlled by varying the surface properties, which in turn are controlled by changing the dimensions of the constituent periodic unit cells, whether it be the physical dimensions or merely the electrical dimensions by adding lumped capacitors or inductors [18], [19].

Numerous applications of metasurfaces in antennas and microwave devices have been explored, such as AMCs for low-profile antennas [13], [20], partially reflective

surfaces as superstrates for directive antennas [21]–[23], high-impedance surfaces for quasi-TEM waveguides [24], and EBG structures to reduce coupling between nearby antenna elements [25]. Additional metasurfaces have included multiband AMCs [26], ultra-thin absorbers [27]–[29], metaferrires [30], matched impedance magneto-dielectric surfaces [31], and filters [32]. As will be explained shortly, metasurfaces have also recently been applied to feeds for satellite reflector antennas as an alternative and improvement upon corrugated horns.

## 2.2 Introduction to Hybrid-Mode Horn Antennas

Horn antennas have progressed through several stages in the past few decades as engineers have attempted to control side-lobe levels and cross-polarization, particularly for satellite reflector feeds. In the 1960s, Potter introduced his dual-mode horn [33], followed shortly thereafter by corrugated horns [3], [4], [5], and the dieguide feed [34]. In the 1980s, the dielectric core horn appeared, first proposed by Clarricoats *et. al.* with a foam core [35], and then by Lier *et. al.* with a solid dielectric core [36]. The dielectric core horn has a dielectric cone filling the horn with a small air gap separating it from the conducting walls. After the dielectric core horns came the strip-loaded horn, with conducting strips placed on a thin dielectric lining the horn walls [37], and the slotted dielectric lined horn, which has a corrugated dielectric lining the horn walls [38]. Other variations on the dielectric core horn include the dual-dielectric horn [39].

Corrugated horns and dielectric core horns are both heavy, which is very undesirable for satellite applications. Manufacturing corrugated horns requires much more machining than do simple horns composed of conducting walls. A much simpler alternative to the corrugated horn as a reflector feed is the rectangular trifurcated horn [40], [41]. The trifurcated horn does sacrifice some side-lobe suppression for structural simplicity however; beyond the first side-lobe, its pattern is rather similar to that of a plain horn.

Electromagnetic metamaterials offer a useful new perspective in designing horn antennas for low cross-polarization and other desired characteristics. Certain classes of metamaterials can be designed to function with the same desirable surface characteristics as corrugations, but over a wider bandwidth. Moreover,

metamaterials promise to be less expensive and much lighter than corrugations, making metamaterial horn antennas ideal candidates for satellite applications. Lier and Shaw investigated lining a conical horn with an ideal metamaterial [42], demonstrating low cross-polarization and the desired radiation characteristics over wide bandwidths.

For corrugated horns with low side-lobes, the corrugations function as a soft-surface [43], [44], creating a soft horn [45]. Earlier work considered a rectangular horn with a metamaterial soft-surface liner as an improvement upon the trifurcated horn, where the metamaterial soft-surface creates a smoothly tapered field distribution in the aperture, resulting in very low side-lobes and a much more symmetrical pattern than an unlined horn or even a trifurcated horn [12], [46]–[48].

## 2.3 Soft and Hard Surfaces and Horns

Corrugations and their relations are characterized by their anisotropic surface impedances, which we define in accordance with [43]. We consider an electromagnetic wave propagating parallel to a surface (grazing incidence). If we let  $\hat{z}$  be the direction of propagation along the surface and  $\hat{x}$  be transverse to this but still parallel to the surface, we can define the anisotropic surface impedances as follows:

$$Z^{TM} = R^{TM} + jX^{TM} = -\frac{E_z}{H_x} \quad (2.1)$$

$$Z^{TE} = R^{TE} + jX^{TE} = \frac{E_x}{H_z} \quad (2.2)$$

If the walls of a conical horn antenna satisfy  $X^{TM}X^{TE} = -\eta_0^2$  (where  $\eta_0$  is the impedance of free space), the horn supports *balanced hybrid modes*, which provide axially symmetric radiation patterns with no cross-polarization [4]. A more generalized condition that leads to no cross-polarization and modes that are independent of rotation angle in cylindrical waveguides or horn antennas is [49]

$$\frac{X^{TE}}{\eta_0} + \frac{\eta_0}{X^{TM}} = 0. \quad (2.3)$$

A surface is electromagnetically *soft* if the power flow along the surface (*i.e.*



the Poynting vector) in a given direction is zero [43]. Similarly, a surface is *hard* if the power flow along the surface is a maximum. A soft surface satisfies:

$$|X^{TM}| = \infty \quad \text{and} \quad X^{TE} = 0 \quad (2.4)$$

while a hard surface satisfies:

$$X^{TM} = 0 \quad \text{and} \quad |X^{TE}| = \infty \quad (2.5)$$

Ideal soft and hard surfaces are impossible in practice, but they can be approximated by  $|X^{TM}| \gg |X^{TE}|$  (soft) and  $|X^{TM}| \ll |X^{TE}|$  (hard), provided that  $X^{TM}X^{TE} = -\eta_0^2$  still holds [45].

Horn antennas lined with soft surfaces, or more simply “soft horns,” are characterized by an aperture field distribution that tapers from a maximum in the center to zero at the horn walls, resulting in low side-lobes. Hard horns have a uniform aperture field distribution, which leads to a higher aperture efficiency and thus peak gain, but also higher side-lobes. Both soft and hard horns provide low cross-polarization, assuming that their surfaces satisfy the hybrid-mode condition.

## 2.4 Design of Inhomogeneous Metasurfaces

While previous metamaterial horn antennas have employed liners with identical unit cell dimensions throughout the horn, we have explored varying the unit cell geometry along the length of the horn to minimize cross-polarized radiation, as well as using aperiodic metasurfaces to eliminate gaps in the lining. By properly tapering the surface impedance, we have created a hybrid-mode metahorn design with improved radiation characteristics and impedance matching over a broader bandwidth than previous metahorns based on homogeneous metamaterial liners. Tapered geometries are not new to microwave engineering, particularly for impedance matching [50]. The same technique has been applied in the development of corrugated horns, where corrugated waveguide mode converters gradually taper the depth of corrugations [49], [51]. Inhomogeneous metasurfaces based on the transformation optics design technique have also been proposed for Luneburg lenses and leaky-wave antennas [52]. In contrast with previous works on inhomogeneous

metasurfaces, which guided waves in the spatial domain, we engineer the dispersion of the metasurface, combined with spatial tapering, to yield broadband performance, improving the frequency-domain performance of metamaterial horn antennas.

Microwave metasurfaces have been composed of a variety of structures, including metallic screens on top of thin dielectric substrates (similar to frequency selective surface screens) [8] and wire-grid meshes [12]. Fig. 2.1(a) shows the general geometry of the metasurface that we have employed as a liner for horn antennas. The unit cell consists of a rectangular patch and a continuous strip along the x-direction with vertical wires connecting the patches to the conducting ground plane beneath. The analyses shown here apply to a free-standing structure, but the techniques are valid for printed-circuit-board construction as well.

Because the metasurface periodicity is much smaller than a wavelength, we can characterize the surface by its effective surface impedances, as defined in Equations 2.1-2.5, and elaborated on in [46]. The surface impedances can be calculated using a simple plane wave model, providing a straightforward design approach for metasurfaces with specific electromagnetic properties. Soft and hard surfaces used for soft and hard horn antennas have been characterized by grazing incident plane waves as an approximation to their behavior near the aperture of a horn [53]. Similarly, we simulated the metasurface using Ansys®HFSS™ under plane wave incidence at an angle of  $80^\circ$  from broadside, as indicated in Fig. 2.1(a).

To achieve the desired surface impedances, we placed conductors along the three coordinate axes as follows: the long continuous wires in the x-direction form a wire array, which has an inherent Drude permittivity response for TE waves with the electric fields polarized along the axes of the wires [54], [55]. These wires force  $E_x$  to be zero at the surface, controlling  $Z^{TE}$  in the band of interest. Similarly, the vertical posts couple with TM-polarized incident waves, leading to the desired value of  $Z^{TM}$ . The z-periodicity of  $p = 3\text{ mm}$  and thickness of  $t = 5.2\text{ mm}$  were chosen for operation between 10 and 20 GHz to include the  $K_u$ -band for satellite communications. The width of the continuous wire was chosen to be  $s = 0.4\text{ mm}$ . Forcing these parameters to remain constant provided regular layouts, allowing for intuitive placement of the metasurface within the horn antenna.

The tapering functions were applied primarily to two parameters: the patch



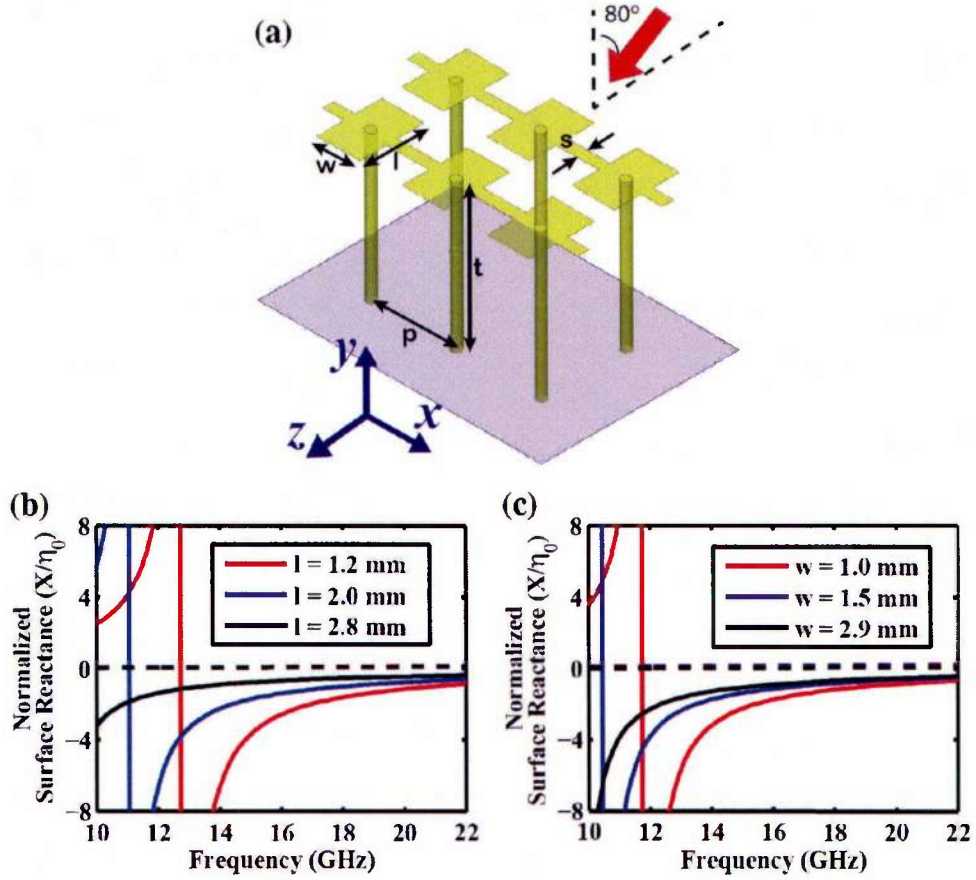


Fig. 2.1: (a) The geometry of a soft metasurface composed of metallic patches and wires (yellow). The effective properties of the metasurfaces were characterized with a plane wave at near grazing incidence ( $80^\circ$  from broadside) in the  $y$ - $z$  plane. (b) Normalized surface reactance of metasurfaces with patches of width  $w = 2.0$  mm and varying length  $l$ . (c) Normalized surface reactance of metasurfaces with patches of length  $l = 2.3$  mm and varying width  $w$ . The other dimensions of the metasurfaces are  $t = 5.2$  mm,  $s = 0.4$  mm, and  $p = 3$  mm.

width  $w$  and length  $l$ . The patches function as end loads for the vertical wires; thus, the varying the patch size provides direct control over the surface impedance. Moreover, with the patch end-loads, the thickness of the liner can be significantly reduced compared to the  $\lambda/4 - \lambda/2$  that is required for corrugated horns.

Full-wave numerical simulations were used to compute the normalized surface reactances of lossless metamaterial surfaces under TE and TM polarized illumination. Fig. 2.1(b) shows the dispersive surface reactance of metasurface structures with patches of width  $w = 2.0$  mm and varying length  $l$ . As  $l$  increases, the resonance in  $X^{TM}$  shifts to lower frequencies. Note that  $X^{TE}$  remains nearly zero while  $X^{TM}$  exhibits a negative value with decreasing magnitude at frequencies above its resonances. The reactances do not comprise an ideal soft-surface across the band, but they approximate it well enough to maintain good radiation performance when placed in a horn antenna. Similarly, when the patch length is fixed at  $l = 2.3$  mm and the width  $w$  is varied, an increase in  $w$  leads to a lower frequency resonance in  $X^{TM}$ .

## 2.5 Metasurfaces Coating a Cylindrical Waveguide

In addition to the plane wave model shown above, we have also studied the performance of the metasurface in a cylindrical waveguide. Fig. 2.2 shows the waveguide, which has an outer diameter of  $D_1 = 30.4$  mm. The metasurface periodicity is maintained at  $p = 3$  mm. The continuous wire then becomes a closed ring with a diameter of  $D_2 = 20.0$  mm. The patches were conformed to the shape of a cylinder of diameter  $D_2$ , and the vertical wires were oriented along the radial direction, connecting the patches to the waveguide walls.

Using the eigenmode solver in HFSS<sup>TM</sup>, the guided modes of the metasurface-coated waveguide were calculated in order to study the propagation properties of the hybrid-modes and how they varied with different metasurface designs. Moreover, the waveguide mode calculations provided verification of several of the assumptions used in the plane wave model for designing the metasurface. The waveguide field patterns are useful for estimating the radiation pattern of a lined horn or waveguide, which can be accomplished by assuming a uniform phase distribution over relatively large apertures.

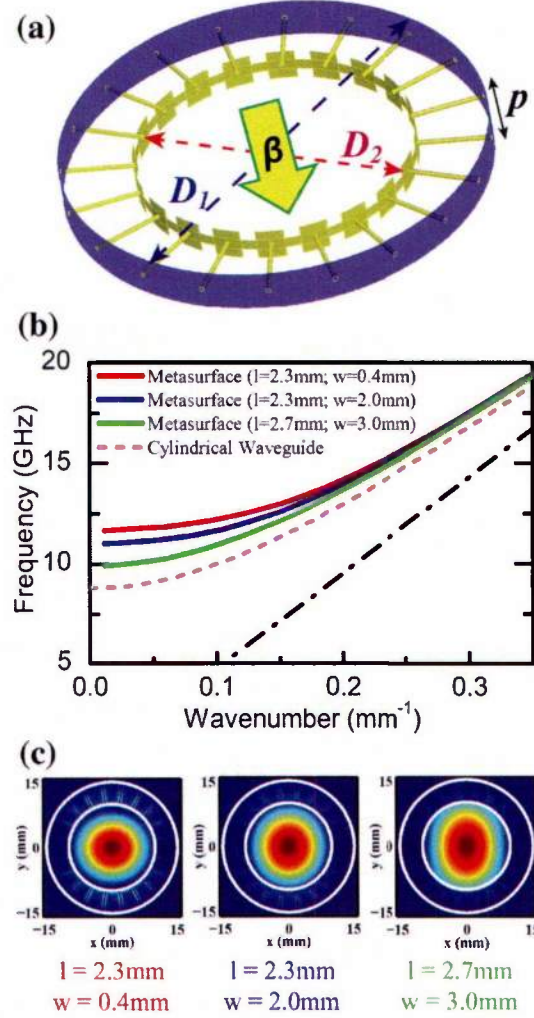


Fig. 2.2: (a) The schematic of one section of metasurface inside the straight waveguide of a metahorn. The periodicity of the metasurface structure along the wave propagation direction ( $\hat{\beta}$ ) is  $p = 3 \text{ mm}$ . The outer and inner boundaries of the metasurface liner have diameters of  $D_1 = 30.4 \text{ mm}$  and  $D_2 = 20.0 \text{ mm}$ , respectively. (b) The dispersion diagrams of circular waveguides containing metasurfaces with different dimensions. The dispersion of a circular waveguide with a diameter of  $20 \text{ mm}$  (dashed, pink) is shown as a reference. The light line is indicated by the dash-dotted black line. (c) The electric-field mode patterns of the three circular waveguides coated with metasurfaces at  $12 \text{ GHz}$ .

Fig. 2.2(b) shows the calculated dispersion diagrams for three different metasurface geometries. The solid curves show the modes for three different metasurface-lined waveguides, while the dashed line is for a simple cylindrical waveguide. Besides guiding hybrid modes, waveguides lined with impedance surfaces can also support surface-wave modes at some frequencies [56]. As we were only interested in hybrid modes, the dispersion diagrams shown represent the  $HE_{11}$  modes for the various waveguides. The dispersion diagram for the plain cylindrical waveguide is for a diameter of 20 mm and the  $TE_{11}$  mode, which has a cutoff frequency of 8.8 GHz. Note that the metasurfaces increase the cutoff frequency as a result of the soft-surface boundary. The cutoff frequencies for the  $HE_{11}$  modes of the three metasurface-lined waveguides are 11.7 GHz, 11.0 GHz, and 9.9 GHz. Metasurfaces with larger patches led to hybrid modes with lower cutoff frequencies. This is consistent with the plane wave model from Fig. 2.1(b-c), where the larger patches lowered the soft-surface performance in frequency. At frequencies significantly above cutoff, all the guided  $HE_{11}$  modes converge to the  $TE_{11}$  mode of the cylindrical waveguide.

Fig. 2.2(c) shows the electric-field mode patterns the of the three metasurface-coated waveguides at 12 GHz. The coatings effectively taper the field magnitudes to be zero at the surface. Consistent with balanced hybrid modes, the aperture electric fields consisted nearly entirely of a linearly polarized  $E_y$  component, with  $E_x$  being nearly zero. Note that smaller patches led to a smaller mode pattern at 12 GHz, which is close to the waveguide cutoff frequency. This results from the larger surface reactance of the smaller patches at this frequency. Lastly, the metasurfaces with smaller patches showed larger induced currents on their vertical/radial wires, as they were operating close to their resonance.

## 2.6 Metamaterial Horns with Homogeneous Metasurface Liners

Previous work has demonstrated that horns with metamaterial liners can exhibit low  $E$ -plane sidelobes and low cross-polarization over more than an octave bandwidth [12], [46]. We first created a conical horn antenna with a homogeneous

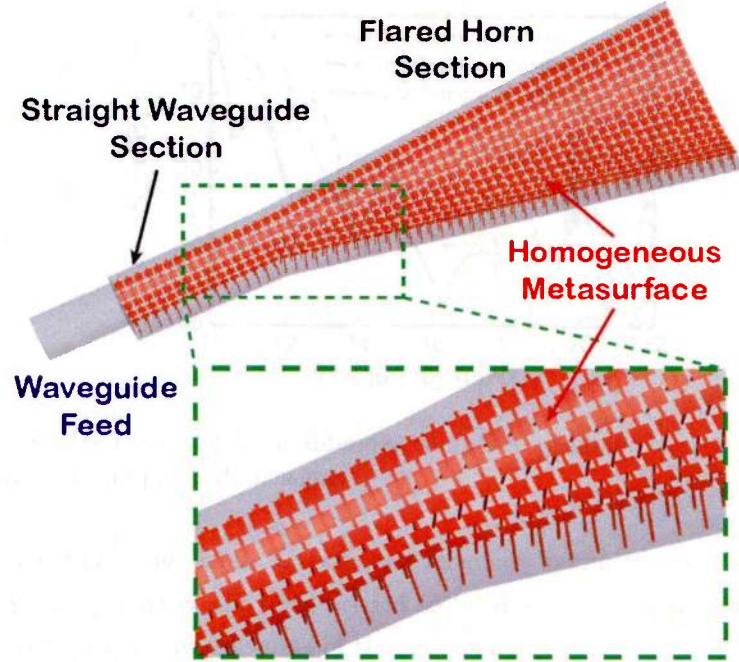


Fig. 2.3: The interior view of a metahorn antenna with homogeneous metasurface liners covering both the flared horn section and the straight waveguide section. The metahorn is fed by a circular waveguide with a diameter of 20 mm.

metasurface liner as described above. Fig. 2.3 shows the interior of the metamaterial horn with the metasurface lining both a section of waveguide and the horn itself. The horn aperture had a diameter of 70 mm, or  $2.3\lambda$  at the low end of the frequency band. The flared portion of the horn was 115 mm long, including 40 rows of the metasurface's unit cells on the horn walls. The lined waveguide included 15 rows of unit cells for a total length of 45 mm, effectively suppressing higher-order modes. This waveguide section was fed by another section of plain cylindrical waveguide with a length of 25 mm and a diameter of 20 mm, aligning the waveguide wall with the inner surface of the metamaterial in the lined waveguide. A cylindrical wave port excited the  $TE_{11}$  mode in the cylindrical waveguide section.

HFSS<sup>TM</sup> was used to perform full-wave simulations of the completed structure, predicting axially symmetric radiation patterns with low sidelobes and low cross-



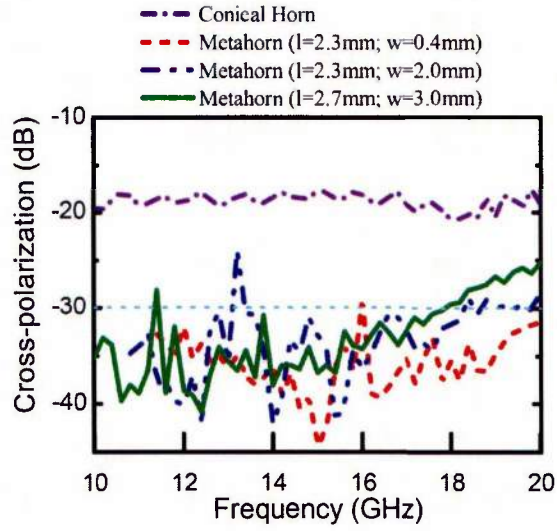


Fig. 2.5: Peak relative cross-polarized radiation with respect to the maximum co-polarized field in the radiation patterns of a conical horn antenna and three soft horns with various homogeneous metasurface liners. The maximum cross-polarization level was evaluated at a  $45^\circ$   $\phi$ -plane cut where the metahorn exhibits the highest cross-polarized radiation. The relative cross-polarization of a conventional conical horn with the same dimensions (dash-dotted, purple) is shown as a reference.

ness of the metasurface liners. Unfortunately, higher-order modes are excited above approximately 18 GHz, leading to increased cross-polarization, which rises over  $-30$  dB, especially for the horn with the largest metasurface patches.

These results show the effectiveness of uniform metasurface liners for controlling the radiation pattern of horn antennas. Engineering the dispersive properties of metasurfaces through varying patch dimensions achieved important design flexibility. Finally, we have found a trade-off in terms of patch size: larger patches reduce the cutoff frequency, but give rise to increased cross-polarization at higher frequencies.

## 2.7 Metamaterial Horns with Spatially Tapering Liners

The analyses presented above suggested a practical method for extending the bandwidth of metamaterial horn antennas. The return loss performance primarily depended on the patch sizes in the waveguide and at the horn throat, while the radiation performance at the higher frequencies depended on the patch sizes on the horn walls. The solution to extend the operating bandwidth was to use large patches in the waveguide, but taper the patch size in the horn itself to minimize reflections while suppressing higher-order modes. Fig. 2.6(a) shows a horn with large patches in the waveguide and horn throat tapering to smaller patches closer to the aperture. Multiple tapering functions were examined, including both linear and exponential functions of patch width and length. Both good impedance bandwidth and radiation performance were achieved using an exponential decay function, as shown in Fig. 2.6(b), where the patch width varies from 3.0 mm to 0.4 mm and the length varies from 2.7 mm to 2.3 mm. That is, the metasurface designs in the throat and aperture of this horn correspond to the solid (green) and dashed (red) curves in Figures 2.4 and 2.5. The dimensions of the metasurface in the waveguide were identical to those of the metasurface at the throat of the horn.

Fig. 2.7 shows the reflection coefficient ( $|S_{11}|$ ) for the metahorn with a tapered liner. The large patches in the waveguide and horn throat lead to a cutoff frequency just below 9.8 GHz, maximizing the impedance bandwidth at the low end of the

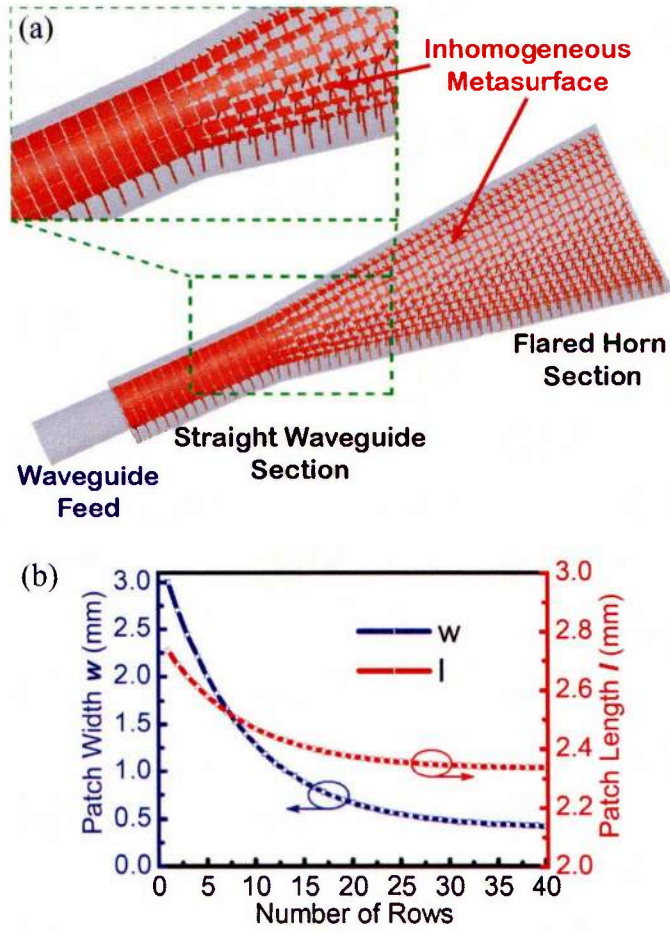


Fig. 2.6: (a) The interior view of a metahorn antenna with inhomogeneous metasurface liners covering both the flared horn section and the straight waveguide section. The metahorn is fed by a circular waveguide with a diameter of 20 mm. (b) The sizes of the metallic patches at each row of the metasurface in the flared horn section. Both the length and width of the patches follow an exponentially decaying function and decrease in size towards the aperture of the metahorn.



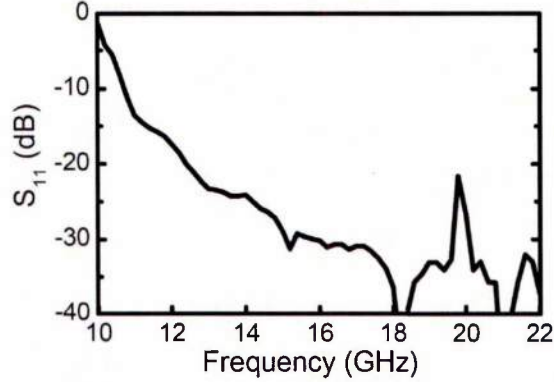


Fig. 2.7: Calculated  $S_{11}$  of the soft metahorn antenna with inhomogeneous metasurface liners.

band. This reflection performance is very similar to that of the horn with a uniform liner with the largest patches (solid green curve) in Fig. 2.4. Above the cutoff frequency, the horn operates on the tail of a resonance, resulting in a combination of low return loss and minimal absorption loss in the metamaterial liner. It is also expected that further optimization of the horn's throat will yield even better impedance performance.

Fig. 2.8 shows the cross-polarization performance of the metahorn with an inhomogeneous liner. Besides improving the return loss at the lower frequencies, the inhomogeneous metasurface supports the hybrid ( $HE_{11}$ ) mode over the higher frequencies, extending the performance at the upper end of the band. At this point, the relative cross-polarization remains below -30 dB from 10.2 GHz to 20 GHz, primarily a result of the smaller patches approaching the horn's aperture. For comparison, the cross-polarization performance of a conical corrugated horn is shown as well (dashed curve). The corrugation depth is a uniform value of 6 mm. The corrugated horn shows slightly better cross-polarization near its designed frequency of 12-14 GHz, but the metahorn exhibits low cross-polarization over a significantly wider bandwidth, demonstrating the broad band performance of the inhomogeneous metahorn. One may argue that the corrugated design could be further optimized [57], but the comparison is representative because the metahorn could be further optimized as well. The results indicate that the metahorn is a

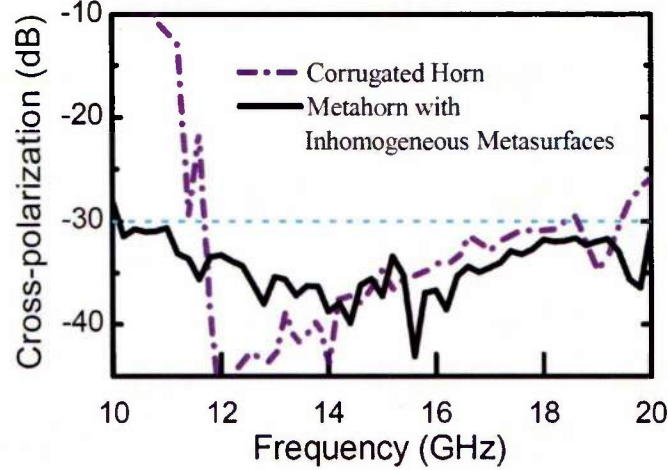


Fig. 2.8: Peak relative cross-polarized radiation with respect to the maximum co-polarized field in the radiation patterns of the soft metahorn with inhomogeneous metasurface liners. The maximum cross-polarization level was evaluated at a  $45^\circ$   $\phi$ -plane cut where the metahorn exhibits the highest cross-polarized radiation. The relative cross-polarization of a conical corrugated horn with the same dimensions (dash-dotted, purple) is shown as a reference.

significant challenger to the corrugated horn, particularly with its benefits of broad bandwidth and light weight.

Fig. 2.9 shows the radiation patterns of the inhomogeneous metahorn at several frequencies across its operating band. The  $E$ -plane and  $H$ -plane co-polarized radiation patterns are nearly identical within the main beam, indicating that the metahorn radiates rotationally symmetric patterns. Such patterns are necessary for optimal efficiency in many reflector antenna systems. The spatially-varying, dispersion-engineered metasurface produces axially-symmetric radiation patterns with low-cross polarization and broad bandwidth, desirable qualities for feeds for satellite reflector antennas.

As expected from a soft horn antenna, the inhomogeneous metahorn demonstrates its tapered aperture field distribution through reduced sidelobe levels (below  $-22$  dB) compared to a plain conical horn, as shown in Fig. 2.10. The metahorn shows sidelobe levels that are more than 10 dB below those of the conical horn at most frequencies. The corrugated horn does provide even lower sidelobes in its

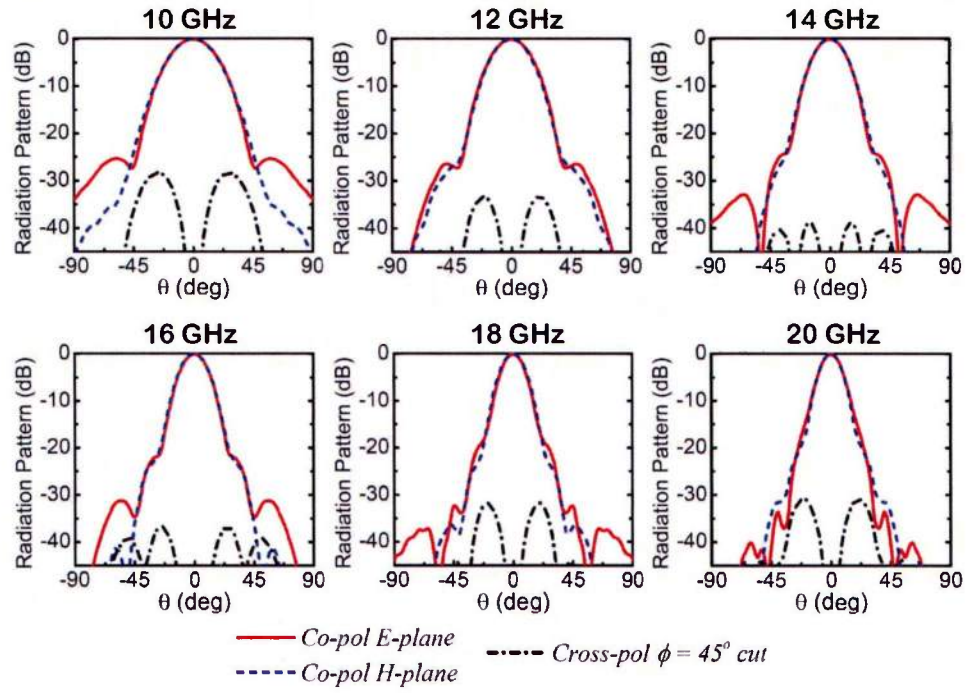


Fig. 2.9: Simulated E-plane, H-plane, and  $45^\circ$   $\phi$ -plane cut co- and cross-polarized radiation patterns of the soft metahorn with inhomogeneous metasurface liners at various frequencies across the band. Note that the copolarized patterns are approximately identical in both planes within the main beam, producing radiation patterns that are nearly independent of polarization.

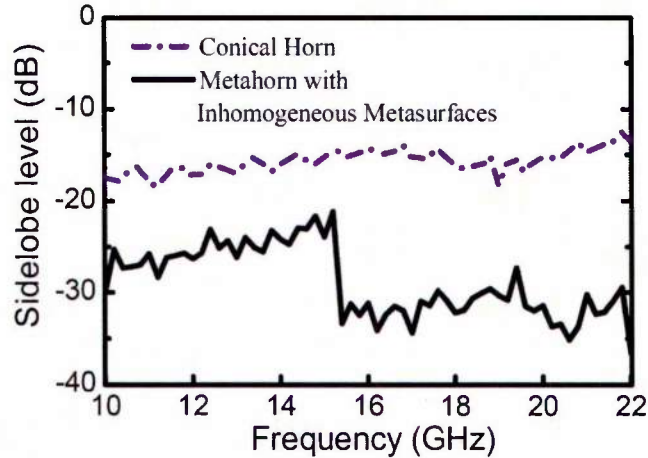


Fig. 2.10: Peak relative sidelobe level with respect to the maximum copolarized field in the radiation patterns of the soft metahorn with inhomogeneous metasurface liners. The  $E$ -plane relative sidelobe level of a conventional conical horn and a corrugated horn with the same dimensions (dashed, red and dash-dotted, purple) are shown for comparison.

designed frequency range, but the metahorn shows its low sidelobes over a broader bandwidth. These low sidelobe levels are desirable because lower sidelobes reduce spillover losses in reflector antenna systems.

Fig. 2.11 shows the aperture field distributions for the various horns at two frequencies in their operating bands. Note the field distributions that taper from zero (dark blue) at the metasurface walls to a maximum (dark red) in the center of the horn aperture. In contrast, the fields in the conical horn only taper from the sides, while showing a much more uniform pattern vertically. This pattern leads to high sidelobes, and the nonlinear field directions increase cross-polarized radiation. Finally, note that the fields of the metahorn are nearly identical to those of the conical horn, except that the metahorn operates over a broader bandwidth.

One last important parameter that we investigated was the horn flare angle, which controls the length of the horn for a given aperture size. The flare angle has been a challenging parameter in corrugated horns, forcing designers to create profiled horns to reduce antenna size [57]. We investigated three different horn designs with semi-flare angles of  $10^\circ$ ,  $12.3^\circ$  and  $15^\circ$ , keeping the horn aperture

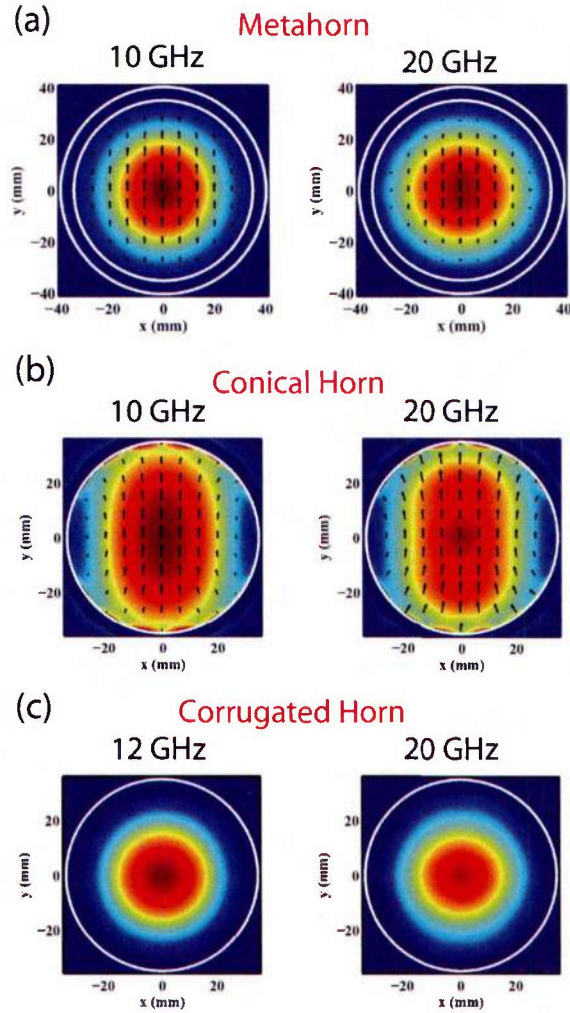


Fig. 2.11: (a) Calculated co-polarized electric field distributions at the aperture of the soft metahorn with inhomogeneous metasurface liners at 10 and 20 GHz. The fields are tapered towards zero at the wall of the metahorn because of the soft metasurface coatings. (b) Calculated co-polarized electric field distributions at the aperture of a conventional conical horn. (c) Calculated copolarized electric field distributions at the aperture of a corrugated horn.



diameter at 70 mm. The horn lengths became 142, 115, and 93 mm, respectively. We maintained the tapering profiles for the metasurface, however, but because of the exponential decay, the patch sizes at the horn aperture remained very nearly constant. As expected, because the metasurface at the horn throats are the same, the return loss and cutoff frequencies of the three horns are nearly identical, as shown in Fig. 2.12(a). The cross-polarization shows no clear trend however. Fig. 2.12(b) shows that the cross-polarization levels exhibit spikes as high as -26 dB, but that levels are generally low across the band. The cross-polarization is sensitive to the excitation of higher-order modes, suggesting that metahorns will require optimization of the entire horn, analogous to what is required for profiled corrugated horns.

## 2.8 Summary

We have developed metasurface designs consisting of metallic patches and connecting wires, which provide the surface impedances necessary to enhance the performance of conical horn antennas over a broad bandwidth. Engineering the metasurface dispersion by varying the dimensions of the patches in the unit cells yielded soft surfaces with controllable surface impedances across the desired operating band. Lining a cylindrical waveguide gave rise to balanced hybrid modes with linearly polarized fields and tapered magnitudes. Calculations of the guided modes supported by the waveguide gave rise to dispersion profiles, which depended strongly on the metasurface geometry, particularly at frequencies near cutoff.

Applying these metasurfaces to horn antennas made it possible for the metahorns to support hybrid modes over a broad bandwidth. Recognizing the trade-off between the return loss and cross-polarization bandwidths for horns with uniform liners enabled us to design inhomogeneous horn liners which extended the bandwidth to an octave of rotationally symmetric radiation patterns with low cross-polarization and low sidelobes. These characteristics, combined with the lightweight nature of metahorns, make them ideal candidates for spaceborne reflector antennas.

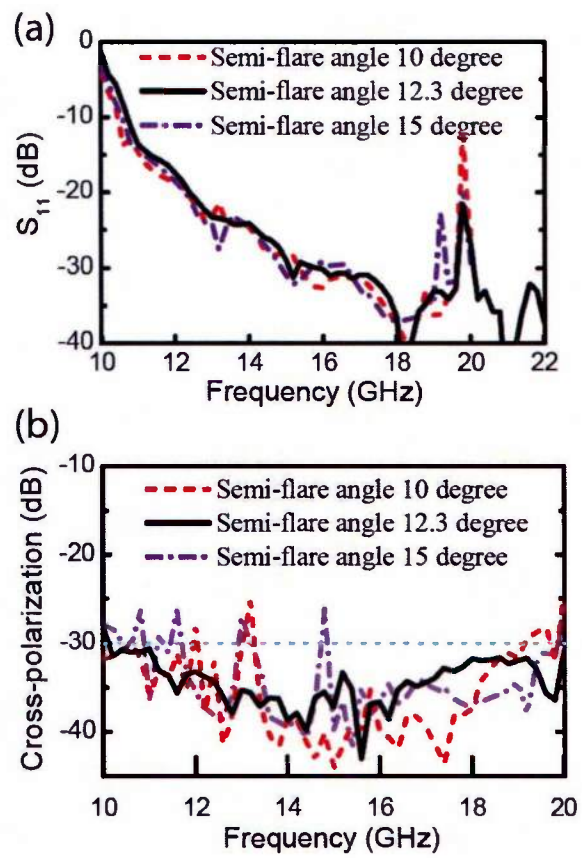


Fig. 2.12: Calculated (a)  $S_{11}$  and (b) peak relative cross-polarized radiation of soft metahorn antennas with semi-flare angles of  $10^\circ$ ,  $12.3^\circ$  and  $15^\circ$ , respectively.

# Near-Arbitrary Polarization from Tunable Crossed End-Loaded Dipoles

## 3.1 Introduction

Crossed dipoles have been employed to radiate circularly-polarized (CP) waves for nearly a century [58]. Two identical dipoles are mounted perpendicularly to each other, and they are fed through a matching and phasing network such that there is a  $90^\circ$  phase difference between the waves energizing each dipole, resulting in a CP beam. Bolster simplified this design by using two dipoles with differing dimensions leading to a  $90^\circ$  phase difference in their input impedances [59]. This approach obviated elaborate feeding networks, allowing the antenna to radiate a CP beam while using a simple feed. Many applications can benefit from miniaturized antennas, but reduced antenna size is accompanied by well-known bandwidth and gain limitations [60], [61]. Limited bandwidths can be used to advantage, however, in many radio communication applications, where individual channels require a limited instantaneous bandwidth. By making a narrow-band antenna tunable over the entire band of the radio, the antenna can still provide good performance while allowing for the flexibility of operating at any channel in the band. Various researchers have studied static end-loaded dipoles as miniaturized



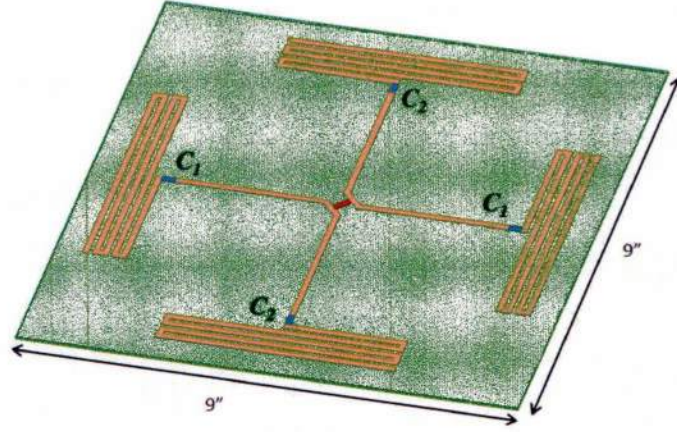


Fig. 3.1: Geometry of the preliminary crossed ELD design. The trace width is 0.100" and the substrate is 0.050" thick Rogers 5880LZ, which has a dielectric constant of 1.96.

antenna elements [62], [63], even using Bolster's approach to achieve CP radiation [64]. We add tunable capacitors to end-loaded dipoles (ELDs) to achieve both frequency agility and dynamically reconfigurable polarization characteristics. We have developed the concept of tunable crossed end-loaded dipoles in the context of low-profile antennas enabled by artificial magnetic conductors, as in [65] and later chapters, but in this chapter we focus on the dipoles and their polarization characteristics apart from any novel substrates.

### 3.2 Preliminary Work

Fig. 3.1 shows a preliminary design for crossed end-loaded dipoles, and Fig. 3.2 shows the input admittance of a single ELD as its tuning capacitors change, with each curve corresponding to a specific frequency. At 350 MHz, tuning capacitances of 1.58 pF and 2.10 pF result in input admittances with identical real parts of 11.0 millisiemens (mS), but a phase difference of 90°. Applying this to a crossed ELD, as shown in Fig. 3.1, we set  $C_1 = 1.58$  pF and  $C_2 = 2.10$  pF, which results in a circularly polarized beam.

Performing full simulations of three different capacitor configurations across the tunable band showed that the 9" crossed ELDs provide approximately 1 dB of real-

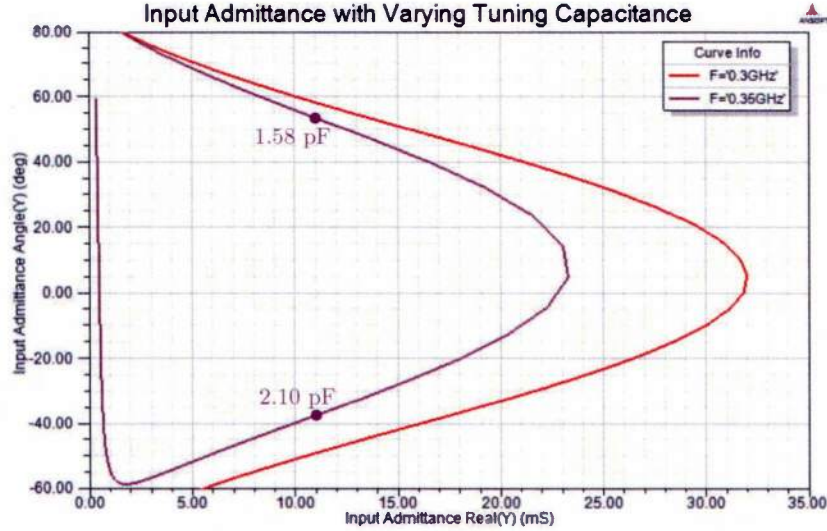


Fig. 3.2: Input admittance of an ELD with varying tuning capacitance. Note that at the two marked capacitances, there is a  $90^\circ$  phase difference but identical real parts.

ized circularly polarized gain across the tunable band, as displayed in Fig. 3.3. For the ELD geometry shown, its tunable range includes 270 MHz through 340 MHz. For a given capacitance configuration, the 3 dB bandwidth is between 1% and 2%.

Fig. 3.4 shows the input reflection coefficient magnitude  $|S_{11}|$  corresponding to the configurations shown in Fig. 3.3. At the respective operating frequencies, the magnitude of  $S_{11}$  stays below  $-15$  dB, corresponding to a VSWR that is better than 1.5:1.

Constructing a prototype required several modifications to the design. The idealized feed point had to be made more realistic by incorporating an RF transformer functioning as an unbalanced-to-balanced converter (balun). Moreover, the end-loads needed to have a DC bias applied to them in order to properly tune the varactor capacitance. Lastly, a DC bias needed to be applied at the feed point as well, which was accomplished using a conventional bias-tee. The RF transformer chosen was the Mini-Circuits TC1-1-13MG2+, which provided minimal insertion loss in the frequency range of interest here.

The printed circuit board (PCB) layout for the final design is shown in Fig. 3.5, including the connecting pads for the RF transformer at the center feed along with

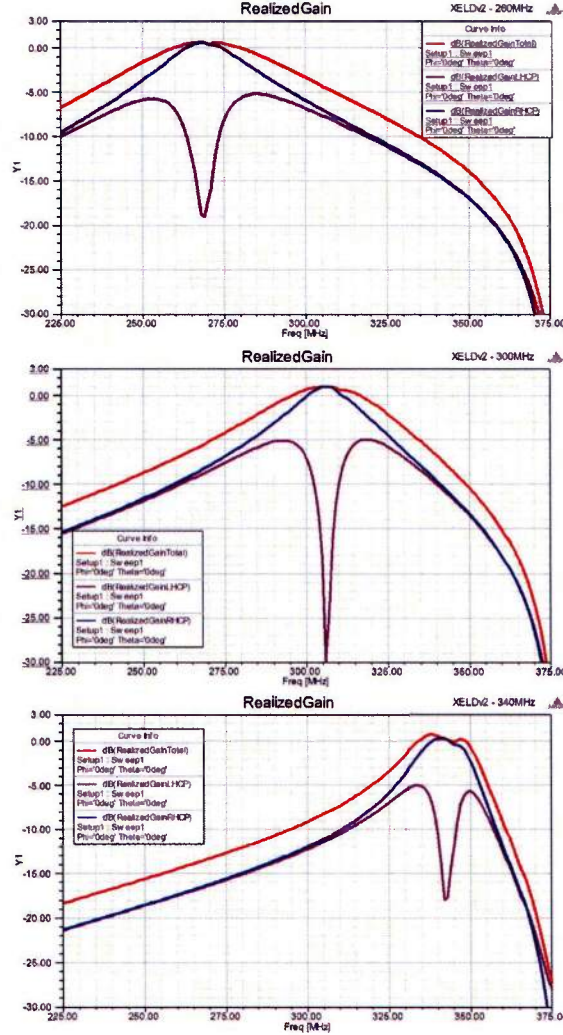


Fig. 3.3: Realized gain for three different tuning capacitor configurations. The red curve is the total gain, purple is the left-hand circularly-polarized (LHCP) gain, and blue is the desired right-hand circularly-polarized (RHCP) gain. The ELD achieves 1 dB of realized gain from a circularly-polarized beam with instantaneous bandwidths of approximately 1% over a total tunable bandwidth of more than 25%. (a)  $C_1 = 8.5 \text{ pF}$ ,  $C_2 = 20 \text{ pF}$  (b)  $C_1 = 2.64 \text{ pF}$ ,  $C_2 = 3.85 \text{ pF}$  (c)  $C_1 = 0.83 \text{ pF}$ ,  $C_2 = 1.13 \text{ pF}$

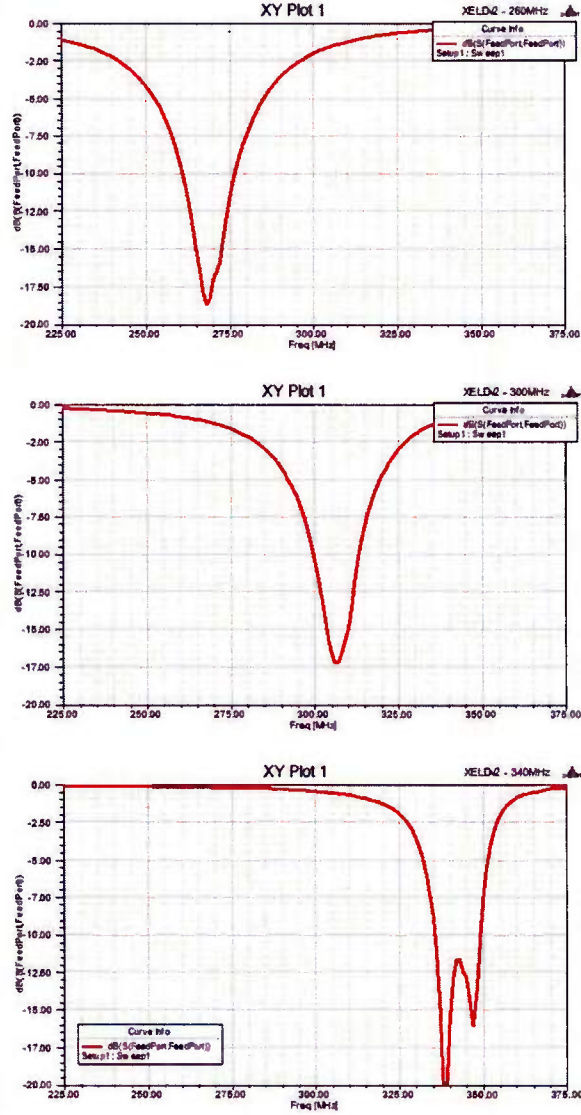


Fig. 3.4: Input reflection coefficient  $S_{11}$  for the three configurations shown in Fig. 3.3. Note that, at the respective operating frequencies,  $|S_{11}|$  is below  $-15$  dB across the entire tunable range.

those for the inductors functioning as RF chokes attached to the end-loads. Finally, Fig. 3.6 shows photographs of the preliminary antenna prototype, along with input measurements compared to simulations. This prototype showed that the crossed ELDs could indeed be tuned, but the trends failed to match the simulations. It was later discovered that the 100 nH choke inductor was insufficient for isolating the biasing lines from the ELDs, and this is likely a major cause of the discrepancies found here.

Fig. 3.7 shows a simulation that was used to improve the bias isolation circuit for later prototypes. The simulation was placed on a microstrip line in order that the effect of a series inductance and shunt-to-ground capacitance could be considered apart from other parts of the geometry. The initial prototype had a 100 nH inductor, which is shown to have very poor isolation performance, with a transmission coefficient ranging from -4 dB to -8 dB from 200 MHz to 300 MHz. The 100 nH value was chosen as an attempt to be conservative in terms of the inductor's self-resonant frequency. Increasing the inductance to 390 nH yields a drop in the transmission coefficient to less than -15 dB across most of the band, while still providing a self-resonant frequency that is still sufficiently greater than the operating band. Adding a shunt-to-ground capacitance improves the isolation even further, with the transmission coefficient dropping below -30 dB, besides giving a uniform response over frequency. The capacitor can be added if the bias voltages are applied to the ELDs through coaxial cables, and the capacitor can connect any RF energy that does get through the inductor with the outer sheath of the coaxial cable, which in turn is connected to the RF ground plane beneath the antenna.



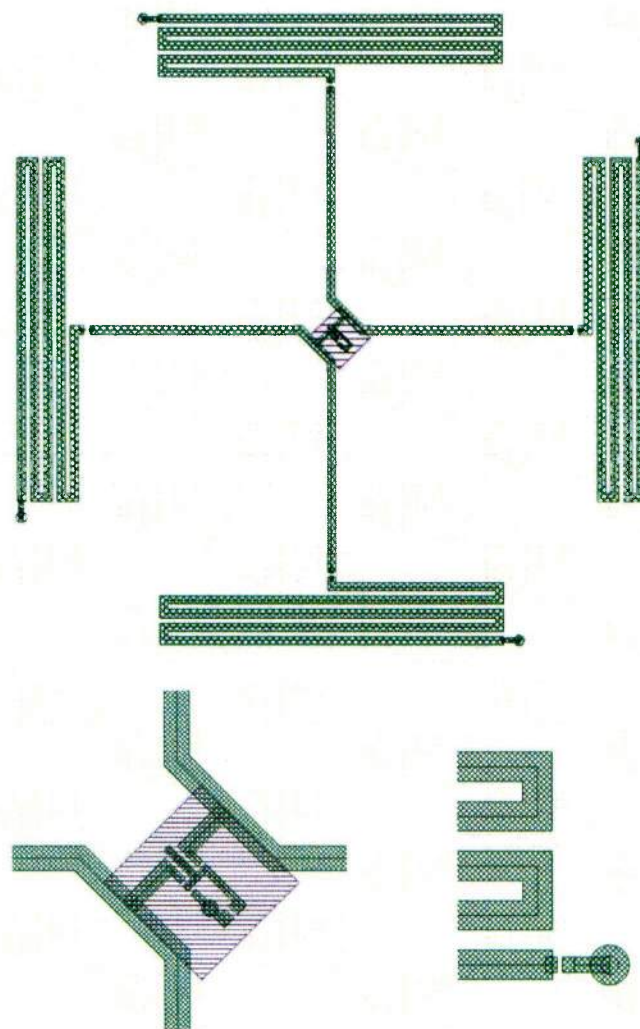


Fig. 3.5: Printed circuit board layout for the ELD prototype (a), including connection pads for the RF transformer at the feed point (b) and for the inductors as RF chokes (c) to connect a DC bias to the end-loads (for tuning the varactors).

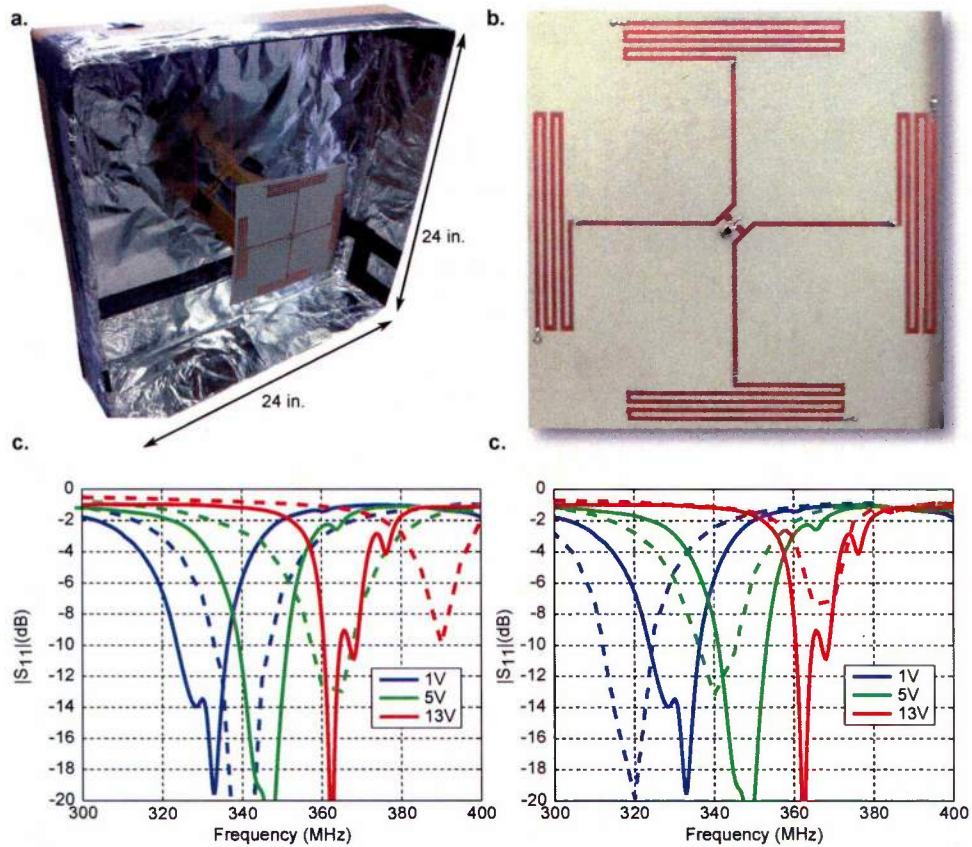


Fig. 3.6: (a) Photograph of the initial crossed-ELD prototype above a 24 in. square cavity. (b) Close-up view of the crossed ELDs. (c) Measured antenna input reflection coefficient (solid) compared to the simulated reflection coefficient for the antenna 6 in. above the cavity. (d) Measured antenna input reflection coefficient (solid) compared to the simulated reflection coefficient for the antenna 8 in. above the cavity.



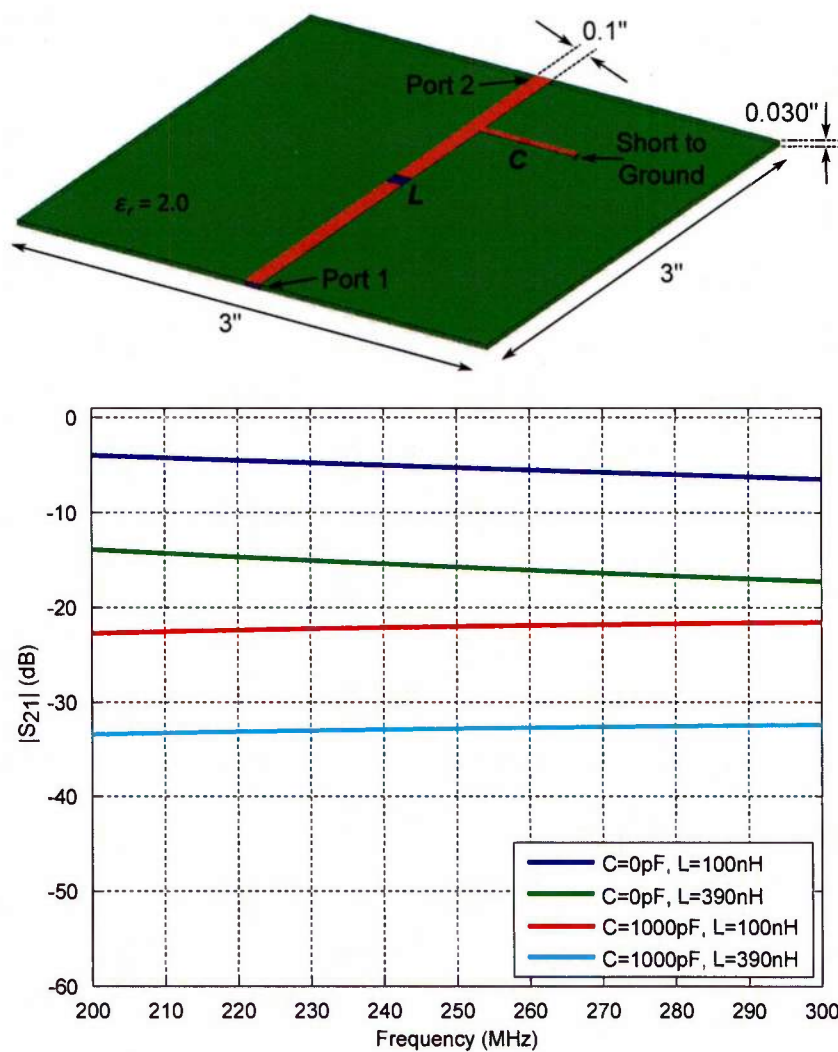


Fig. 3.7: Geometry (top) and simulated results (bottom) to reduce power flow to the DC biasing lines from the ELDs. Various combinations of series inductance  $L$  and shunt-to-ground capacitance  $C$  are shown.

### 3.3 Antenna Geometry

Fig. 3.8 shows final details and dimensions of the tunable crossed end-loaded dipole antenna geometry considered here. The dipoles consist of 1 oz. copper traces on a 0.020 in. thick and 35 cm square FR4 substrate, which is elevated 30 cm above a 90 cm square aluminum ground plane. The ground plane was included and the elevation distance was chosen to be one quarter wavelength at 250 MHz in order to provide a unidirectional beam for testing purposes while allowing the tuning circuits to be placed behind the ground plane, minimizing their interference with the antenna performance.

A single coaxial cable feeds the center of the dipoles, where a Mini-Circuits TC1-1-13MG2+ 1:1 RF transformer is used as a balun. The tunable capacitor on each leg of each dipole is an Infineon BB857 varactor diode, which can be tuned from several picofarads down to approximately 0.6 pF across a range from 0 V to 20 V. Placing the tuning capacitors adjacent to the meandered end-loads maximizes the tuning range of the antenna, as opposed to placing the capacitors closer to the feed point or within the end loads. The feed point is connected to a DC ground through a bias tee on the feed line, and the DC tuning voltages are applied to the varactor diodes through the end loads. The center pin of a coaxial cable provides the DC bias to each end-load, where a 390 nH series choke inductor and a 2,200 pF shunt-to-ground capacitor reduce the RF energy propagating out the bias lines by more than 30 dB. The capacitor is placed between the biasing line and the outer sheath of the coaxial cables just before connecting to the choke inductor. Sections of 0.5 in. CPVC pipe provide mechanical support for the prototype antenna.

### 3.4 Impedance Characteristics of End-Loaded Dipoles

In order to achieve circularly polarized radiation, Bolster varied the physical antenna dimensions to adjust the electrical length of each dipole, and thus create a 90° phase difference between the input impedances of two perpendicular dipoles. For this antenna, the tunable capacitors dynamically adjust the electrical length of each dipole, allowing the polarization to be reconfigured dynamically. Fig. 3.9 shows

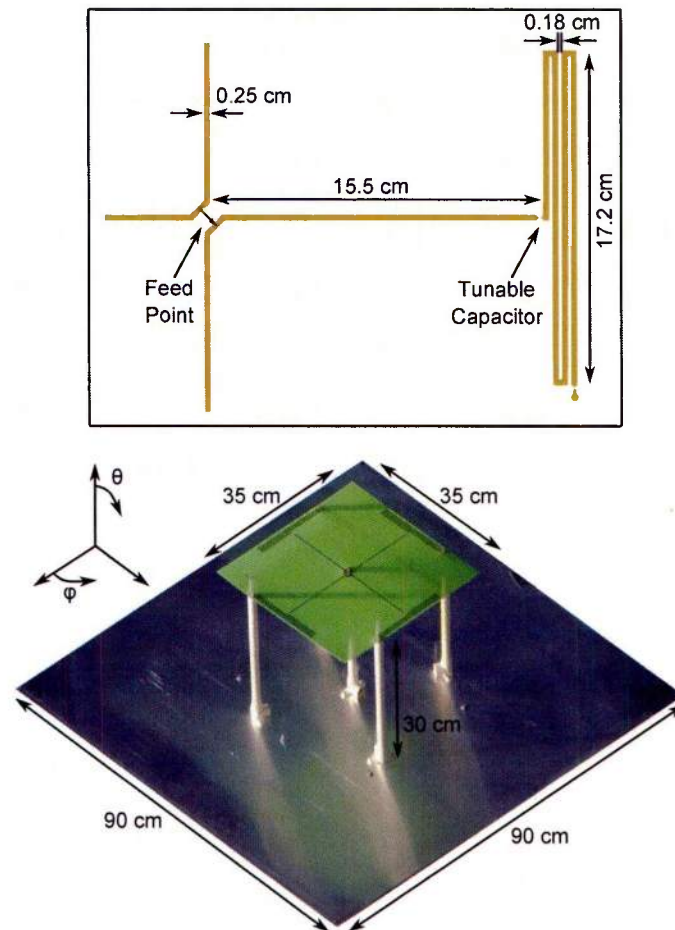


Fig. 3.8: End-loaded dipole geometry and photograph of the prototype. Top: Detailed dimensions of partial dipole with meandered end-load. Bottom: Photograph of the prototype and remaining dimensions. The dipoles consist of 1 oz. copper traces on a 0.020 in. thick FR4 substrate.

the simulated antenna input characteristics as a function of tuning capacitance for various frequencies, for the antenna with all four tuning capacitances set to the same value. Because the parallel combination of two identical impedances results in an impedance with half the magnitude and the same phase as the original impedance, we can use this plot to choose tuning capacitances that will yield a  $90^\circ$  phase difference between the input impedances of each of the two dipoles, as is necessary for circularly polarized radiation.

For example, in order to achieve circular polarization at 260 MHz, the simulation predicts that one dipole should be tuned with approximately 0.9 pF, while the second dipole should have approximately 1.4 pF. This combination provides the necessary  $90^\circ$  phase difference between the two input impedances, while ensuring that the two dipoles have approximately equal impedance magnitudes. The similar impedance magnitude values guarantee that each dipole radiates at the same power level; otherwise the antenna would radiate with an elliptical polarization rather than circular. Switching between the right- and left-handed sense of polarization is achieved by simply switching the tuning capacitances between the two dipoles. Linear polarization parallel to a single dipole can be achieved by tuning that dipole for best return loss at the desired frequency, while tuning the other dipole for poor return loss at that frequency. Linear polarization parallel to the feed point simply requires tuning both dipoles identically. Linear polarization perpendicular to the feed point can be approached by tuning the two dipoles such that the phase difference between them approaches  $180^\circ$ , though the antenna's return loss may be degraded such that it would yield better gain if it were configured for circular polarization and suffered the 3 dB loss from polarization mismatch. Elliptical polarization would also be possible with various orientations if the application would require it.

In order to verify that real varactor diodes would not have a significant effect on the antenna's performance compared to ideal capacitors, the  $S$ -parameters of a Skyworks SMV1265 varactor diode and of an Infineon BB857 varactor diode were measured on a two-port microstrip test board, as shown in Fig. 3.10 and Fig. 3.11. The measured curves show slight variations with frequency, unlike the ideal capacitor, but in all cases, the tuning voltages give very similar performance to that of an ideal capacitor. Finally, Fig. 3.12 shows the crossed ELDs input

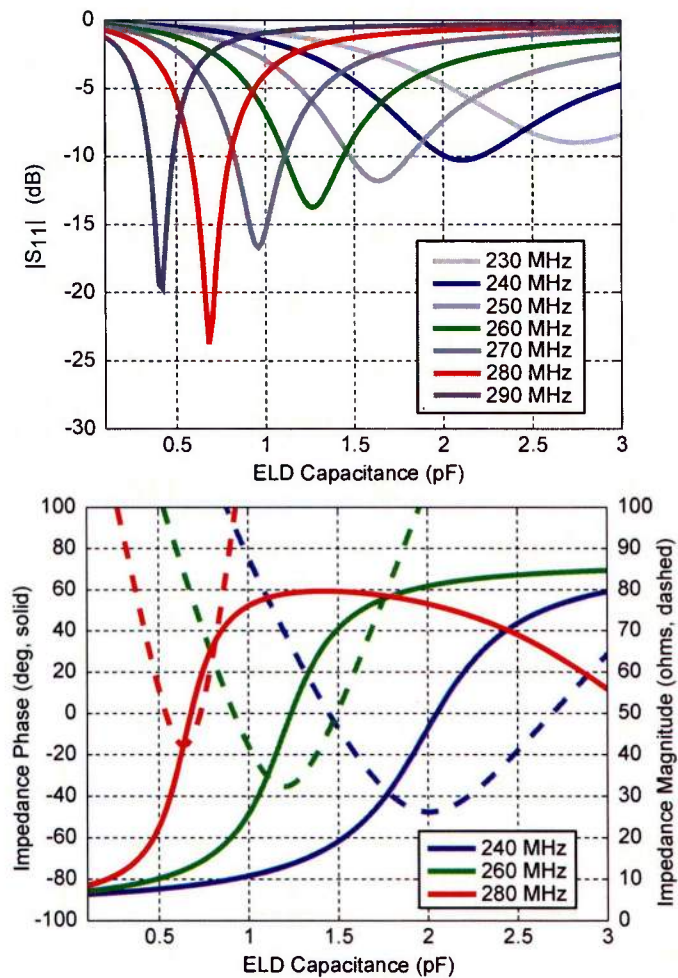


Fig. 3.9: Top: Simulated antenna input reflection coefficient  $S_{11}$  versus tuning capacitance for various frequencies. Bottom: Simulated antenna input impedance magnitude and phase at representative frequencies.

reflection coefficient versus frequency for various tunings, with both ideal capacitors and with the measured varactor S-parameters applied to the simulation. There are slight frequency shifts near the middle of the band, but the tuning range and other properties remain the same after applying the measured varactor properties.

### 3.5 Polarization Characteristics of Crossed End-Loaded Dipoles

The fabricated prototype shown in Fig. 3.8 was characterized in an anechoic chamber for its boresight radiation characteristics across its possible frequency range as well as its radiation pattern at the representative frequency of 250 MHz. Although there was limited time on the equipment, the measurements that were completed sufficiently demonstrated that the antenna performed as predicted by the simulations. Fig. 3.13 shows the measured boresight circularly polarized realized gain, as well as the axial ratio, versus frequency for various tuning configurations. Simulations, with capacitances chosen from the simulated impedance curves, predicted the gain to be in the vicinity of 7 dB across the band, with axial ratios better than 2 dB. Measurements largely confirmed these predictions: when tuned to operate around 240 MHz and 280 MHz, the measured realized gain was excellent at 7 dB or more, and the axial ratio was better than 1 dB. At 260 MHz, however, the gain is a more modest 5 dB, likely a result of imperfect tuning, also evidenced by the axial ratio values of 3-4 dB.

Table 3.1 shows the tuning voltages applied to the antenna that yielded the results shown in Fig. 3.13. These values were obtained by adjusting the tuning voltages to maximize the received power from a helical antenna used as a circularly polarized source. An alternative way of finding the required bias voltages would be to measure the antenna's input impedance while adjusting the tuning voltages, producing curves analogous to the simulated traces in Fig. 3.9 but with respect to biasing voltage rather than capacitance. The appropriate voltages to yield the desired polarizations could be deduced from these curves. Fig. 3.14 shows the measured realized gain patterns and axial ratio patterns at 250 MHz for four azimuth angles. Note that the axial ratio is better than 4 dB over nearly a 90°



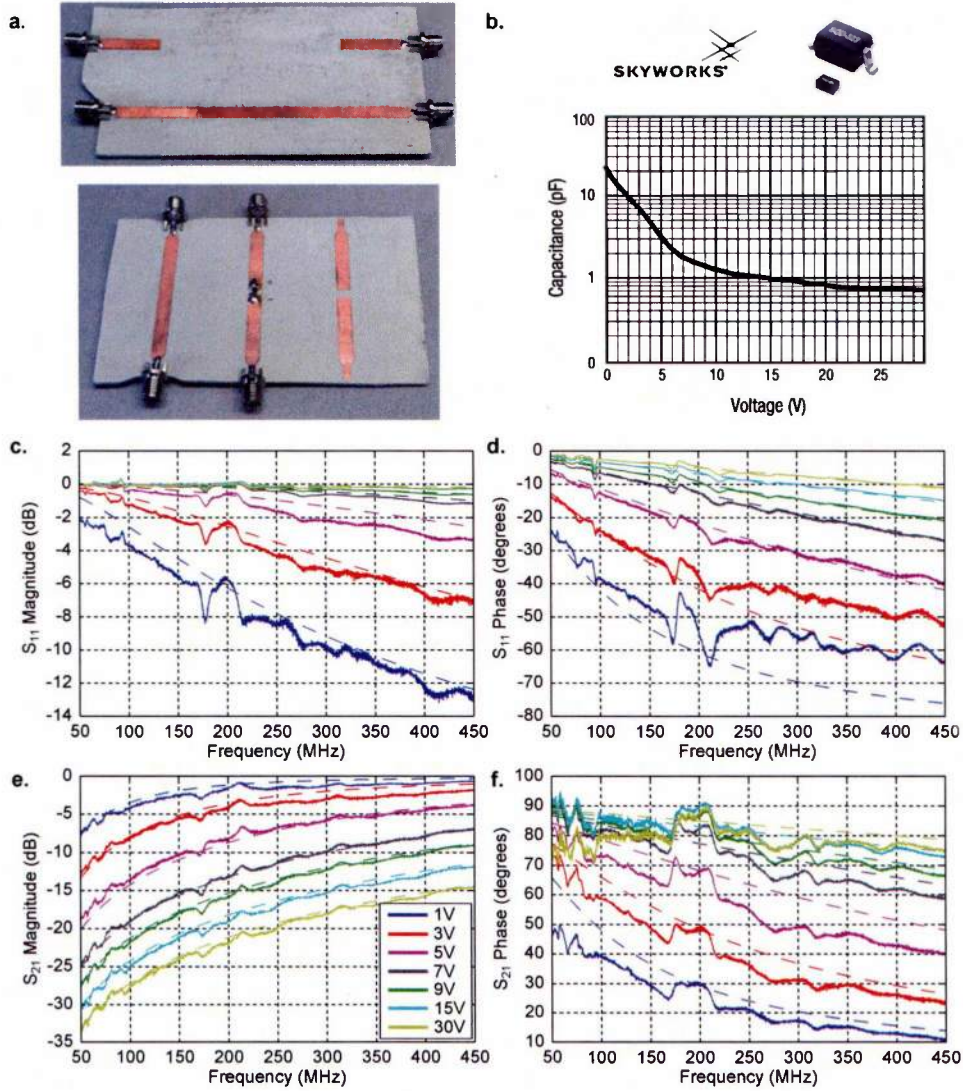


Fig. 3.10:  $S$ -parameter measurements of a Skyworks SMV1265 varactor diode. (a) Photographs of the test board, including the calibration standards. (b) Varactor capacitance as a function of reverse bias voltage, taken from the varactor datasheet. (c)-(f) Magnitude and phase of the reflection and transmission coefficients for the measured varactor (solid) and ideal capacitor with capacitance determined by the curve in (b).



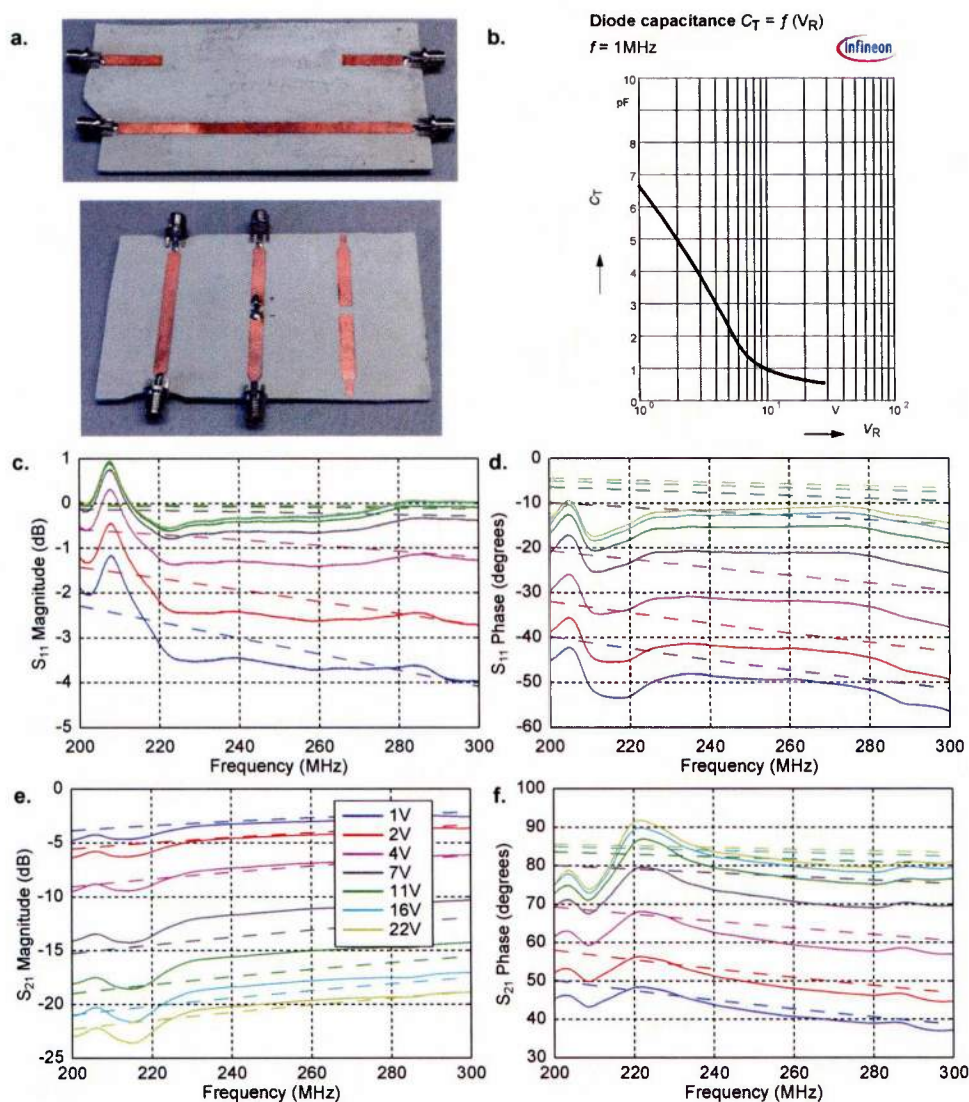


Fig. 3.11:  $S$ -parameter measurements of an Infineon BB857 varactor diode. (a) Photographs of the test board, including the calibration standards. (b) Varactor capacitance as a function of reverse bias voltage, taken from the varactor datasheet. (c)-(f) Magnitude and phase of the reflection and transmission coefficients for the measured varactor (solid) and ideal capacitor with capacitance determined by the curve in (b).

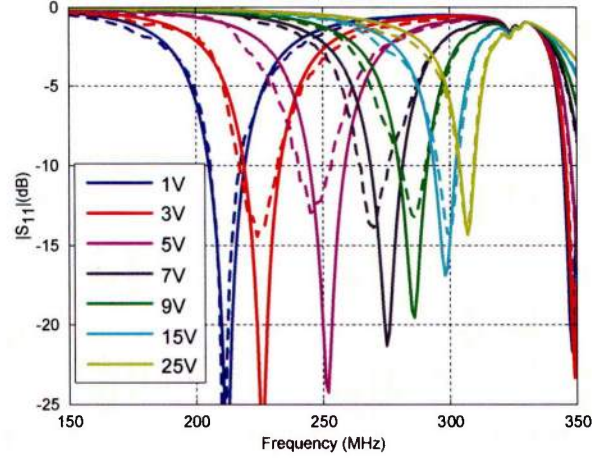


Fig. 3.12: Simulated reflection coefficient for the crossed ELDs with ideal capacitors (solid) and measured Skyworks SMV1265 varactor properties (dashed).

Table 3.1: Tuning voltages applied to the antenna when measuring the results shown in Fig. 3.13.

Target Frequency	$V_{ELD_1}$	$V_{ELD_2}$
240 MHz	0.0 V	3.7 V
250 MHz	1.8 V	5.2 V
260 MHz	2.6 V	7.8 V
270 MHz	4.3 V	9.8 V
280 MHz	6.6 V	11.9 V
290 MHz	9.0 V	18.7 V

beamwidth and the 3 dB beamwidth is more than  $90^\circ$  as well. Finally, note that the curves for the various azimuth angles nearly overlay each other, indicating a high degree of axial symmetry in the beam.

### 3.6 Summary

Tunable crossed dipole antennas can produce a wide variety of dynamically reconfigurable beam polarizations without the need for electronically controlled phase shifters. Instead, this design incorporates relatively inexpensive components, such as varactor diodes, appropriate for applications where the power levels remain on the order of Watts or below, to perform all the tuning necessary for both frequency

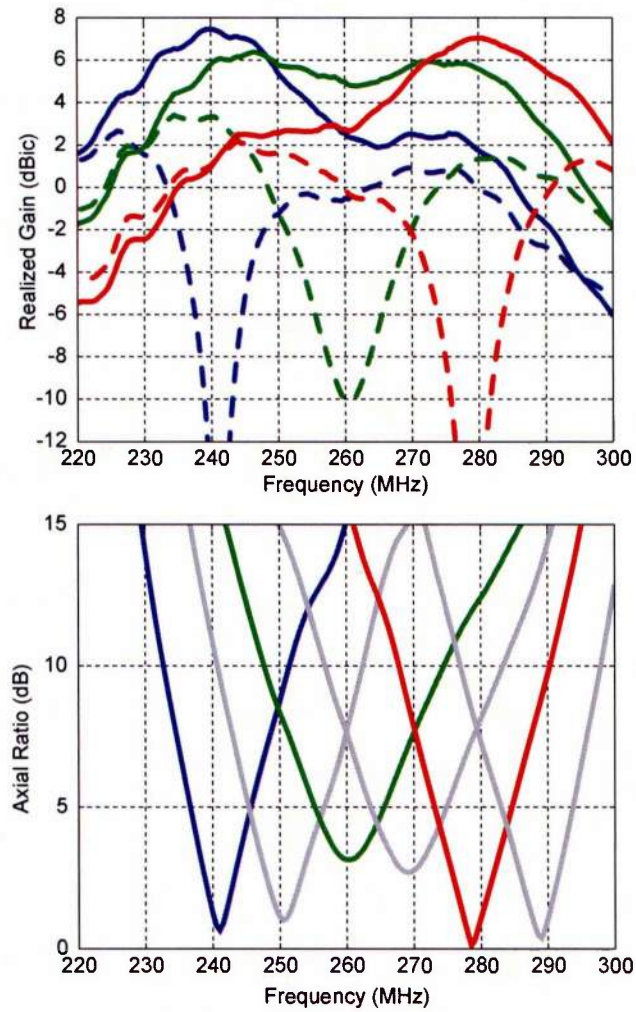


Fig. 3.13: Top: Measured boresight antenna realized gain versus frequency for representative tuning configurations. Solid curves represent the left-handed circular component while dashed curves represent the right-handed component. Bottom: Measured boresight axial ratio versus frequency for various tuning configurations. Colored curves correspond to their counterparts above.

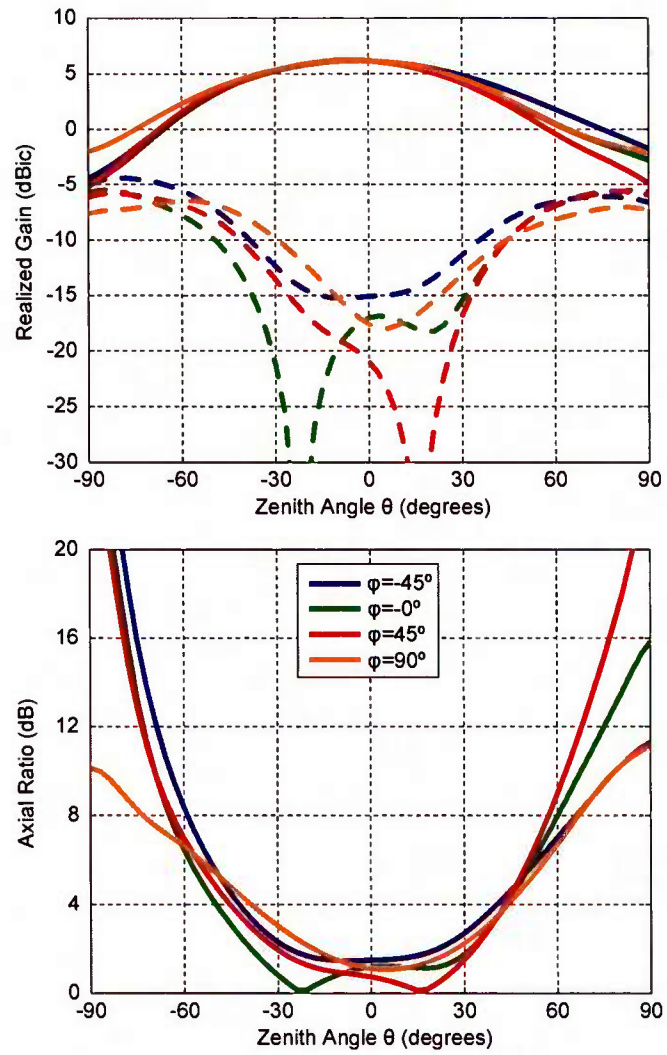


Fig. 3.14: Top: Realized gain pattern at 250 MHz for various azimuth angles. Bottom: Axial ratio pattern at 250 MHz for various azimuth angles.

agility and polarization configuration. Measurements of a prototype confirmed the antenna's performance and tuning capabilities over approximately a 20% total bandwidth.

# Compact Low-Profile Tunable Metamaterial Antenna with Near-Arbitrary Polarization

## 4.1 Introduction

Artificial magnetic conductors (AMCs) and high-impedance surfaces have garnered a great deal of attention over the past decade [26], [31], [66], as researchers have investigated their theory and application, expanding on the original works by Yang [14] and Sievenpiper [13]. One of the most prominent applications of AMCs proposed in the early papers is for reducing the height profile of horizontally polarized antennas. Antennas become inefficient radiators when placed close and parallel to an electric conductor, but their efficiency can be largely restored when placed atop an AMC. The instantaneous bandwidth of an AMC is inherently limited, with the more extreme thickness reductions generally corresponding to narrower bandwidths. Several authors have explored tunable AMC surfaces beneath broadband antenna elements [67]–[71]; such an approach allows for a narrow instantaneous operating channel that can be tuned across a much wider communications band. These works have achieved height profile reductions, but their broadband antenna elements still require large lateral dimensions. In this work we employ compact, tunable antenna elements above a tunable AMC to achieve size reductions for both



the antenna's height and lateral dimensions. Conventional AMC structures would result in just a few unit cells beneath the miniaturized antenna elements, and thus would present a rather inhomogeneous interface to the antenna elements above. In this work, we use a miniaturized, intertwined unit cell design inspired by [31] to provide a much more homogeneous substrate to the antenna elements. In order to control the antenna polarization, we adjust tunable capacitors on crossed end-loaded dipoles placed above the AMC substrate, tuning the electrical length and thus the input impedance of each dipole, analogous to what Bolster accomplished by varying the physical dimensions of crossed dipoles to create circular polarization [59]. This approach allows for a variety of polarizations, including left- and right-hand circular, as well as linear with various orientations, all from a single feed that need be no more complex than a balun. An important simulation technique that was essential to this work was presented by Bray and Werner in [69] and employed in similar works such as [72], [73]; an entire antenna and AMC structure is simulated with lumped ports placed at the feed and at each lumped element loading point. The simulation then results in a (potentially large) S-parameter matrix, to which the appropriate S-parameters from the desired loading elements are applied to reduce the matrix and estimate the impedance of the antenna at its feed. This approach allows a single simulation to be run, taking as many as several days to complete, after which the effect of a multitude of capacitance values on the antenna input impedance can be quickly calculated or even optimized.

## 4.2 Preliminary Work

### 4.2.1 Initial AMC Design

An initial design for the AMC surface consists of the periodic unit-cell shown in Fig. 4.1. The copper traces on the unit cells are interconnected to reduce their periodicity and thus increase homogeneity. Adjacent cells are further connected by varactor diodes, which provide an electrically tunable capacitance for adjusting the operating frequency (channel) of the AMC surface. The substrate chosen is Rogers 5880 LZ, which has an electric permittivity of 1.96 with minimal dielectric loss. Fig. 4.2 shows that the AMC exhibits an operational band that is tunable



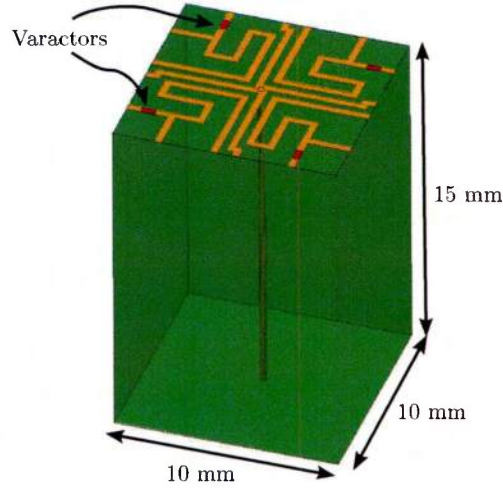


Fig. 4.1: Initial AMC unit cell structure and dimensions. The unit cell consists of a patterned copper layer with vias through a Rogers 5880LZ substrate to a conducting ground plane.

from about 150 to 435 MHz using commercially available varactors tuning from 2 to 18 pF. Depending on the desired antenna performance, absorption becomes a significant factor when operating below about 250 MHz. Absorption depends most strongly on the width of the resonant response, which in turn depends on the thickness of the substrate. As the substrate thickness decreases, the resonance narrows, increasing the absorption at the operating frequency. This effect is also visible when the surface is tuned to operate at lower frequencies, where it becomes thinner in terms of wavelength. The chosen thickness of 15 mm represents a compromise between reducing the material size while allowing low to moderate absorption.

#### 4.2.2 Tunable End-Loaded Dipole (ELD)

The end-loaded dipole (ELD) is a convenient miniaturized antenna for this application because it can be small (approaching as little as  $\lambda/10$  in length) and is easily tunable with varactor diodes, placed as shown in Fig. 4.3. It consists of a center-fed wire or trace with meandering traces at the ends of the wire to shorten its length below the usual  $\lambda/2$  required for a dipole. In free space, this ELD gives

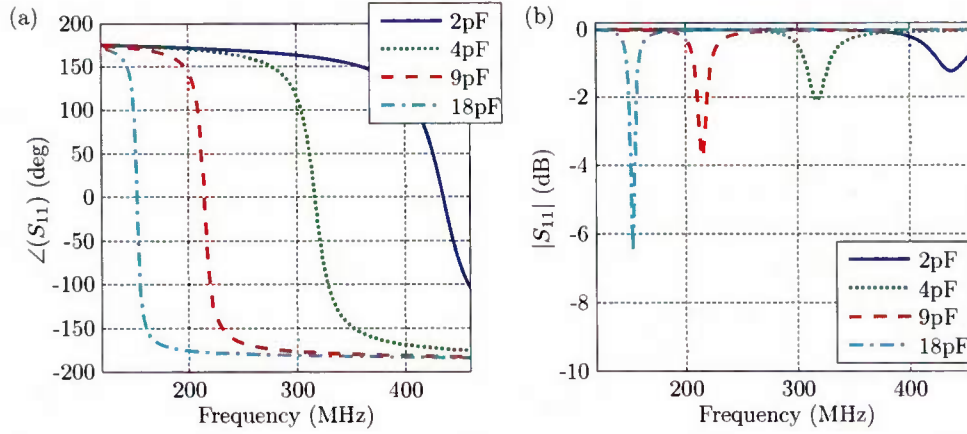


Fig. 4.2: Simulated AMC tuning performance as the varactor capacitance changes from 2 to 18 pF. Reflection coefficient (a) phase and (b) magnitude. The AMC channel can be tuned from approximately 150 to 435 MHz with instantaneous bandwidths ( $\pm 45^\circ$ ) ranging from 2 to 17 MHz (1.3-3.9%). Absorption becomes quite significant at the lower frequencies, but more than half of the incident power is reflected above about 250 MHz.

a simulated peak gain of 1.22 dB (peak directivity of 2.08 dB).

When placed 5 mm above a PEC ground plane, the gain drops dramatically to less than -20 dB. By placing a small section of perfect magnetic conductor (PMC) directly beneath the ELD, the gain is restored and even increased slightly to 2.75 dB (directivity of 5.76 dB). Fig. 4.4 shows the E- and H-plane radiation patterns for the ELD above a PMC section on a larger PEC ground plane at 400 MHz and the reflection coefficient magnitude for the ELD over a PMC with different capacitance values for the varactors (tunings). The ELD shows operation over the range from about 330 to over 400 MHz with instantaneous bandwidths of 1 to 2 MHz. These very preliminary design and simulation results led into the revisions shown in the final design that follows.

### 4.3 Final Antenna Geometry

The final antenna considered herein was designed for operation over a UHF satellite communications band from approximately 240 MHz to 270 MHz, where conventional alternatives often require total height profiles of 15-20 cm or more in order

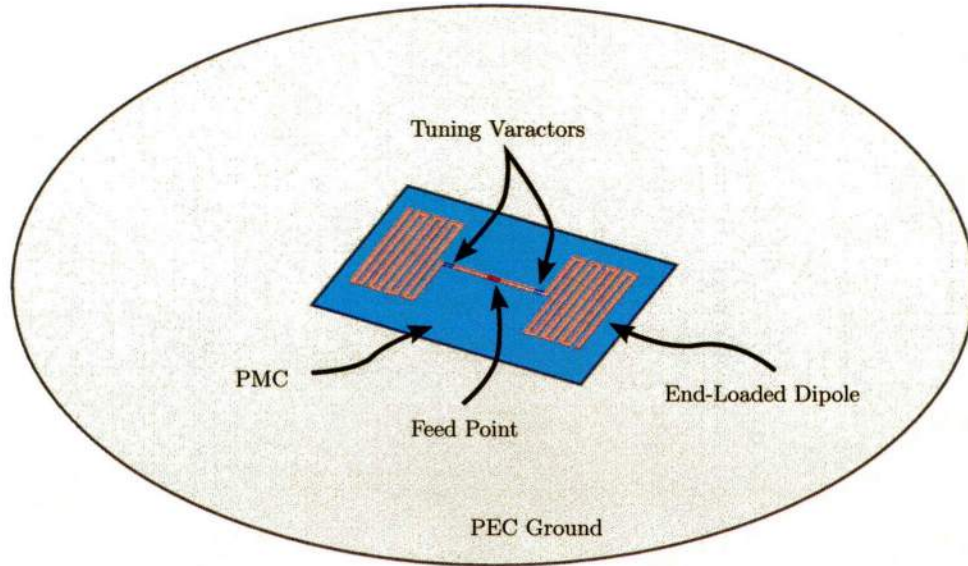


Fig. 4.3: End-loaded dipole (ELD) geometry when placed over a small section of a perfect magnetic conductor (PMC) embedded in a larger section of a perfect electric conductor (PEC). The entire ground plane is about 50 cm across.

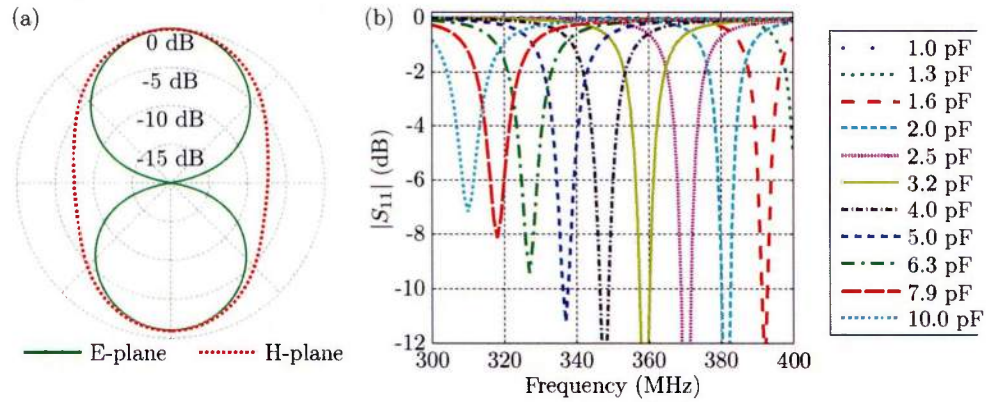


Fig. 4.4: Simulation results corresponding to the geometry in Fig. 4.3. (a) Radiation pattern. The pattern is very similar in the absence of the PEC. (b) Reflection coefficient magnitude with tuning. As the varactors are tuned from 1 to 10 pF, the operating frequency shifts from over 400 MHz down close to 300 MHz. These curves assume that a matching network can transform from a standard transmission line to an impedance with a real part around  $15\text{--}20\Omega$ .

to achieve a modest realized gain of a few dB over a reasonable bandwidth. This work aimed to maintain comparable performance to the existing antennas while dramatically reducing the height profile required. The final antenna prototype achieved these goals, having a height profile less than 5 cm. Fig. 4.5 shows photographs and dimensions of the overall antenna prototype, including the intertwined tunable AMC and the tunable crossed end-loaded dipoles. The dipoles are composed of 1 oz. copper traces on a 0.020 in. thick and 35.6 cm square FR4 substrate, which is elevated 1.5 cm above a 40.6 cm square section of AMC substrate. The AMC pattern is composed of 1 oz. copper traces on a 0.020 in. thick FR403 substrate, which is then connected by AWG18 copper wire vias to the ground plane beneath. The ground plane is actually a double-layered board, with every other via connected to alternate sides of the board. The tunable capacitors on the AMC are Infineon BB857 varactor diodes, and they are oriented so that every other via is connected to either a DC ground or the tuning voltage VAMC.

Fig. 4.6 shows detailed dimensions and the structure of the end-loaded dipoles and the intertwined AMC. The vias connect to the AMC pattern in the center of the unit cell. The AMC pattern was initially designed as a pixilated structure on a 32 by 32 pixel grid. The design was refined to have beveled edges for manufacturing, as well as appropriately sized solder pads for the varactor diodes.

A single coaxial cable feeds the center of the dipoles, where a Mini-Circuits TC1-1-13MG2+ 1:1 RF transformer is used as a balun. The tunable capacitor on each leg of each dipole is an Infineon BB857 varactor diode, which can be tuned from several picofarads down to approximately 0.6 pF across a range from 0 V to 30 V. Placing the tuning capacitors adjacent to the meandered end-loads maximizes the tuning range of the antenna, as opposed to placing the capacitors closer to the feed point or within the end loads. The feed point is connected to a DC ground through a bias tee on the feed line, and the DC tuning voltages are applied to the varactor diodes through the end loads. The center pin of a coaxial cable provides the DC bias to each end-load, where a 390 nH series choke inductor and a 2,200 pF shunt-to-ground capacitor reduce the RF energy propagating out the bias lines by more than 30 dB. The capacitor is placed between the biasing line and the outer sheath of the coaxial cables just before connecting to the choke inductor; the outer sheath of each coaxial cable is then connected to the ground



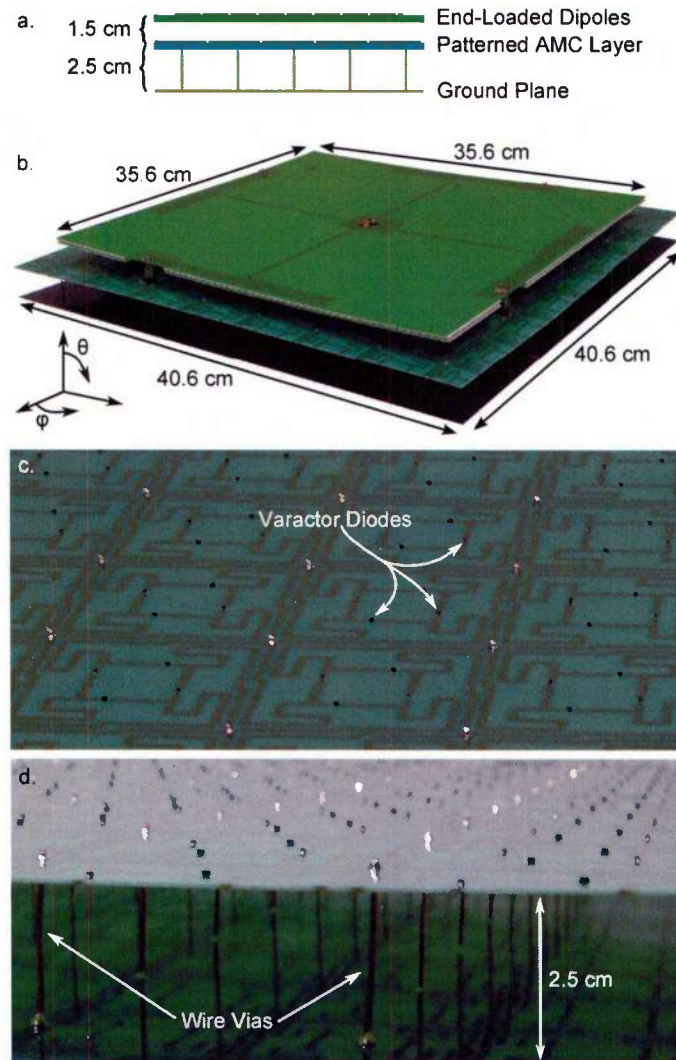


Fig. 4.5: Antenna geometry and photographs. (a)-(b) Overview dimensions of the antenna. While the thickness from the ground plane to the ELDs is 4 cm, the total antenna thickness approaches 4.5 cm when including circuit components on both the top and bottom circuit boards. (c)-(d) Photographs of details of the tunable AMC.

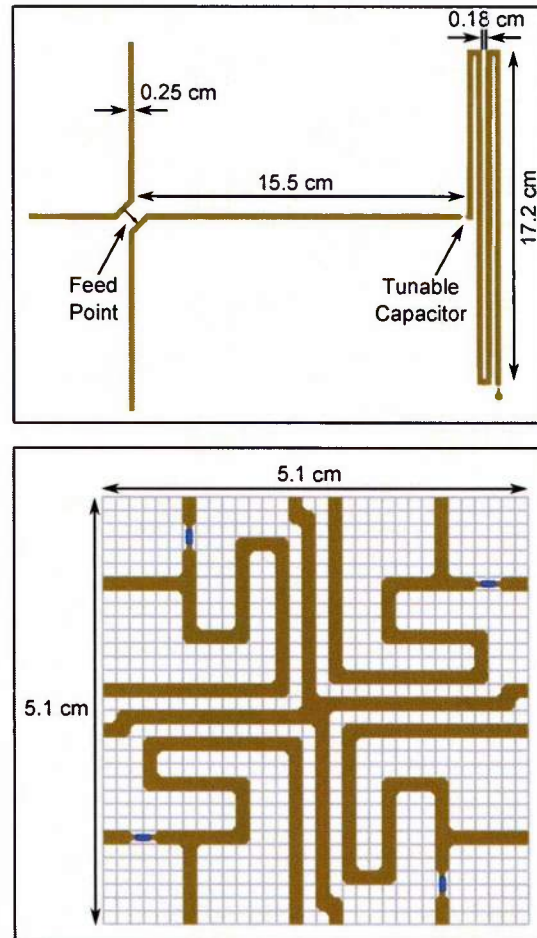


Fig. 4.6: Detailed dimensions of the ELD (top) and AMC unit cell pattern (bottom). The AMC pattern was initially designed as a 32 pixel square unit cell, but the corners were beveled and the capacitor connection pads sized appropriately for manufacturing, as shown. The blue patches represent the locations of the tunable capacitors (varactor diodes).



plane of the AMC layer.

## 4.4 Simulated AMC Performance

The primary characteristic of interest for the AMC is the reflection phase for a wave incident upon the AMC structure. Fig. 4.7 shows both the reflection phase and magnitude for the AMC structure for both varying tuning capacitance and varying total thicknesses. As a reference, the thickness chosen for the antenna prototype was 2.54 cm, as shown in Fig. 4.5. Although the antenna targeted a UHF satellite communications band from approximately 240 MHz to 270 MHz, the AMC design can be tuned to operate over more than an octave. The phase curves in Fig. 4.7 show that the operating point of the AMC, where the reflection phase angle passes through 0°, can be tuned from less than 150 MHz to more than 350 MHz, all using a capacitance range that is readily available from commercially available varactor diodes. If the thickness of the AMC structure is increased, then the tunable range increases to nearly two octaves from the same capacitance tunings, while the instantaneous phase bandwidth for a given tuning configuration also increases.

The lower half of Fig. 4.7 shows the reflection magnitude for the same variety of tuning capacitances and AMC thicknesses. The reflection magnitude is important because it indicates the relative level of RF energy that is absorbed by the AMC. Although the 1.27 cm thick structure would enable an antenna with the smallest height profile, a reflected wave below 200 MHz is reduced by more than 1 dB from that of the incident wave, and by more than 0.5 dB at frequencies up to 325 MHz. In contrast, the 7.62 cm thick AMC leads to less than a 0.2 dB reduction from the incident power, even at its worst case at the lowest frequencies. The 2.54 cm thick configuration represents the approximate point at which increasing thicknesses only lead to marginal improvements in the AMC absorption, while also exhibiting losses with a worst case of 0.5 dB decreasing to less than 0.2 dB at the upper frequencies. Moreover, the 2.54 cm thickness provides adequate phase bandwidths as well as the potential for dramatic antenna profile reductions, as it represents a mere  $\lambda/75$  at 150 MHz, and  $\lambda/50$  at the lower end of the UHF satellite communications band targeted by this work.

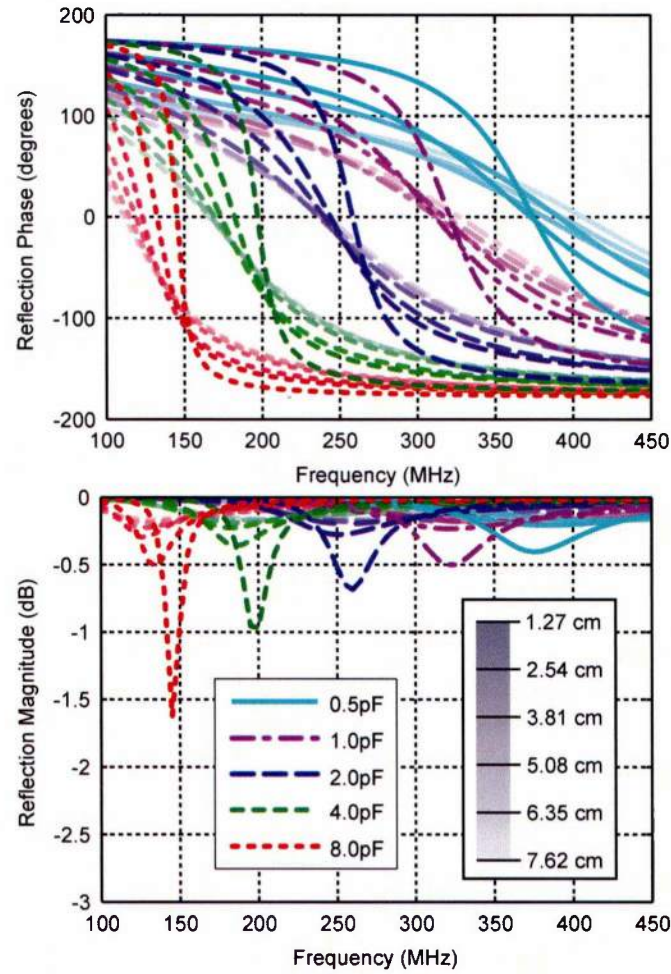


Fig. 4.7: Simulated AMC unit cell reflection phase (top) and magnitude (bottom) for various tuning capacitance values and various total thicknesses of the structure. The AMC can be tuned to operate over a range of one to two octaves, depending on its total thickness. The various tuning capacitance values are represented by various line styles and colors, while the curves for the various thicknesses have varying shadings.

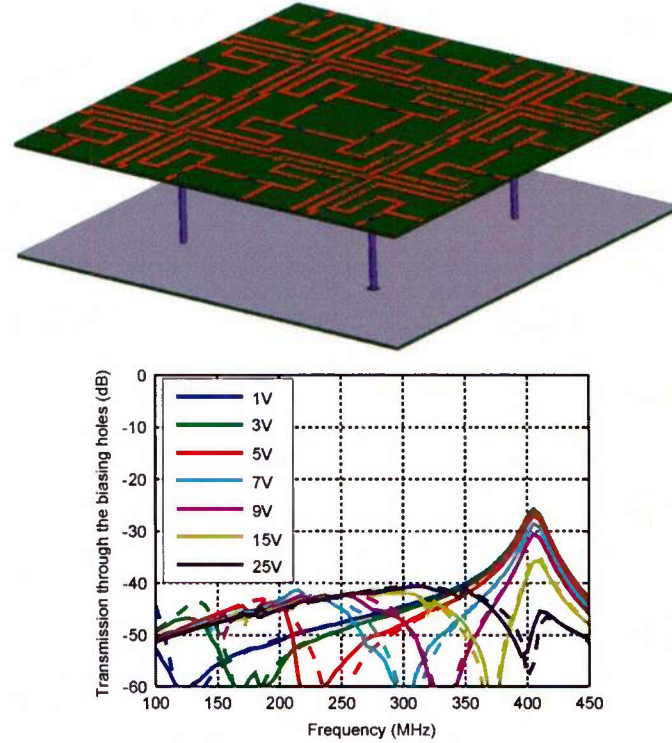


Fig. 4.8: Geometry (top) and simulated results (bottom) of a set of four unit cells including the biasing ground planes.

Because the wire vias provide biasing voltages to the varactor diodes on the unit cells, and thus alternate vias connect to alternate ground planes, there are small holes where some RF energy could conceivably propagate around a via and into the gap between the ground planes, and then out the gap between the next adjacent via and the lower ground plane. Fig. 4.8 shows a simulation of a combination of four unit cells to include these effects. For all tuning voltages, the transmission coefficient from the incident wave to the small gaps under the vias remains beneath -40 dB, indicating that using two ground planes for biasing the AMC's varactor diodes should present no problems in terms of undesired power coupling out the back of the AMC.

## 4.5 Simulated Antenna Performance

Once the AMC design was completed, a simulation of the crossed ELDs above an 8 unit cell square section of the AMC was created in Ansoft HFSS. The full simulation proved to be too large for the available computing resources, but one quarter of the structure was feasible using symmetry planes diagonal to the crossed ELDs. The structure including symmetry led to imperfections along the symmetry planes, as the AMC structure lacks any reflective symmetry, but later measurements of the antenna prototype showed that the general results of the simulations were still valid. Fig. 4.9 shows these imperfections. The antenna feed as well as all the ELD and AMC tuning capacitors were implemented in the simulation as lumped ports so that the output of the simulation was a large S-parameter matrix. The S-parameters of capacitors with various values (either ideal or measured) could then be applied to reduce the matrix to a singleton representing the antenna's input impedance. Fig. 4.10 shows the antenna input impedance magnitude and phase versus ELD tuning capacitance for various AMC tuning capacitance values and at their corresponding frequencies. In this work, we always applied a uniform capacitance value to all unit cells in the AMC while varying those on the ELDs. In order to control the antenna polarization, we need to know the input impedance phase for a single dipole. For the plots in Fig. 4.10, the same capacitance was applied to all four ELDs, leading to an impedance value corresponding to the parallel combination of two dipoles, which in turn has the same phase and half the magnitude of an individual dipole. The phase plots show that, for example, at 235 MHz and with an AMC capacitance of 1.3 pF, ELD tuning capacitances of approximately 2.2 pF and 2.5 pF achieve a relative phase difference of 90 while having approximately equal impedance magnitudes. Applying these tuning capacitances to each of the perpendicular dipoles should then result in an equal amount of power radiated from both dipoles with a 90 phase difference, and thus a circularly polarized beam.

### 4.5.1 AMC Tolerance Analysis

In order to predict the effects of inconsistencies between the various varactor diodes across the AMC surface, numerous simulations were run with a random distribution



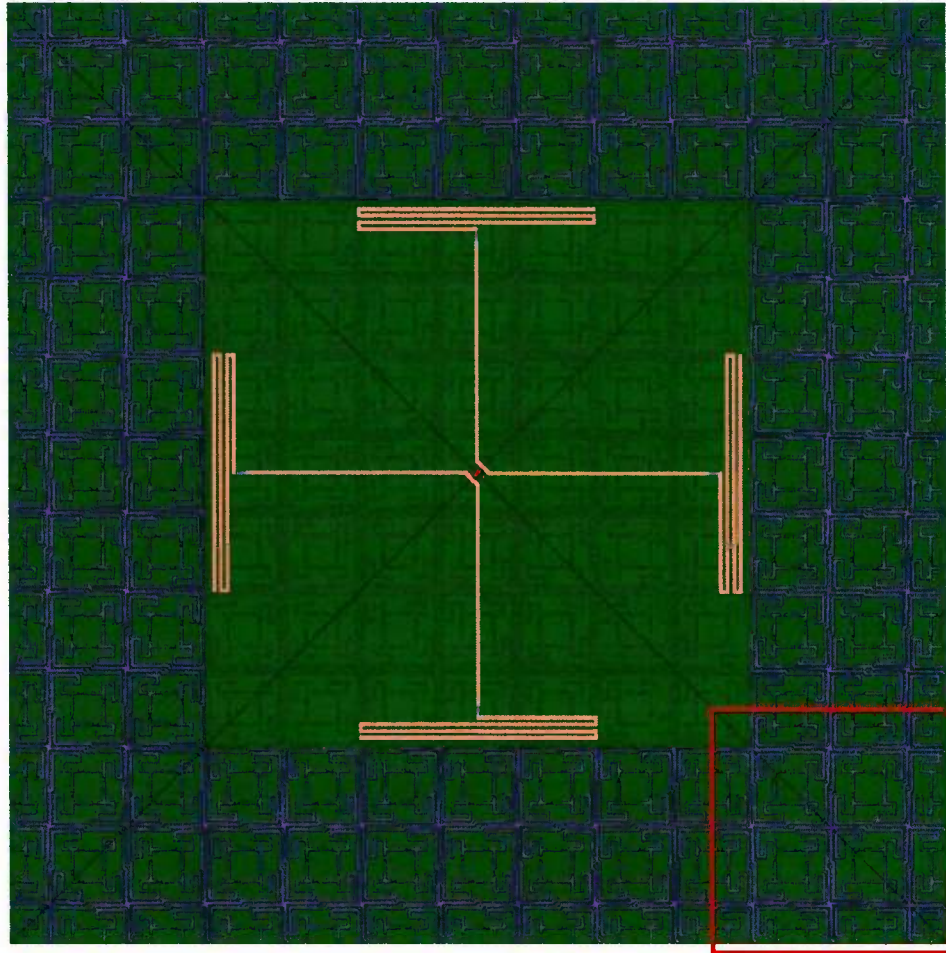


Fig. 4.9: Model view showing the imperfect symmetry in the HFSS impedance simulations; the diagonal black lines correspond to the symmetry planes. This view shows the ELDs atop a 24" square AMC so that the AMC is visible.

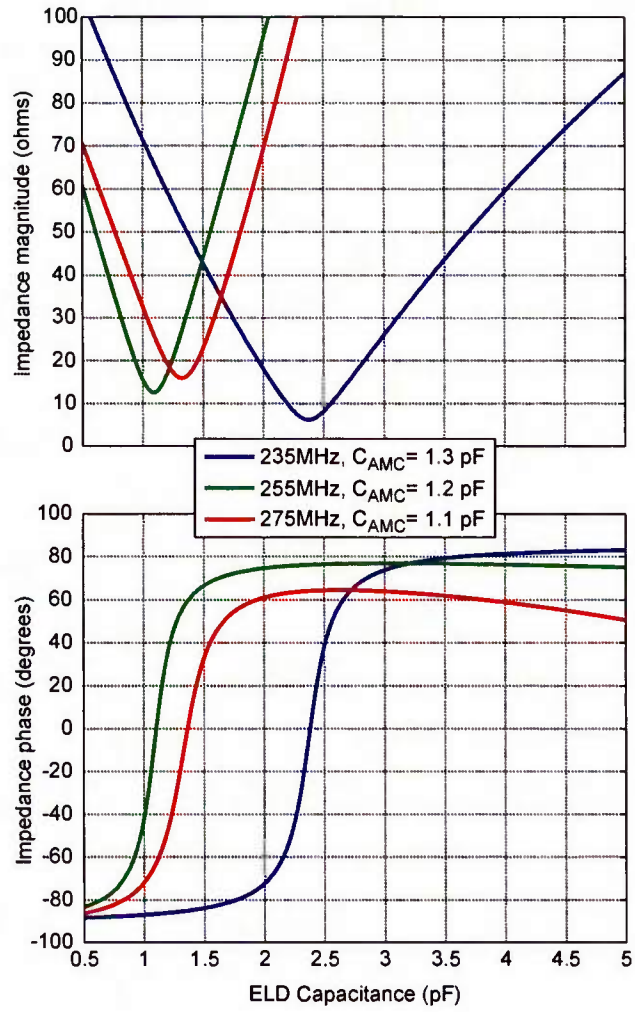


Fig. 4.10: Simulated antenna input impedance magnitude (top) and phase (bottom) versus ELD tuning capacitance at representative frequencies and their respective AMC tuning capacitances.



of capacitance values applied across the AMC. For a given percentage tolerance  $X$ , the capacitances were chosen randomly according to a uniform distribution from the nominal value minus  $X\%$  to the nominal value plus  $X\%$ . Fig. 4.11, Fig. 4.12, and Fig. 4.13 show the ELD input reflection coefficient and input admittance versus ELD tuning capacitance for ten different random AMC tunings and for tolerances of 2%, 5%, and 10%. In all cases except two variations with a 10% tolerance at 35 MHz, the reflection coefficients remain below -10dB and the phase of the input admittance follows the profile necessary to achieve polarization tuning, though the exact tuning values differ depending on the exact random configuration. These results suggest that the AMC design is robust to capacitor tolerances of 5% or better, and good performance could often be obtained even with a mere 10% tolerance.

One last aspect to consider regarding tolerances is the precision and accuracy required for the tuning voltages. Fig. 4.14 shows the capacitance versus bias voltage curve as well as its derivative with respect to bias voltage. For tuning voltages above 5 V, the capacitance changes by less than approximately 0.1 pF for each 0.1 V change in the bias voltage. Maintaining bias voltages with an accuracy of 0.1 V does not present many challenges, indicating that the tuning tolerance is reasonable. As shown in the bottom plot, for each 0.1 V change in the tuning voltage, the capacitance will not change by more than 5% across the entire tuning range, and the change will be less than 1% across more than half of the range. Although these curves are for the Skyworks varactor, the Infineon varactor diode used for the prototype AMC has even shallower slopes, meaning that its voltage tolerance characteristics will be even better.

### 4.5.2 Simulated Radiation Characteristics

A variety of polarizations can be achieved through dynamic tuning of the ELD capacitors. Left- and right-hand circular can be achieved at a desired frequency as previously described, and the sense can be changed by simply alternating which tuning capacitance is applied to which dipole. Applying the same tuning capacitance to both dipoles creates a linear polarization parallel to the feed point. Linear polarization parallel to a particular dipole can be achieved by tuning one

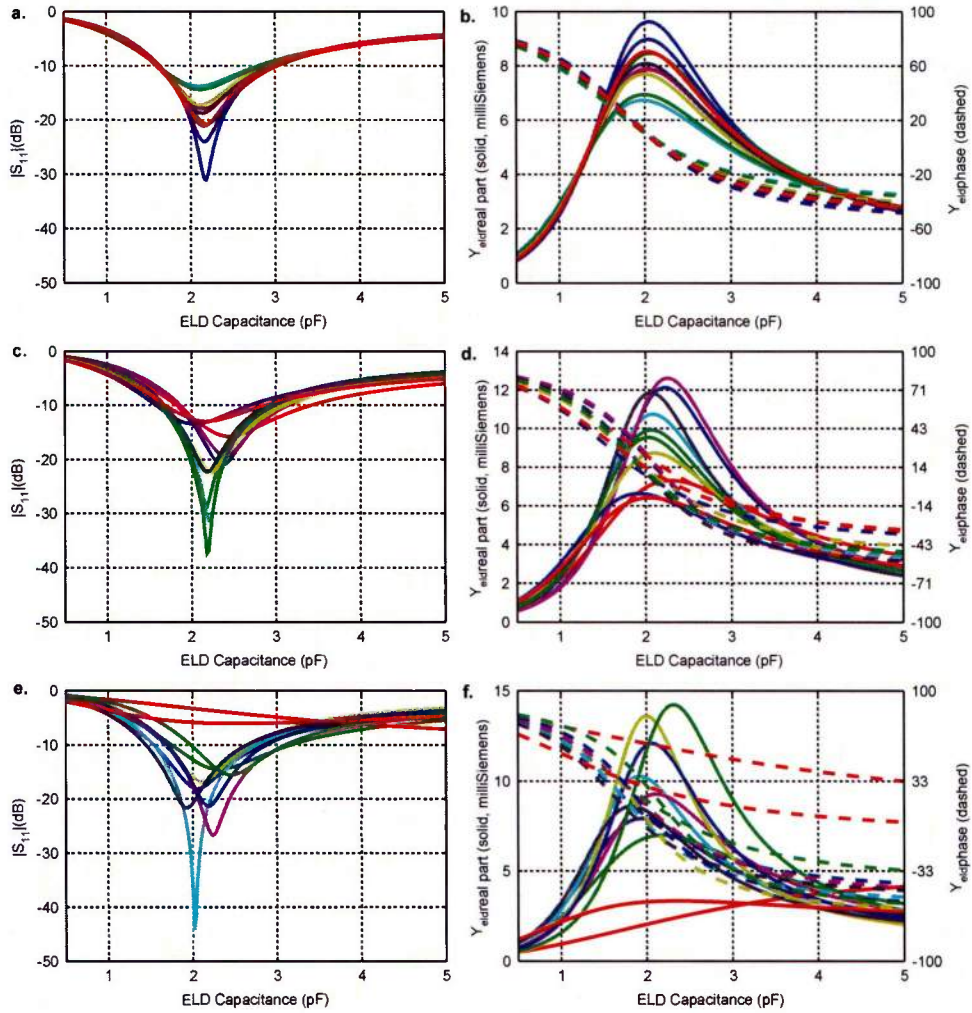


Fig. 4.11: ELD input reflection coefficient (a, c, and e) and input admittance (b, d, and f) versus ELD tuning capacitance for ten random configurations with tolerances of 2% (a-b), 5% (c-d), and 10% (e-f). These curves are all for a frequency of 235 MHz, with a nominal AMC capacitance of 1.76 pF.

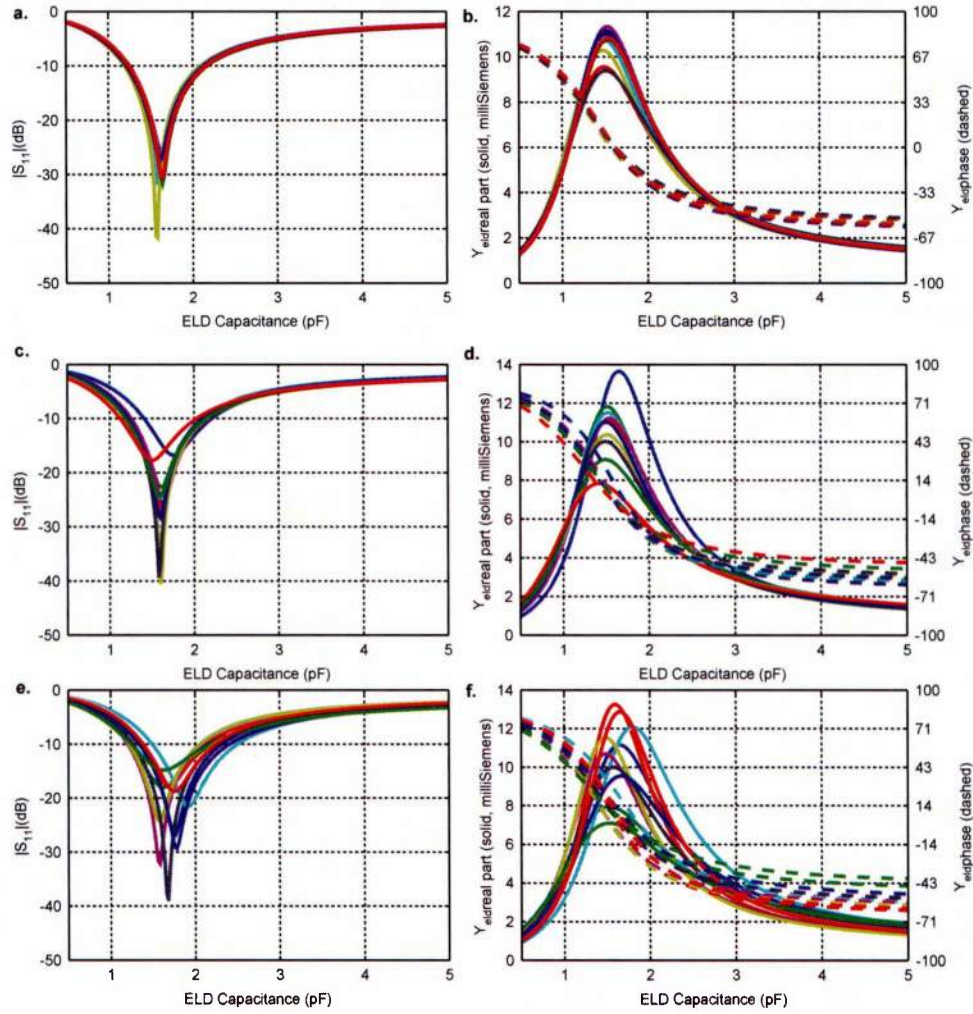


Fig. 4.12: ELD input reflection coefficient (a, c, and e) and input admittance (b, d, and f) versus ELD tuning capacitance for ten random configurations with tolerances of 2% (a-b), 5% (c-d), and 10% (e-f). These curves are all for a frequency of 255 MHz, with a nominal AMC capacitance of 1.31 pF.

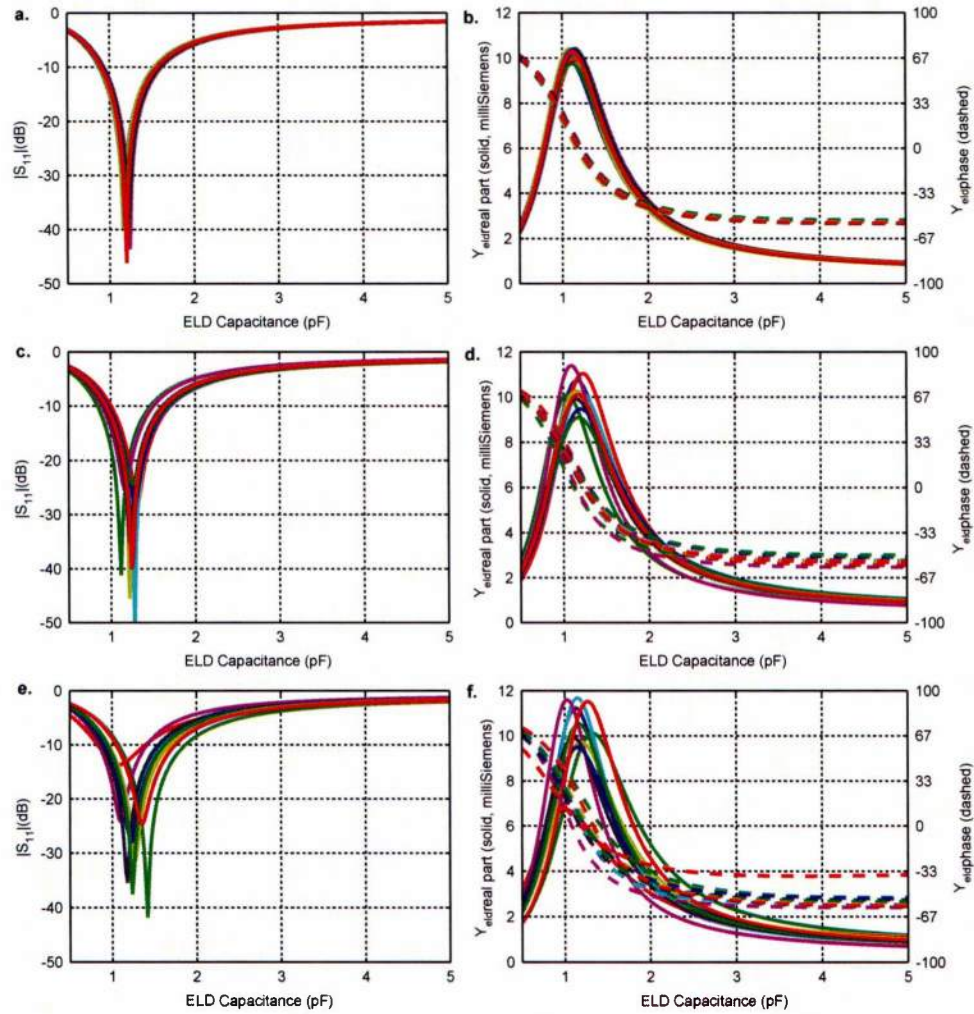


Fig. 4.13: ELD input reflection coefficient (a, c, and e) and input admittance (b, d, and f) versus ELD tuning capacitance for ten random configurations with tolerances of 2% (a-b), 5% (c-d), and 10% (e-f). These curves are all for a frequency of 275 MHz, with a nominal AMC capacitance of 0.94 pF.



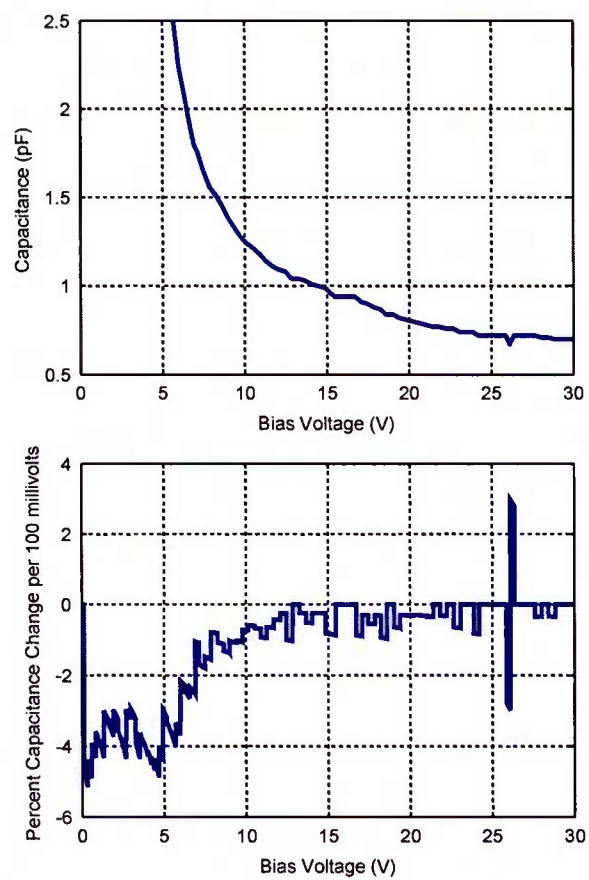


Fig. 4.14: Skyworks SMV1265 varactor diode tuning characteristics. Capacitance versus bias voltage (top) and percent capacitance change versus change in bias voltage (bottom).

dipole to have a good impedance match at the desired frequency, while tuning the other dipole to have a poor impedance match at that frequency. Linear polarization perpendicular to the feed point can be approached by increasing the phase difference between the dipoles to be as close to 180 as possible, though the impedance match of both may suffer slightly. The full antenna structure was modeled in FEKO, as the full simulation to find the radiation pattern was computationally infeasible in Ansoft HFSS, requiring hundreds of gigabytes of memory. The FEKO simulation consisted of metallic triangles for the ground plane and for the patterns of the AMC and ELDs, and the dielectric substrates were modeled using Green's functions. This setup was slightly inexact in that the simulated dielectric layers were infinite in extent, but this discrepancy had negligible effects on the simulation results. The simulated antenna was fed by a 50 lumped port. Fig. 4.15 shows the simulated left- and right-hand circular polarized radiation patterns versus zenith angle  $\theta$  for various azimuth angles. The tuning capacitances were chosen by the procedure described above for a target frequency of 250 MHz, yielding  $C_{AMC} = 1.05$  pF,  $C_{ELD_1} = 0.78$  pF, and  $C_{ELD_2} = 0.98$  pF. The curves in Fig. 4.15 predict a peak realized gain of approximately 3.5 dB, and the gain remains above 0 dB across a width of approximately  $120^\circ$ . Although the simulated cross-polarized radiation was only 8 dB down from the co-polarized component, the results showed that the general concept of achieving circular polarization from the tunable AMC and tunable antenna was valid. Operating under the assumption that refined tuning would yield even better results, production of the prototype began.

## 4.6 Measured Antenna Performance

The key differences between the simulated designs and the prototype antenna include real varactor diodes rather than ideal capacitors, as well as low tolerances on the thickness dimensions of the air gaps in the prototype. Varactor diodes can be problematic for some metamaterial designs, as the effective resistance can dominate capacitance for silicon varactors at microwave frequencies. In the upper VHF and lower UHF regime where this prototype antenna operates, however, the capacitive component dominates, and a lossless tunable capacitor is a reasonable



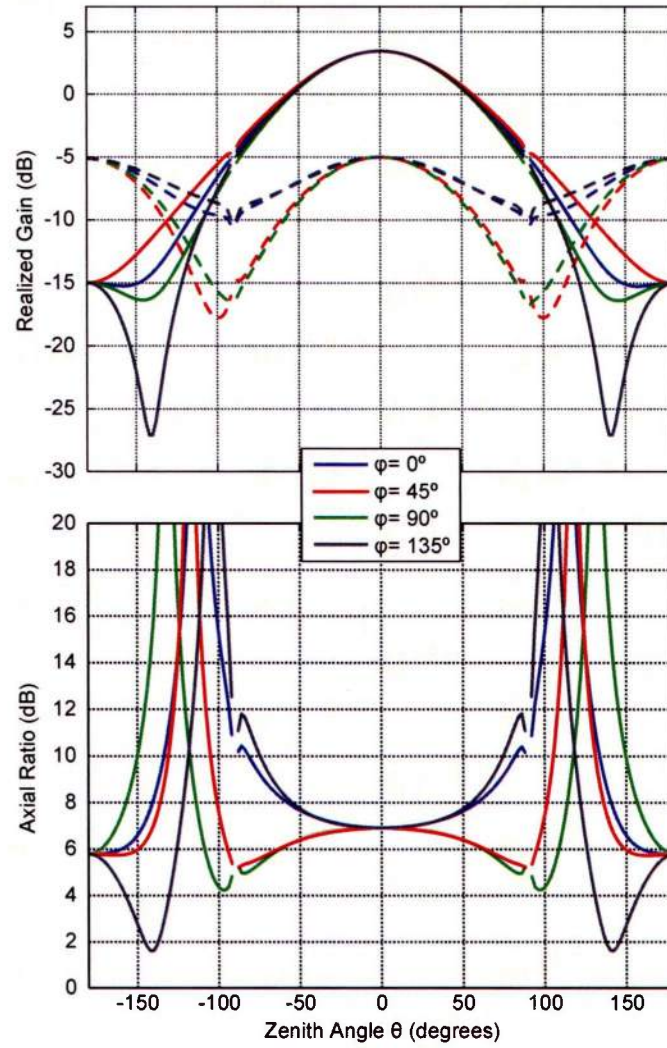


Fig. 4.15: Simulated antenna left-hand circular polarized (solid) and right-hand circular polarized (dashed) realized gain versus zenith angle  $\theta$  for azimuth angles in  $45^\circ$  increments at 250 MHz (top). Simulated axial ratio versus zenith angle  $\theta$  (bottom). The breaks in the curves at  $\theta = 90^\circ$  are an artifact of the use of the Green's function for the dielectrics in the simulated model.

approximation to a varactor. The total thickness of the AMC for the prototype stayed within 5% of the stated value of 2.54 cm, while the distance from the patterned surface of the AMC to the ELDs above remained within approximately 10% of the nominal 1.5 cm. Before characterizing the radiation pattern of the prototype, a limited set of measurements were made of its input impedance. The AMC tuning voltage was set to 12.5 V, and the ELD voltages were swept from 1 V up to 20 V. The antenna input impedance phase and magnitude measured at 245 MHz and corresponding to these tuning parameters are shown in Fig. 4.16. The capacitance of a varactor decreases logarithmically with increasing bias voltage, so the bias voltage is plotted with a logarithmic scale. The horizontal axis is thus reversed from that in Fig. 4.10, but with a largely similar scaling except above 10 V, where the varactor capacitance begins to change much more slowly, never decreasing much beneath 1 pF. This effect seems to prevent the reflection phase from quite reaching its full range shown by the simulations, but enough of the range is covered that the antenna performs admirably, as shown below. The trends in the phase and magnitude response from the simulations are clearly visible in the measured data: the impedance phase varies from approximately  $80^\circ$  at higher tuning capacitances (lower voltages) down to  $-30^\circ$  where the capacitance stops decreasing significantly with increasing voltage. The impedance magnitude is largely similar as well, showing a minimum near the point where the phase passes through  $0^\circ$ .

Although choosing the tuning capacitances from the impedance curves was an effective procedure for simulations, the numerous measurements for varying voltage levels proved impractical without an automated measurement system. In lieu of impedance curves, the tuning parameters for the antenna prototype were chosen by varying the voltages to maximize the power transmitted to a circularly polarized receive antenna. Specifically, the prototype was positioned to radiate towards a helical antenna that operated with an axial ratio better than 2 dB from approximately 220 MHz to 300 MHz, and as good as 0.5 dB in the center of the band. The AMC voltage and both ELD voltages simultaneously were first adjusted to minimize the reflection coefficient at the desired frequency. The two ELD voltages were then adjusted in opposite directions from that point to maximize the power received by the helical antenna. In some cases, it proved easier to

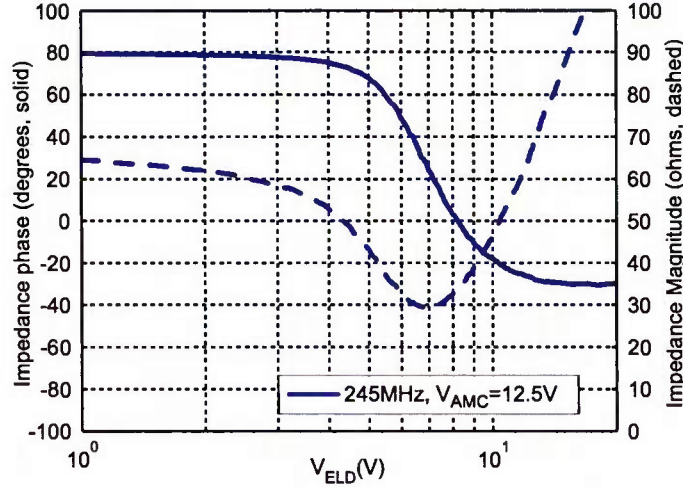


Fig. 4.16: Measured antenna input impedance magnitude (dashed) and phase (solid) versus ELD tuning capacitance at 245 MHz for an AMC tuning voltage of 12.5 V.

minimize the power received by the helical antenna and then switch the two ELD voltages, which usually produced results very close to the maximum gain. Ideally, an automated tuning system would optimize the tuning voltages, rather than the manual approach described here. Appropriate tuning voltages were determined for frequencies ranging from 220 MHz to 270 MHz in 5 MHz increments, and the measured radiation properties are shown for the representative frequencies of 230 MHz, 248 MHz, and 268 MHz in Fig. 4.17, Fig. 4.18, and Fig. 4.19, respectively. The top plot in each figure shows the measured boresight realized gain versus frequency. Each tuning configuration exhibits an instantaneous 3 dB bandwidth ranging from 5 MHz at the lower frequencies to 10 MHz at the upper frequencies. The reduced gain at nearby frequencies can serve as an early filtering stage in the communication system, although the gain often increases at other points further away, such as the peak near 260 MHz when the antenna is tuned for 230 MHz, and the peak near 280 MHz when tuned near 250 MHz.

The middle plot in each of the three figures shows the realized co- and cross-polarized gain patterns in the upper hemisphere at each of the three frequencies. The beam is very broad, as expected for a small antenna. In all cases, the gain

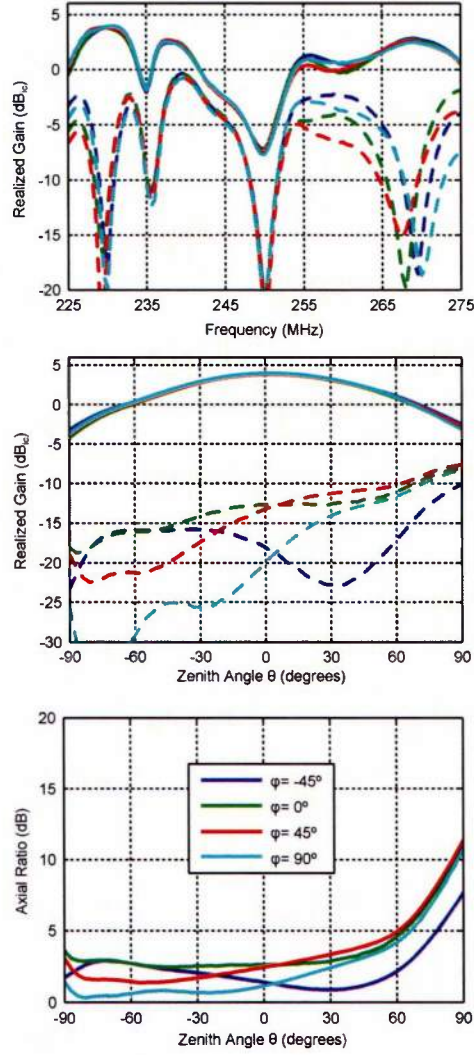


Fig. 4.17: Measured radiation properties for the metamaterial antenna tuned to operate at 230 MHz. Left-hand circular polarized (solid) and right-hand circular polarized (dashed) realized gain versus frequency (top) and versus zenith angle  $\theta$  (middle) for representative azimuth angles  $\phi$ . Axial ratio versus zenith angle  $\theta$  (bottom).

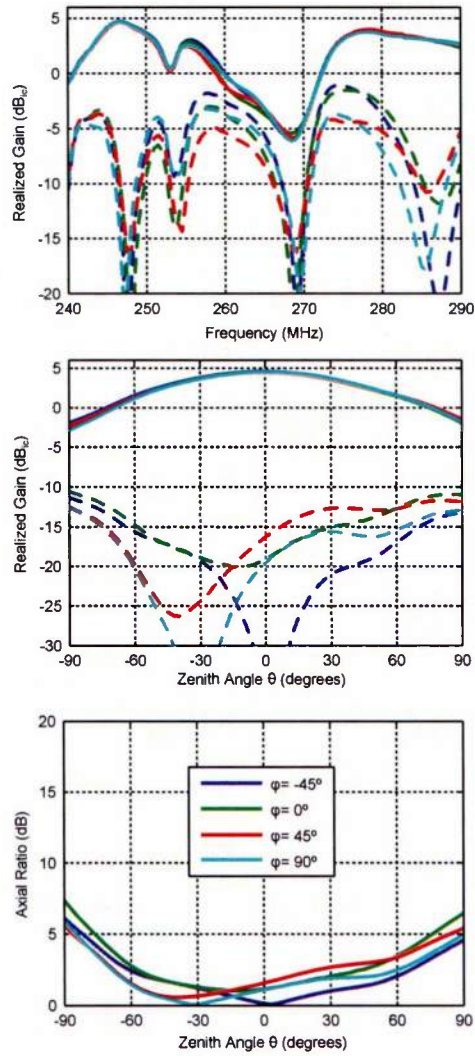


Fig. 4.18: Measured radiation properties for the metamaterial antenna tuned to operate at 248 MHz. Left-hand circular polarized (solid) and right-hand circular polarized (dashed) realized gain versus frequency (top) and versus zenith angle  $\theta$  (middle) for representative azimuth angles  $\phi$ . Axial ratio versus zenith angle  $\theta$  (bottom).



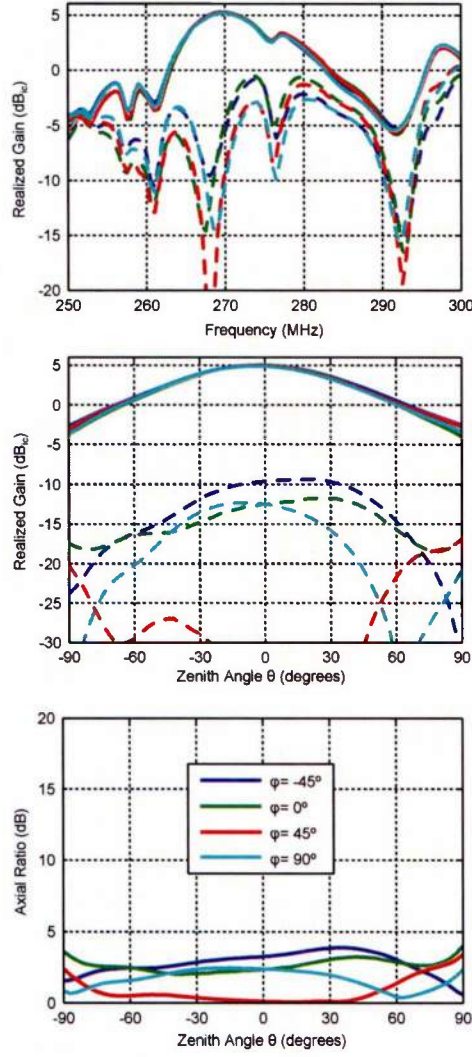


Fig. 4.19: Measured radiation properties for the metamaterial antenna tuned to operate at 268 MHz. Left-hand circular polarized (solid) and right-hand circular polarized (dashed) realized gain versus frequency (top) and versus zenith angle  $\theta$  (middle) for representative azimuth angles  $\phi$ . Axial ratio versus zenith angle  $\theta$  (bottom).



remains above 0 dB across more than a 120° beamwidth, which is nearly identical to the simulation predictions. The bottom plot in each figure shows the measured axial ratio pattern in the upper hemisphere for each of the three frequencies. The axial ratio is often better than 2 dB at boresight, and generally better than 3 dB, with relatively small increases near the horizon in most cases. It is important to note that, in the top plots of the figures, it is apparent that the frequency at which the realized gain is maximized is generally shifted slightly from the frequency at which the cross-polarized component is most strongly rejected. A more extensive study of the effects of tuning may be necessary to fully understand this phenomenon, but it would require automated test equipment in order to be practical. Applications would require slightly different tunings depending on whether peak gain or cross-polarization rejection was the priority. Fig. 4.20 summarizes the boresight radiation characteristics of the prototype antenna across much of the tunable range. The peak realized gain increases from approximately 4 dB at the low frequencies to more than 5 dB when tuned to operate at the high frequencies. The bottom of Fig. 4.20 plots the three tuning voltages leading to the radiation characteristics shown. The second ELD tuning voltage shows erratic behavior at some frequencies, which corresponds to slight decreases in the gain and axial ratio performance. Determining the optimal tuning voltages by an automated system would likely improve the antenna characteristics beyond the excellent performance already found in these preliminary measurements.

As a final consideration, the prototype antenna was connected to a spectrum analyzer and the received power level of several satellite carrier signals was found to be comparable to two commercially available antennas that were more than three times as thick as this metamaterial antenna.

## 4.7 Summary

A tunable artificial magnetic conductor (AMC) based on interconnected unit cells and a substrate consisting primarily of air provides a lightweight, homogeneous interface to compact, tunable crossed end-loaded dipoles above. The combination of the tunable miniaturized AMC with the tunable crossed end-loaded dipoles (ELDs) enables significant reductions in the antenna height profile along with

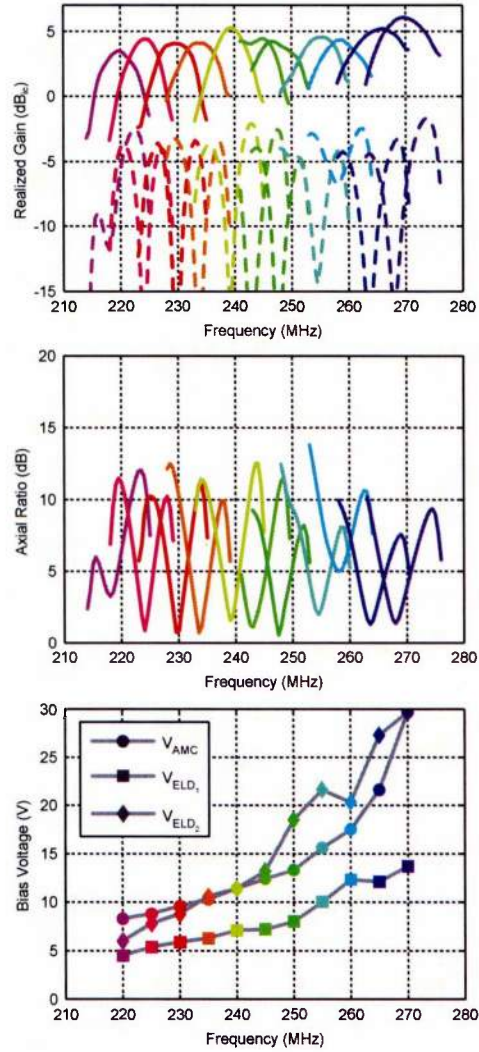


Fig. 4.20: Measured boresight radiation properties for the metamaterial antenna tuned for various frequencies across the band. Left-hand circular polarized (solid) and right-hand circular polarized (dashed) realized gain versus frequency (top). Axial ratio versus frequency (middle). Tuning voltages for the AMC and ELDs to yield left-hand circular polarization at the marked frequencies (bottom).

reductions in the lateral dimensions compared to conventional alternatives, all while maintaining comparable performance. Lastly, the tunable crossed ELDs allow for near-arbitrary dynamic control of the antenna polarization across more than a 35% bandwidth. Potential applications include vehicular and airborne platforms requiring low-profile antennas for satellite connectivity.

# Antenna Testing with Satellite Carrier Signals

## 5.1 Initial Reception Testing

In order to test the antenna in a situation nearer to a real-world application, it was connected to a spectrum analyzer and placed on a cart, facing the sky, where it could receive UHF carrier signals from active satellites. Two commercially available antennas were tested at the same time for comparison. The tests were performed in State College, Pennsylvania, and the active satellites were near the earth's equator, thus the antennas were receiving signals from approximately  $40^\circ$  away from boresight. The satellite carrier signals were from live voice feeds, and thus they varied over time; multiple tests with the same antenna could show variations as large as 2-3 dB or more. Lastly, the tuning voltages for the metamaterial antenna were those shown previously in Fig. 4.20, but several minor modifications had been made to the antenna, so those tuning voltages may have no longer been optimal. The metamaterial antenna was placed in a metal cavity like the other two antennas, but the cavity could have been less than a third of its depth without affecting the antenna performance.

Fig. 5.1 and Fig. 5.2 show the antenna set up for satellite carrier signal reception along with the measured received power compared to two conventional alternatives. The metamaterial antenna performs comparably to the other two antennas, but it

only requires a third or less of their thicknesses.

## 5.2 Bias Voltage Controlling Circuit

### 5.2.1 Circuit Design

In order to create a simple and portable method for tuning the antenna, a microcontroller-based tuning controller was designed and assembled. The controller is primarily based on a Texas Instruments MSP430G2231 microcontroller working in conjunction with an Analog Devices AD5504 4-channel digital to analog converter (DAC). The entire system is powered from a BB2590/U lithium-ion rechargeable military battery, which provides the 30 V source for the tuning voltages, as well as power for the supporting circuitry. Other components include:

- Lite-On LTM-8522HR numeric display
- LM7805 5 V linear voltage regulator
- Fairchild Semiconductor KA78R05C 3.3 V linear voltage regulator
- Several capacitors, resistors, and potentiometers

Fig. 5.3 shows the circuit diagram for the controller, and Fig. 5.4 shows the circuit board layout. Fig. 5.5 shows a photograph of the completed antenna voltage controller. The microcontroller is programmed so that the microcontroller gets the current potentiometer reading, calculates and displays the active frequency on the numeric display, and lastly communicates to the DAC to output the appropriate three voltages to tune the AMC and the two ELDs on the antenna. The range of frequencies supported by the controller goes from 240 MHz to 270 MHz.

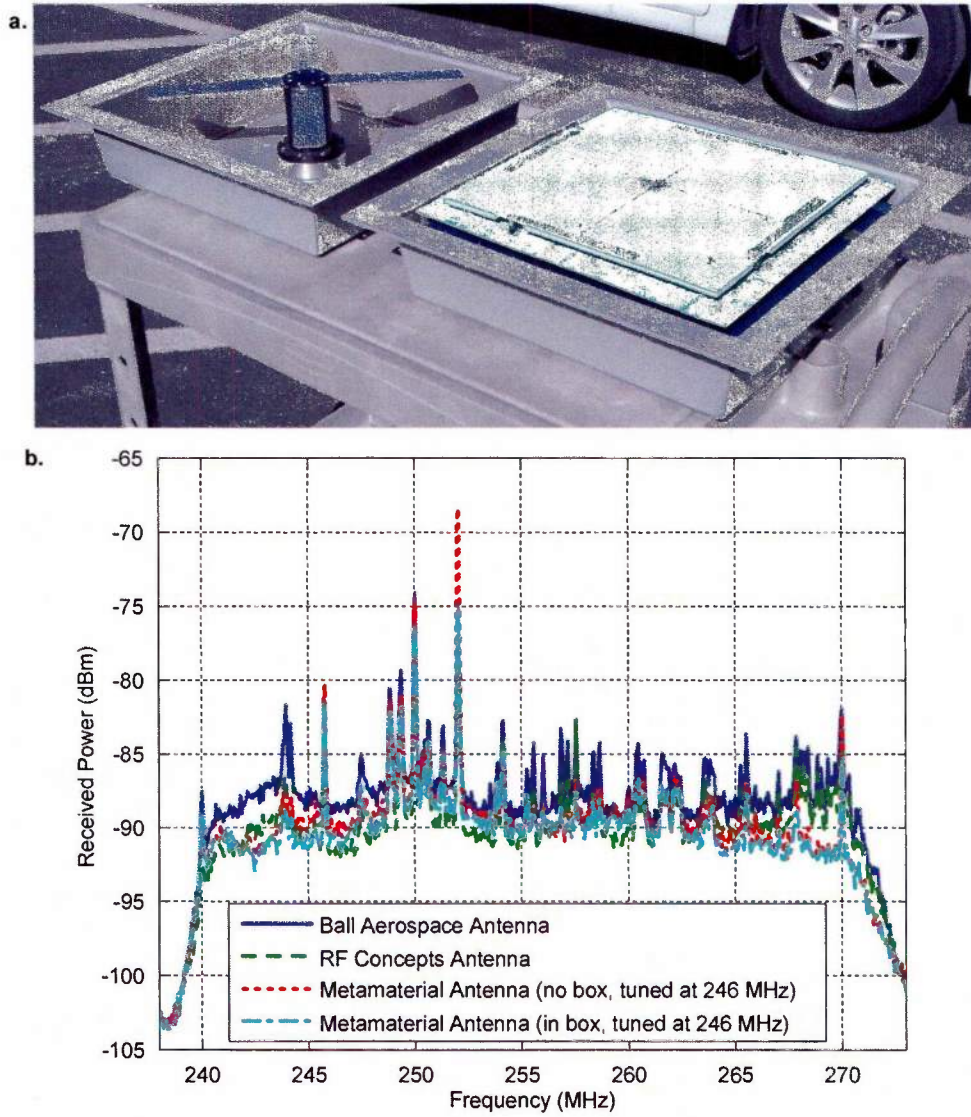


Fig. 5.1: Photograph of the metamaterial antenna and a conventional alternative, as well as the received power across the UHF satcom receive band.



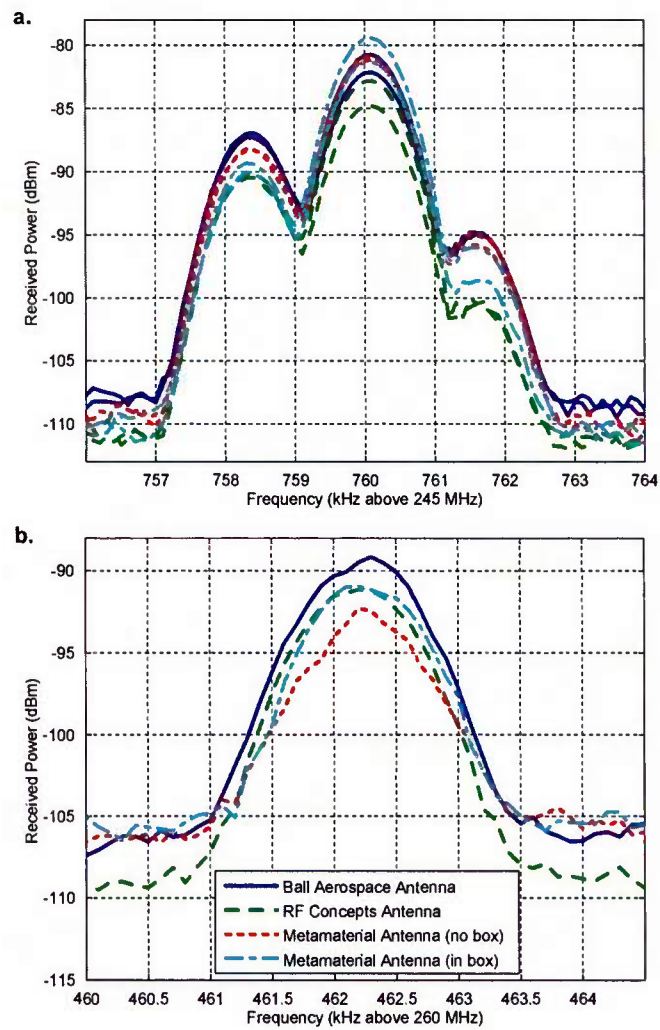
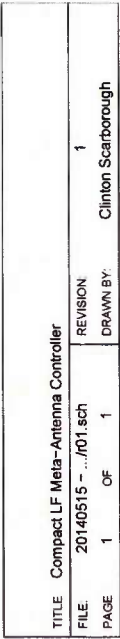


Fig. 5.2: Received power comparison between the metamaterial antenna and conventional alternatives. The metamaterial antenna's performance is comparable to the alternatives, but requires a mere third or less of their thicknesses.



79

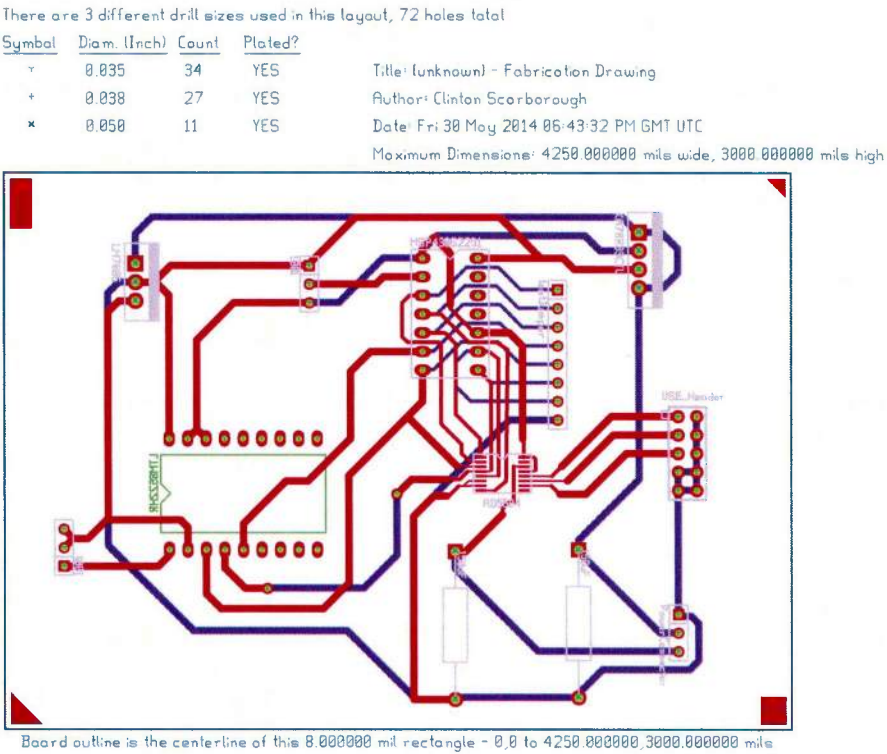


Fig. 5.4: Printed circuit board layout for the bias voltage controlling circuit.

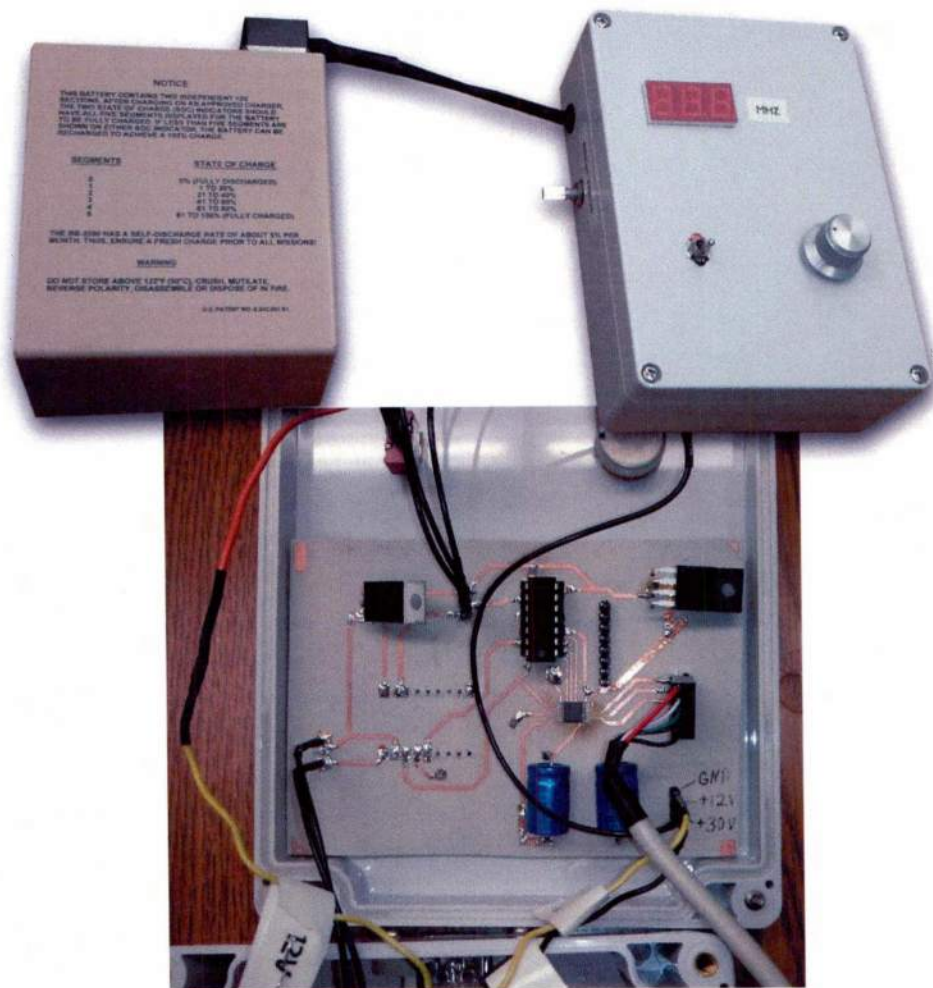


Fig. 5.5: Photographs of the antenna controller box and constituent circuitry.

The following is the source code for the Texas Instruments MSP430G2231 microcontroller that runs the antenna’s bias voltage controller box. Please do not use it as an example of good programming practices, as it was hacked together to give the desired outputs, but not refined, nor was it created by an experienced embedded systems programmer. Any real-world product would require optimizations for robustness and reduced power consumption.

Listing 5.1: main.c

```

1 // *****
2 // Voltage controller for the compact low-profile metamaterial antenna with
3 // near-arbitrary polarization
4 //
5 // MSP430C2231
6 // ^-----|
7 // | | XIN|-----> to center pin of voltage control POT
8 // | | XOUT|-----|
9 // |--|RST | | AD5504 DAC | LTM-8522HR
10 // | | | | ^-----| |-----|
11 // | P1.0|----| | | | | |
12 // | P1.1|----|---|>|~SYNC | |----|14/enable |
13 // | P1.2|----|---|>|~LDAC DAC1|---> V_AMC |----|15/data |
14 // | P1.3|----|---|>|~CLR DAC2|---> V_ELD1 |----|16/clock |
15 // | P1.4|----|---|~R_SEL DAC3|---> V_ELD2 | | |
16 // | SCLK/P1.5|---|----->|SCLK | | |-----|
17 // | MOSI/P1.6|---|---|>|SD1 | | |
18 // | P1.7|---|---|>|SD0 | | |
19 // | | | |~|ALARM | | |
20 // |-----| | |-----| | |
21 // | | | | |
22 // | |-----| |
23 // |-----|
24 //
25 // Clinton Scarborough
26 // Penn State University
27 // May 2014
28 // *****
29
30 #include <msp430g2231.h>
31
32 unsigned short frequency;
33 unsigned short lastFrequency;
34
35 #define FILTERLENGTH 1
36 unsigned short adcReadings[FILTERLENGTH];
37 unsigned short adcFilterIdx;

```

```

38
39 void ConfigureAdcVoltagePot();
40 void ConfigureDAC();
41 void sendDACcmd(unsigned short cmd);
42 void updateFrequency();
43 void displayFreq();
44 void outputVoltages();
45 unsigned char getByte(unsigned short val);
46 unsigned short getDACVoltageCmd(unsigned short voltage);
47
48 // tuning voltage tables
49 unsigned short freq[7];
50 unsigned short vamc[7];
51 unsigned short veld1[7];
52 unsigned short veld2[7];
53 void initializeTables();
54 unsigned short interp(unsigned short f, unsigned short* table);
55
56 void main(void)
57 {
58     WDCTL = WDIFW + WDTHOLD;           // Stop WDT
59
60     PIOUT = 0;
61     PIOUT |= BIT4;                     // set the display's SPI sync line high
62     P1DIR |= BIT4;                     // set the display's SPI sync line to output
63     PIOUT |= BIT2 + BIT1 + BIT3;      // set the DAC's control lines to high (LDAC,
        SYNC, & CLR)
64     P1DIR |= BIT2 + BIT1 + BIT3;      // set the DAC's control lines to output
65
66     // set up stuff for SPI
67     USICTL0 |= USIPE6 | USIPE5 | USIMST | USIOE; //enable output, master mode, clock
        , MSB first, and output enable
68     USICTL1 |= USICKPH;
69     USICKCTL = USIDIV1 + USISSEL_2;
70     // USICTL0 &= ~USISWRST;           // USI released for operation
71     // USICNT = 8;                     // init-load counter
72
73     ConfigureAdcVoltagePot();
74     ConfigureDAC();
75     initializeTables();
76
77     while (1)                          // Loop
78     {
79         ADC10CTL0 |= ENC + ADC10SC;    // Sampling and conversion start
80
81         updateFrequency();
82         if(frequency != lastFrequency)
83         {
84             lastFrequency = frequency;
85             displayFreq();

```



```

86     outputVoltages();
87 }
88     __delay_cycles(50000);
89 }
90 }
91
92 // Function to output the current frequency to the numeric display
93 void displayFreq()
94 {
95     USICTLO &= ~USISWRST;           // USI released for operation
96     PIOUT &= ~BIT4;
97
98     while (!(USIIFG & USICTL1));    // Counter clear?
99     USISRL = 0b10000000;
100    USICNT = 1;                      // re-load counter
101
102    while (!(USIIFG & USICTL1));    // Counter clear?
103    USISRL = getByte( (frequency%1000)/100 );
104    USICNT = 8;                      // re-load counter
105
106    while (!(USIIFG & USICTL1));    // Counter clear?
107    USISRL = getByte( (frequency%100)/10 );
108    USICNT = 8;                      // re-load counter
109
110    while (!(USIIFG & USICTL1));    // Counter clear?
111    USISRL = getByte( frequency%10 );
112    USICNT = 8;                      // re-load counter
113
114    while (!(USIIFG & USICTL1));    // Counter clear?
115    USISRL = 0x0000;
116    USICNT = 11;                     // re-load counter
117
118    while (!(USIIFG & USICTL1));    // Counter clear?
119    USICTLO |= USISWRST;           // hold USI
120
121    PIOUT |= BIT4;
122 }
123
124 // Return the bit sequence necessary to show the digit "val" on the numeric
    display
125 unsigned char getByte(unsigned short val)
126 {
127     if(val == 0)
128         return 0b11111100;
129     if(val == 1)
130         return 0b01100000;
131     if(val == 2)
132         return 0b11011010;
133     if(val == 3)
134         return 0b11110010;

```

```

135     if(val == 4)
136         return 0b01100110;
137     if(val == 5)
138         return 0b10110110;
139     if(val == 6)
140         return 0b10111110;
141     if(val == 7)
142         return 0b11100000;
143     if(val == 8)
144         return 0b11111110;
145     if(val == 9)
146         return 0b11110110;
147
148     // else return 'E'
149     return 0b10011110;
150 }
151
152 // Set up the analog-to-digital converter for sensing the frequency indicated by
153 // the control knob (potentiometer)
154 void ConfigureAdcVoltagePot()
155 {
156     ADC10CTL1 = INCH_0 + ADC10DIV_3; // P
157     ADC10CTL0 = SREF_0 + ADC10SHT_3 + ADC10ON;
158     __delay_cycles(1000); // Wait for ADC Ref to settle
159     ADC10CTL0 |= ENC + ADC10SC; // Sampling and conversion start
160     for(adcFilterIdx = 0; adcFilterIdx < FILTERLENGTH; ++adcFilterIdx)
161         adcReadings[adcFilterIdx] = 240 + ADC10MEM / (1024 / 30);
162     frequency = 240 + ADC10MEM / (1024 / 30);
163     lastFrequency = frequency;
164 }
165
166 // Get the new frequency reading and apply a simple infinite-impulse-response
167 // filter to reduce noise
168 void updateFrequency()
169 {
170     int temp = frequency;
171     temp *= 96;
172     temp /= 32;
173     temp += 240 + ADC10MEM / (1024 / 35);
174     frequency = temp/4;
175     if(frequency < 240) frequency = 240;
176     if(frequency > 270) frequency = 270;
177 }
178
179 // send control signals to enable the DAC
180 void ConfigureDAC()
181 {
182     sendDACcmd(0x0000);

```

```

183     PIOUT &= ~BIT3;
184     __delay_cycles(100);
185     PIOUT |= BIT3;
186
187     sendDACcmd(0x701C);
188 }
189
190 // Send a command over SPI to the DAC
191 void sendDACcmd(unsigned short cmd)
192 {
193     USICTL0 &= ~USISWRST;           // USI released for operation
194     PIOUT &= ~BIT1;
195
196     while (!(USIIFG & USICTL1));    // Counter clear?
197     USISRL = cmd>>8;
198     USICNT = 8;                     // re-load counter
199     while (!(USIIFG & USICTL1));    // Counter clear?
200     USISRL = cmd;
201     USICNT = 8;                     // re-load counter
202
203     while (!(USIIFG & USICTL1));    // Counter clear?
204     USICTL0 |= USISWRST;           // hold USI
205
206     PIOUT |= BIT1;
207 }
208
209 // calculate and send the three output voltages to the DAC for the given frequency
210 void outputVoltages()
211 {
212     sendDACcmd(0x1000 + getDACVoltageCmd(interp(frequency, vamc)));
213     sendDACcmd(0x2000 + getDACVoltageCmd(interp(frequency, veld1)));
214     sendDACcmd(0x3000 + getDACVoltageCmd(interp(frequency, veld2)));
215
216     PIOUT &= ~BIT2;
217     __delay_cycles(2);
218     PIOUT |= BIT2;
219 }
220
221 // return the last 12 bits of the command necessary to change an output channel on
the DAC
222 unsigned short getDACVoltageCmd(unsigned short voltage)
223 {
224     // the parameter "voltage" has units of 10s of millivolts
225     // i.e. voltage==100 corresponds to 1 volt
226     if(voltage > 3000)
227         return 0xFFFF;
228     voltage = (voltage*11)/8 - voltage/100;
229     return voltage & 0xFFFF;
230 }
231

```

```

232 // Initialize the lookup tables for the tuning voltages
233 // Data points are available in 5 MHz increments
234 void initializeTables()
235 {
236     freq[0] = 240;
237     vamc[0] = 1140;
238     veld1[0]= 710;
239     veld2[0]= 1140;
240
241     freq[1] = 245;
242     vamc[1] = 1240;
243     veld1[1]= 720;
244     veld2[1]= 1320;
245
246     freq[2] = 250;
247     vamc[2] = 1330;
248     veld1[2]= 800;
249     veld2[2]= 1850;
250
251     freq[3] = 255;
252     vamc[3] = 1560;
253     veld1[3]= 1000;
254     veld2[3]= 2160;
255
256     freq[4] = 260;
257     vamc[4] = 1750;
258     veld1[4]= 1230;
259     veld2[4]= 2030;
260
261     freq[5] = 265;
262     vamc[5] = 2160;
263     veld1[5]= 1210;
264     veld2[5]= 2730;
265
266     freq[6] = 270;
267     vamc[6] = 2970;
268     veld1[6]= 1370;
269     veld2[6]= 2970;
270 }
271
272 // Interpolate values from the lookup tables to find tuning voltages depending on
    the current frequency
273 unsigned short interp(unsigned short f, unsigned short* table)
274 {
275     unsigned char i;
276     i = (f-240)/5;
277     if(i>=6)
278         return table[6];
279     else
280     {

```

```
281     if(table[i+1] > table[i])
282         return (f-freq[i]) * (table[i+1]-table[i])/5 + table[i]; // freq[i+1]-freq[
283             i] will always equal 5
284     else
285         return (f-freq[i]) * (table[i]-table[i+1])/5 + table[i]; // freq[i+1]-freq[
286             i] will always equal 5
    }
}
```

---

### 5.3 Testing on a Combatant Craft Assault

The Combatant Craft Assault (CCA) is a military boat intended for “medium range maritime interdiction of SOF in [a] medium/high threat environment” and it “supports coastal patrol and insertion extraction operations.” The CCA uses UHF satcom with an antenna placed in the bow of the craft. Replacing the conventional antenna in a CCA with the metamaterial antenna prototype led to slightly worse performance than was shown in the previous section, but still in the vicinity of the original antenna. This may have resulted from placing the metamaterial antenna slightly deeper in the metal cavity supporting it. Bear in mind that even though the metamaterial antenna is less than one third the thickness of the other antenna, its gain is within 2dB of the original antenna. Fig. 5.6 shows photographs of a CCA, the metamaterial antenna mounted on the CCA, and a comparison of the received power levels between the metamaterial antenna and a conventional alternative.



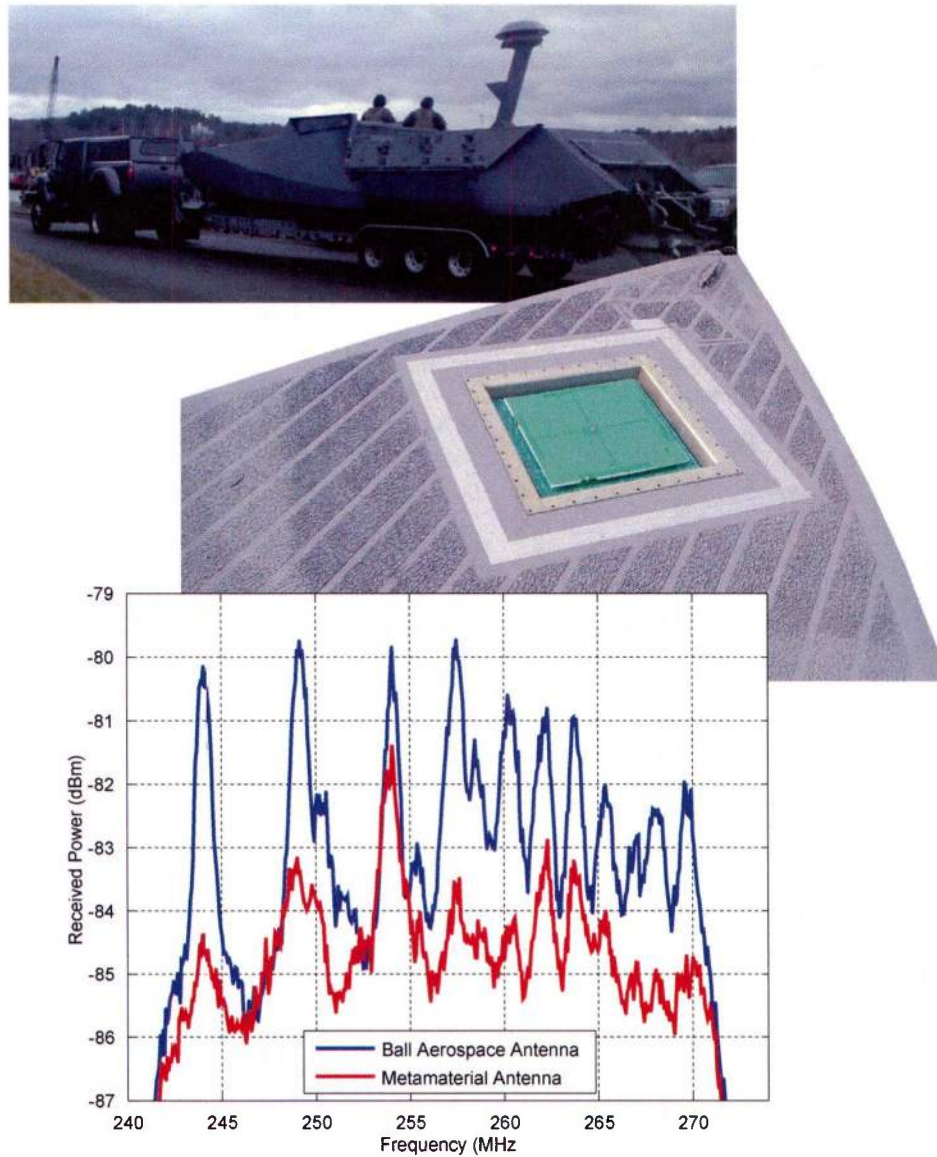


Fig. 5.6: Photographs of a CCA (top), the metamaterial antenna mounted on the CCA (middle) and a comparison of the received power levels between the metamaterial antenna and a conventional antenna (bottom).

## Conclusions and Future Work

### 6.1 Conclusions

We have shown that inhomogeneous metasurfaces play an important role in improving the characteristics of horn feeds for reflector antennas. Specifically, we have developed metasurface designs consisting of metallic patches and connecting wires, which provide the surface impedances that are necessary to support hybrid modes in circular waveguides, and thus enhance conical horn antennas over a broad bandwidth. Horns based on properly designed inhomogeneous metasurfaces can match the performance of traditional corrugated horns while requiring a fraction of the weight (mass) and improving the bandwidth.

Tunable crossed end-loaded dipole (ELD) antennas support near-arbitrary beam polarizations with dynamic reconfigurability, but without the need for complex and expensive feed networks. For relatively low-power applications, all that is required is standard printed-circuit-board manufacturing techniques combined with inexpensive components, including varactor diodes. A prototype antenna showed excellent performance with tunability across an approximately 20% bandwidth.

A lightweight tunable artificial magnetic conductor (AMC) was created from miniaturized interconnected unit cells connected by wire vias to a ground plane beneath. Tunable capacitors between unit cells provides tuning of the AMC over one to two octaves of bandwidth, depending on the AMC thickness. Absorption in the AMC remains better than -10 dB across its entire tunable range for thicknesses of 2.54 cm or greater. Combining the tunable crossed ELDs with the tunable AMC

substrate results in a compact, low-profile antenna with near-arbitrary, dynamic control of polarization and operating frequency, with a tunable range exceeding 35%. Potential applications include vehicular and airborne platforms requiring low-profile antennas for satellite connectivity. The prototype antenna was tested in comparison to conventional alternatives, showing comparable performance while requiring a fraction of the thickness.

## 6.2 Future Work

Although this work has resulted in numerous promising antenna characteristics, several important aspects of the design need to be further explored and developed before the antennas could be used in many real-world applications. Extensions to this research could include the following.

### 6.2.1 Inhomogeneous Liners for Horn Antennas

The primary limitation of the inhomogeneous liner designs for conical horn antennas is manufacturability. Liners for rectangular horns can be manufactured easily using printed circuit board techniques, but the inhomogeneous metamaterial liner design presented here would require a complex combination of multiple layers of flexible circuits connected by vias and conformable to the interior of a cone, or some analogous structure that is not necessarily straightforward to build. Future work could investigate and attempt to overcome these issues.

### 6.2.2 Compact Tunable Metamaterial Antenna

#### 6.2.2.1 Power Handling

The metamaterial antenna prototype was limited to 0.25 W in its power handling by the RF transformer. A different balun design could increase the power handling to the order of watts or possibly the low tens of watts before the voltages induced on the varactor diodes in the ELDs would begin to create undesired intermodulation products, distorting the transmitted signal. The varactor diodes on the AMC should be able to handle more power than those on the ELDs, but a thorough

investigation of their power handling should be completed before exposing them to power levels beyond the low tens of watts. It may be possible to combine the AMC with crossed fat dipoles and still cover the UHF satcom band, while eliminating the power complexities of the tunable ELDs.

#### **6.2.2.2 Tuning Improvements**

The straightforward method for tuning would be to develop an automated system that could measure the transmitted or received power to or from another antenna with the desired polarization while adjusting the tuning voltages to maximize the gain. In a commercial production environment, this system would need to determine the optimal tuning values for each antenna produced, and then store them in a lookup table in that antenna's controlling circuitry. Alternatively, further work could be done to create adaptive algorithms to optimize the tuning voltages based on readily available parameters in the communication system, such as VSWR or signal-to-noise ratio.

#### **6.2.2.3 Structural/Mechanical Evaluations**

The metamaterial antenna prototype is fairly rigid, but an analysis should be made of its ability to withstand vibrations, shocks, and thermal stresses. Solder joints, particularly on the vias, and their surrounding traces could probably be designed to make the antenna more robust. Lastly, it may be possible to surround the antenna with structural foam for reinforcement while maintaining its electrical properties.

#### **6.2.2.4 Redesign for Additional Considerations**

Many antennas, particularly those intended for military applications, involve requirements beyond size, weight, and radiation properties. Investigations of the loading effects of frequency selective surface superstrates/radomes, or perhaps optimizing the AMC itself for specific reflection properties at desired frequencies, could prove helpful in many practical applications.

## Appendix **A**

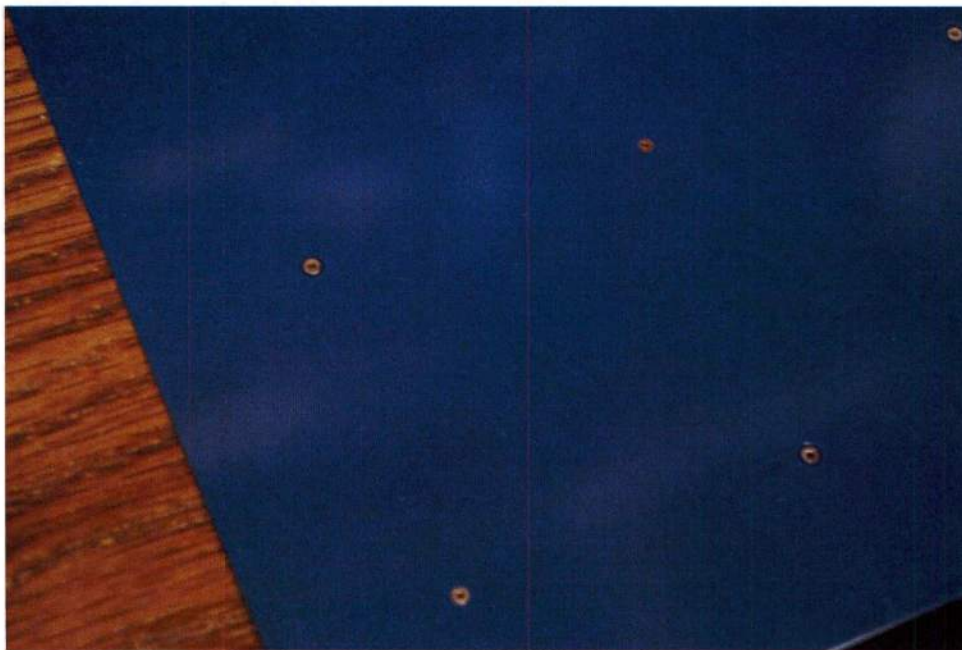
# AMC Metamaterial Prototype Fabrication

The AMC started out as four circuit boards: two 12 in. by 24 in. ground/bias plane boards and two 12 in. by 24 in. boards with the interconnected unit cell pattern. The ground/bias boards as well as the ELD boards were obtained from Epec Engineered Technologies. The patterned boards, including the varactor diodes soldered in place, were obtained from Niche Electronics Technologies, Inc.



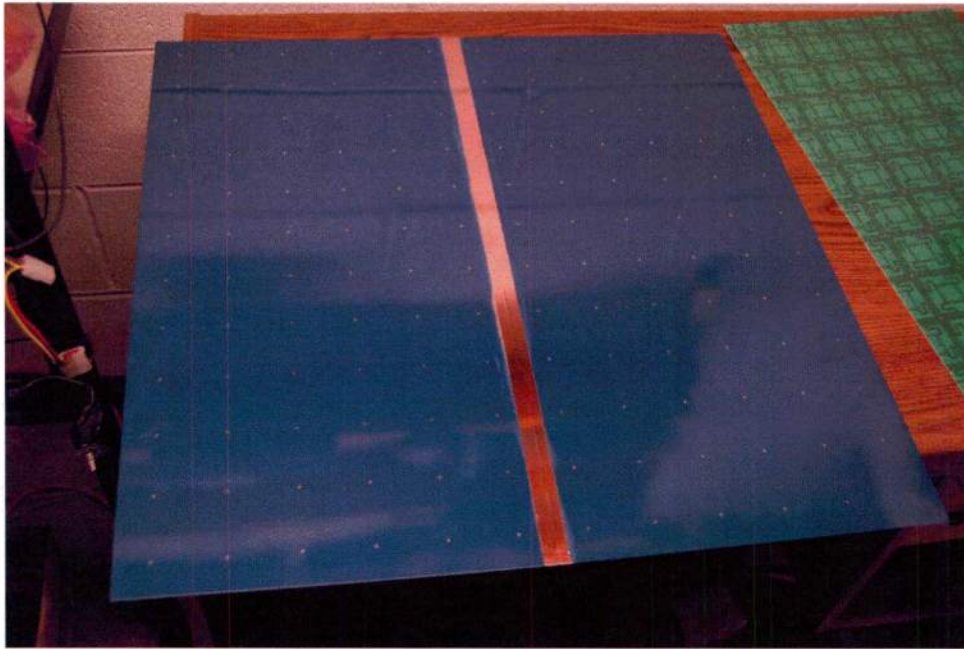


This close-up view shows that alternating holes are connected to alternating sides of the circuit board.

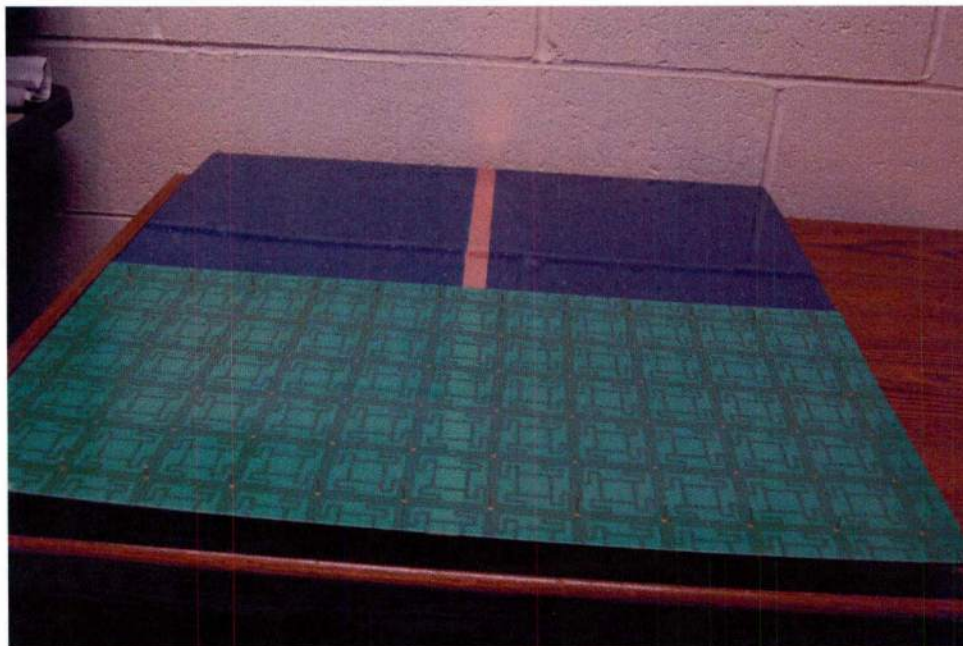




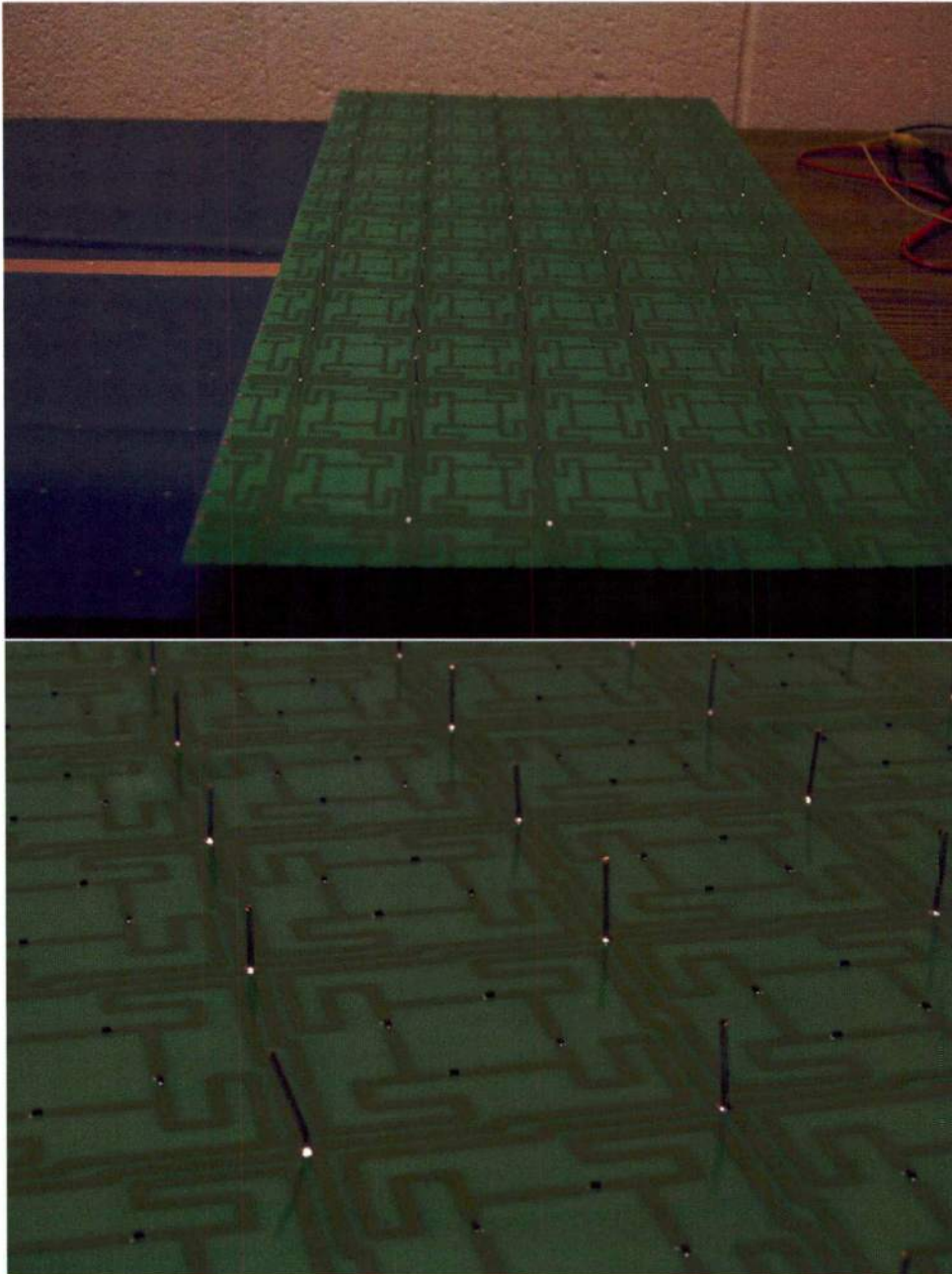
A slight oversight was that the boards were ordered with soldermask covering the copper all the way to the edges. The soldermask had to be sanded off in order to join the two halves with copper tape.



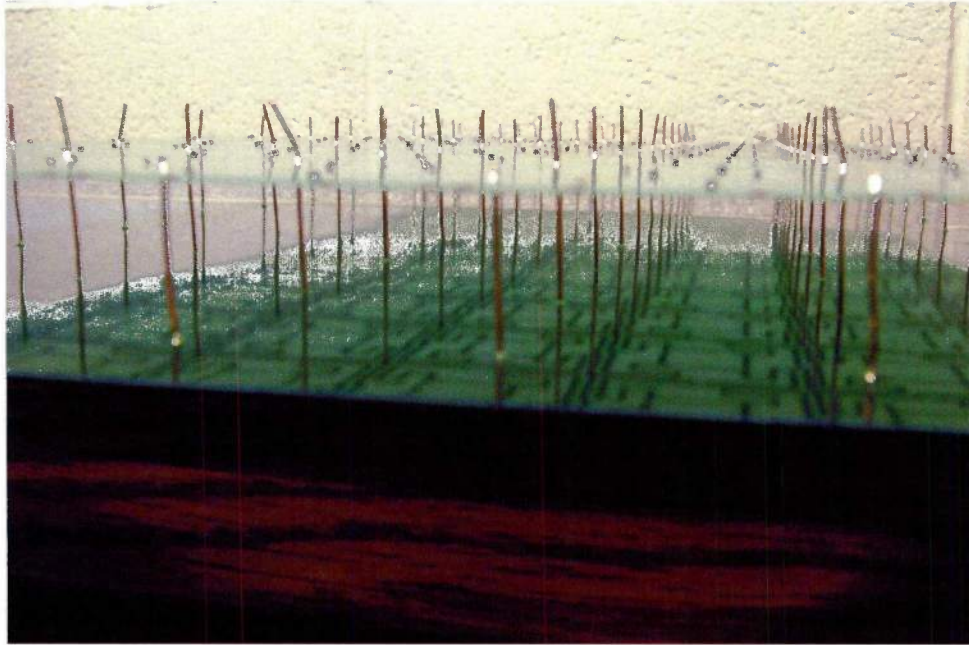
The AWG18 copper wire vias were soldered to the ground/bias planes and to the first patterned board above.



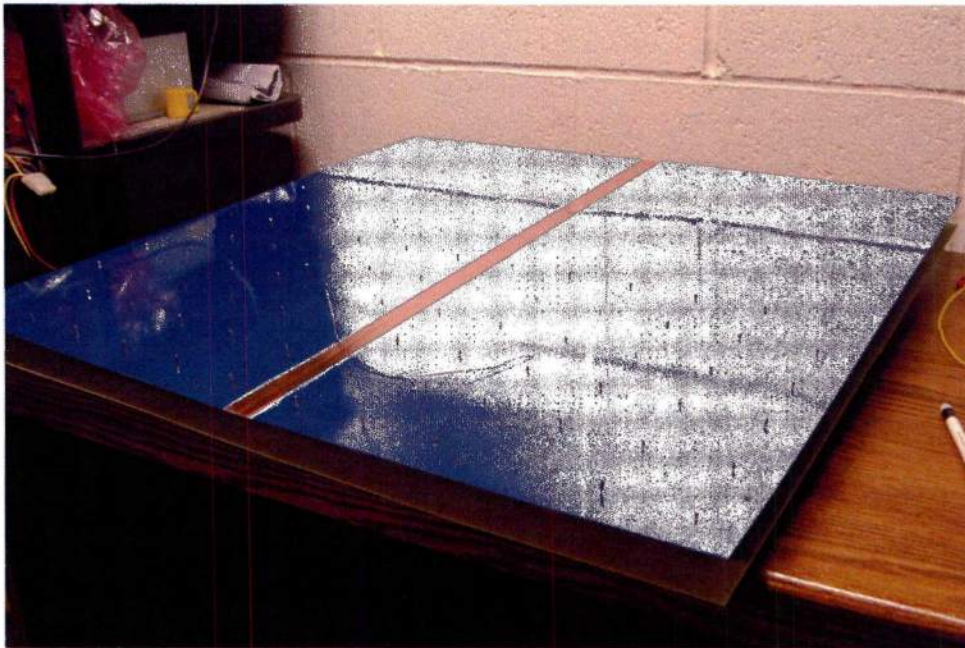
The copper wires were left long and the extra was cut off later.



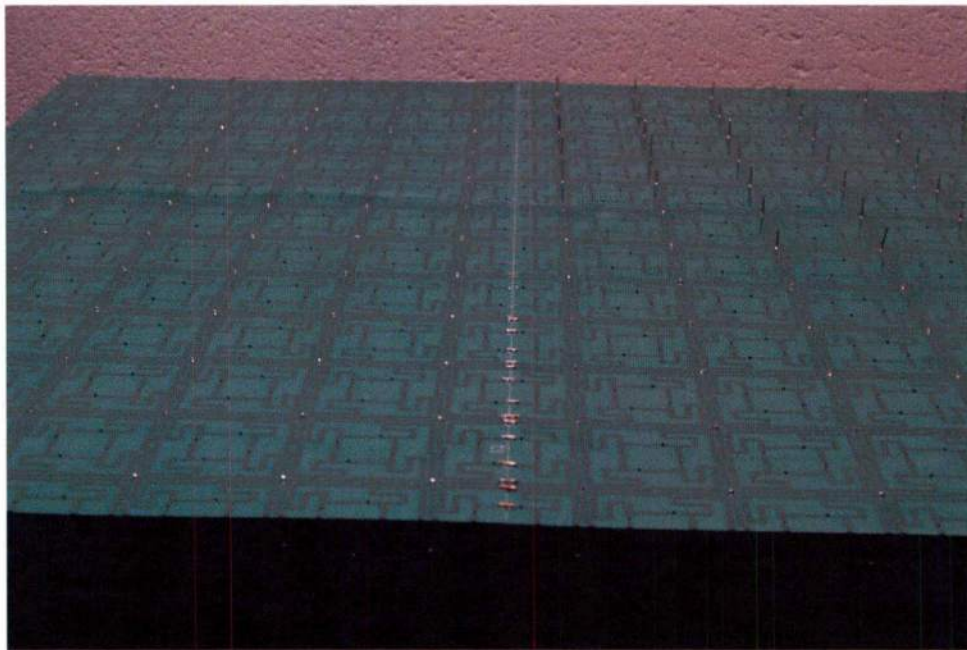




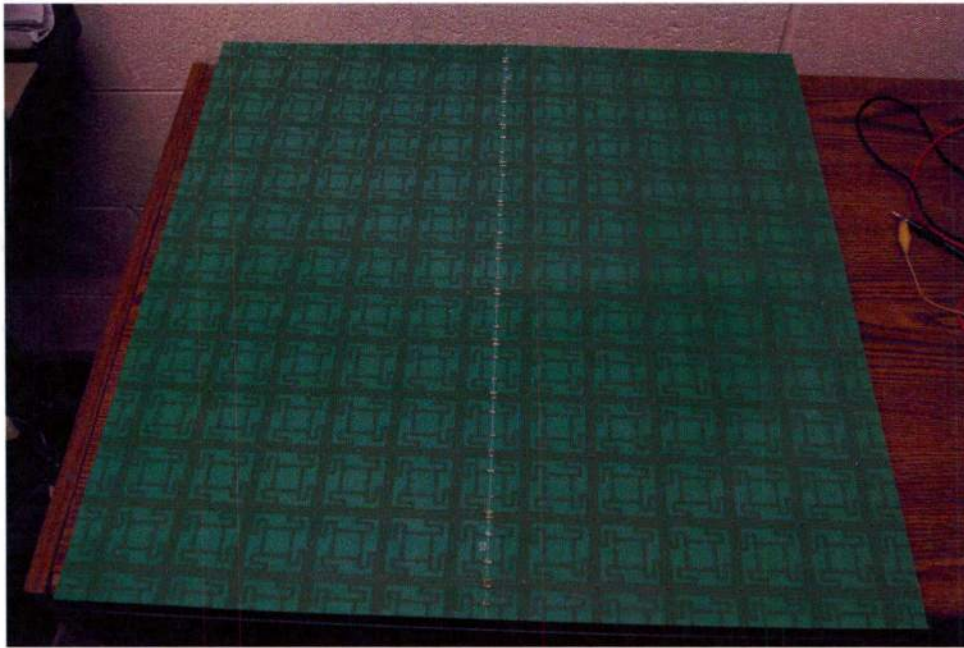
Soldering the wires to the ground plane.



Cutting off excess wire and joining the two patterned boards with small wires.

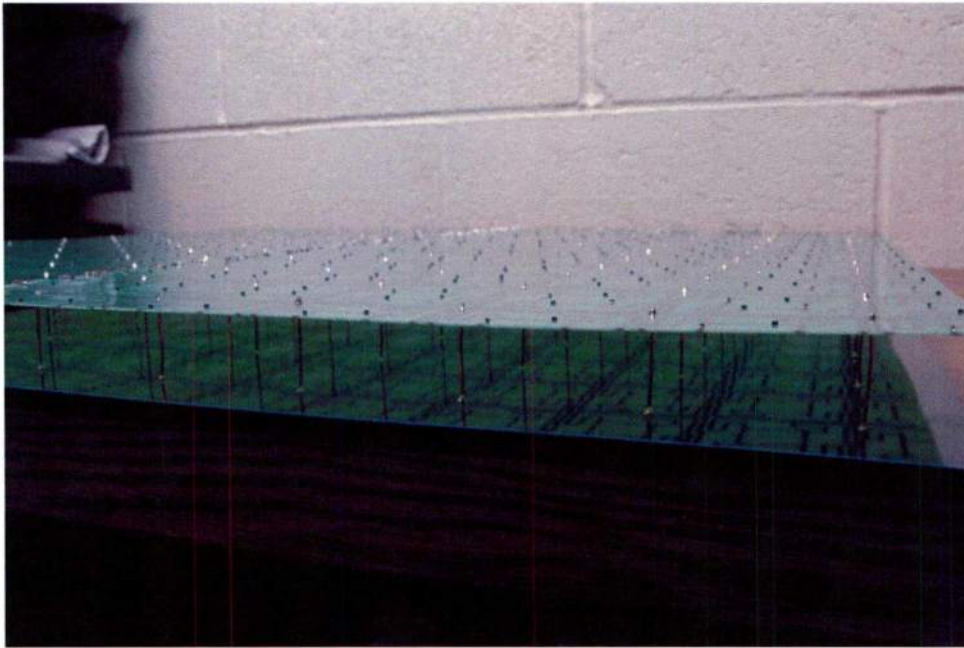


The completed AMC structure.

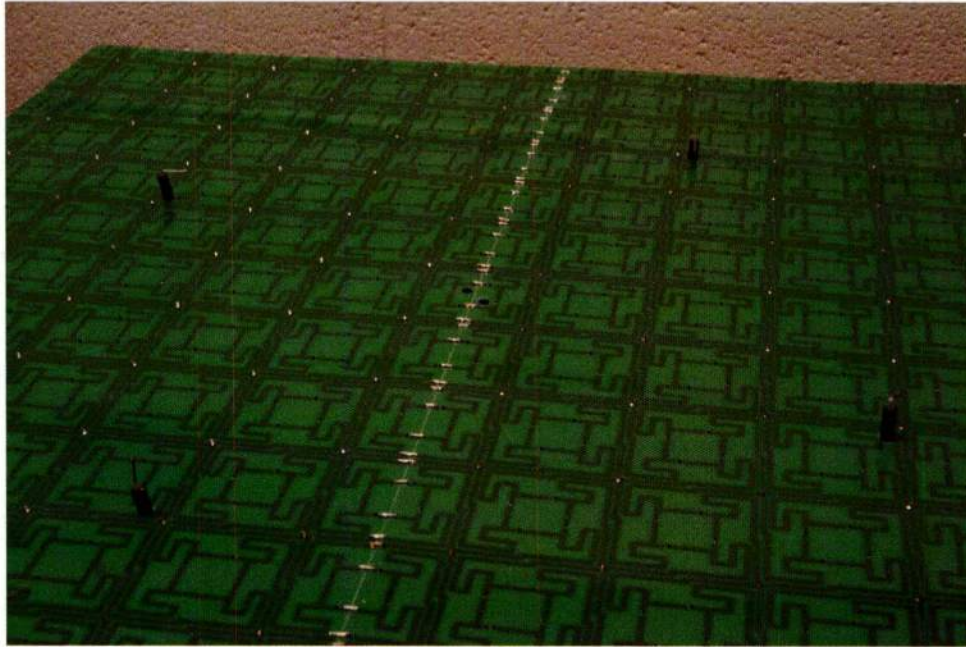




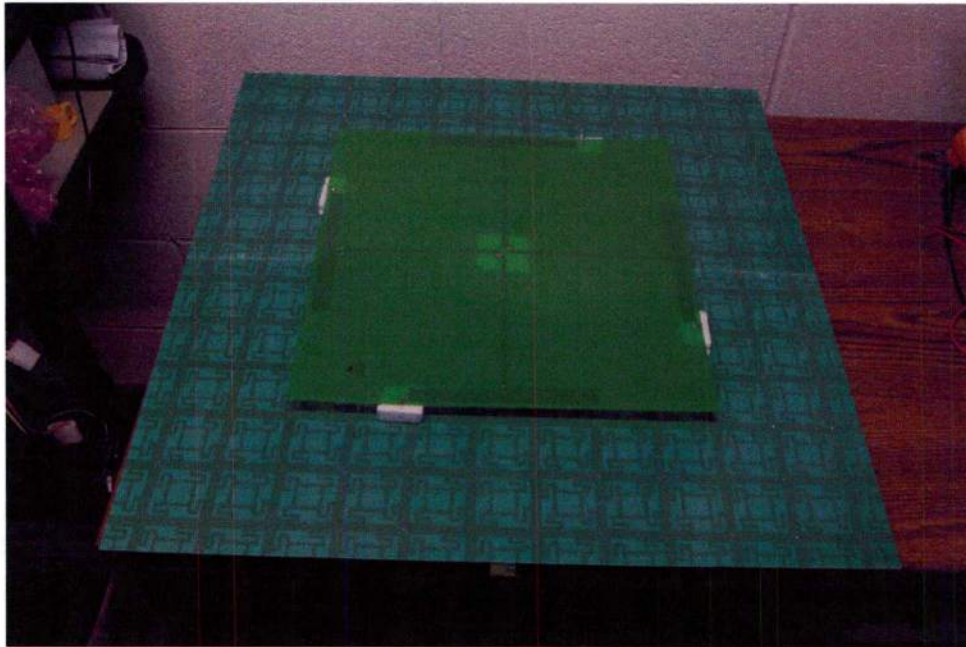
Side view of the completed AMC structure.



Coaxial cables for biasing the ELDs have been added to the AMC.



The completed initial prototype.



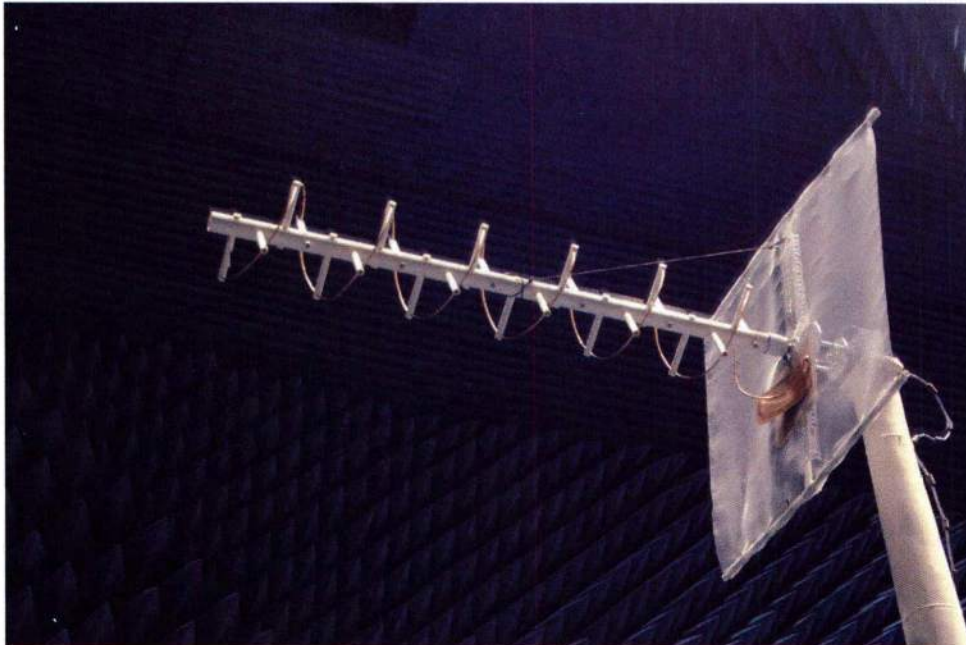
## Appendix B

### Crossed ELD Antenna Characterization

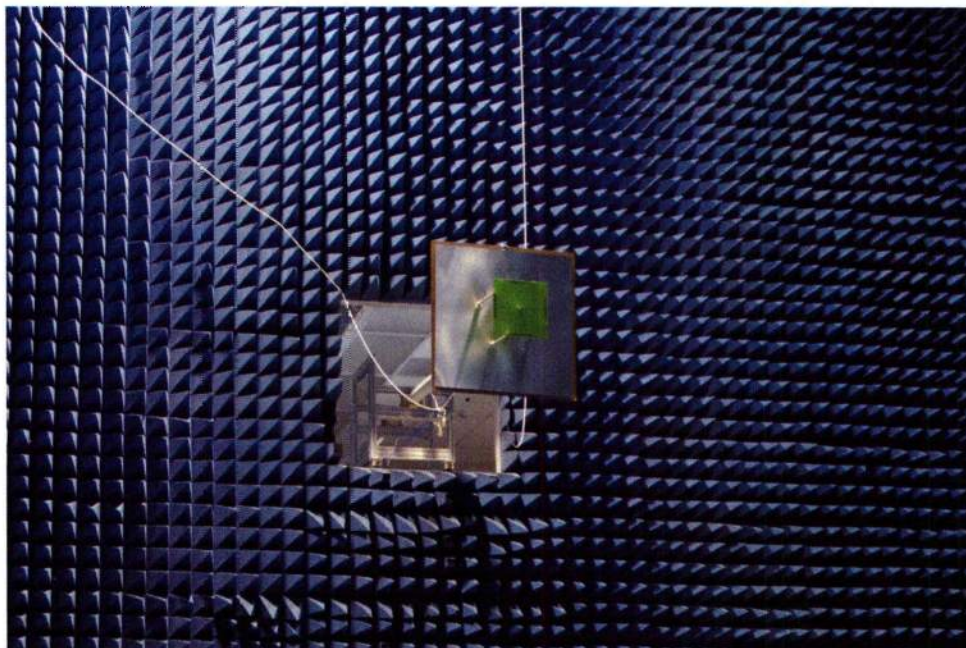
In order to assist with finding the tuning voltages for the crossed ELD antenna and the metamaterial antenna, a helical antenna was designed and constructed. The helical antenna provided circular polarization over nearly the entire range from 200 MHz to 300 MHz.

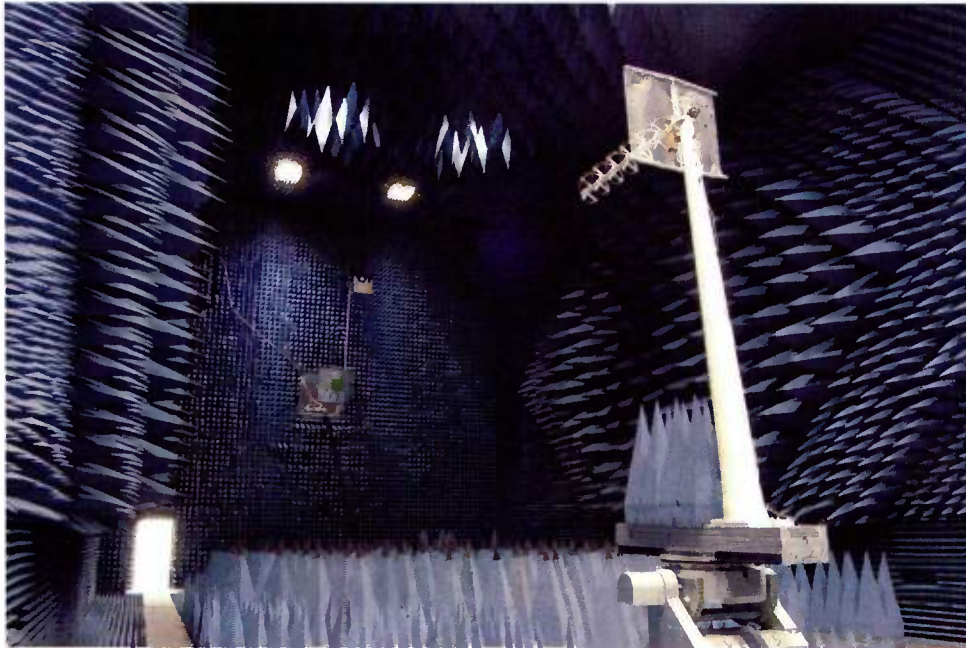






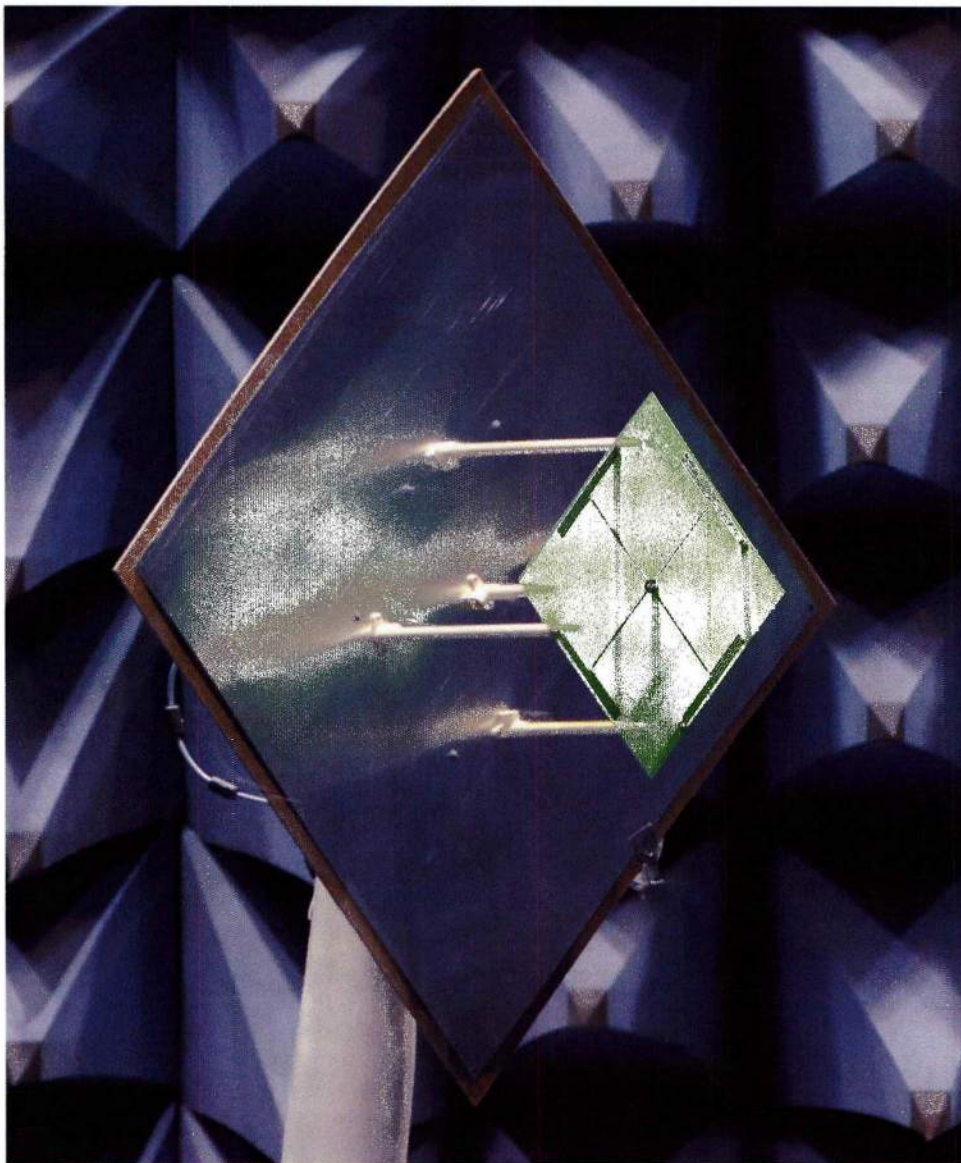
The crossed ELD antenna was mounted opposite the helical antenna to determine its appropriate tuning voltages.



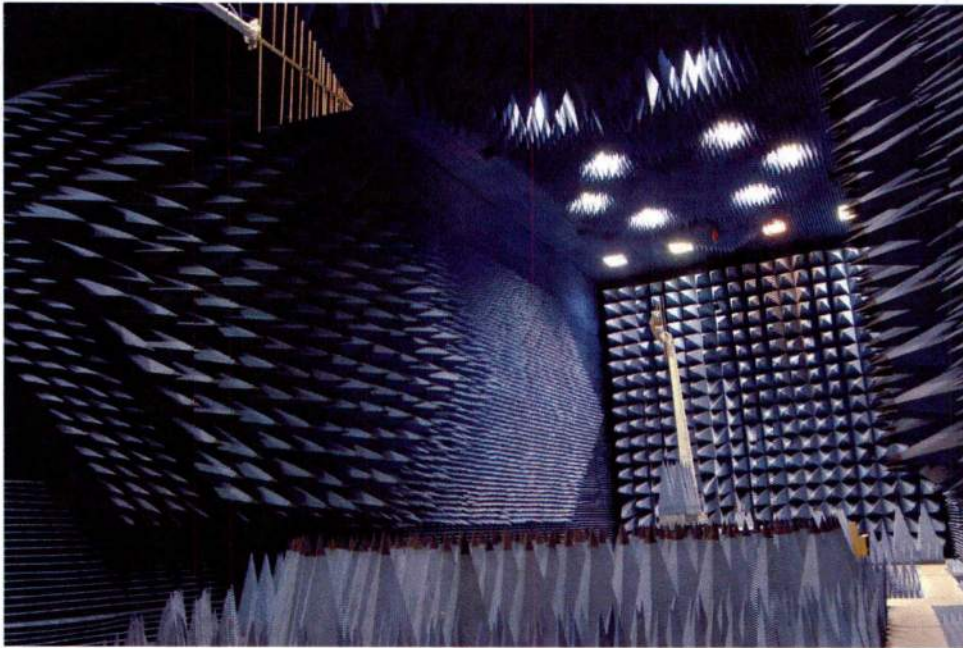




The crossed ELD antenna mounted on the model tower for characterization.



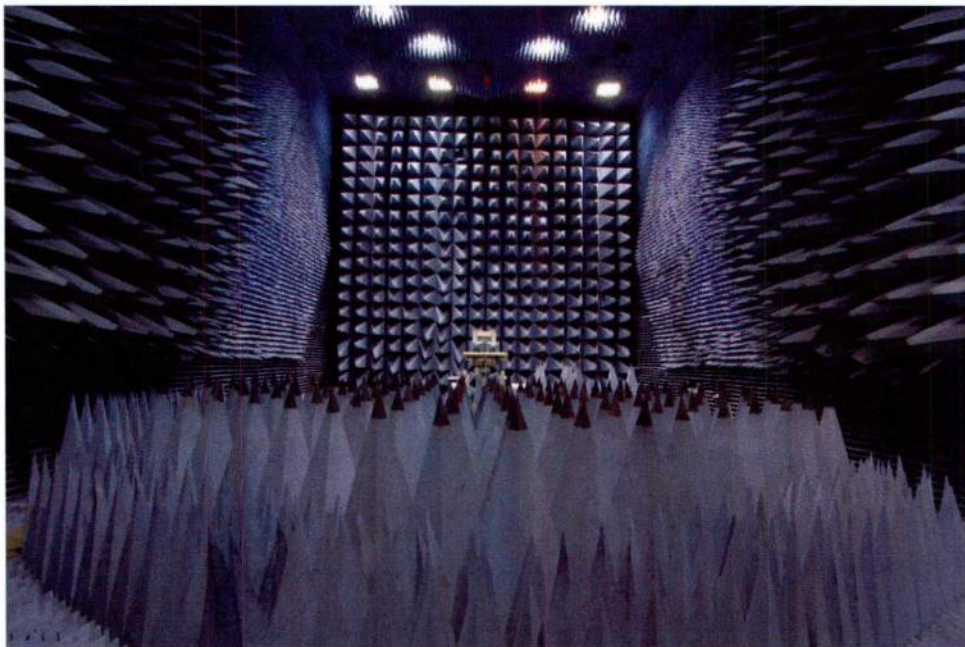
Calibration antennas mounted for a calibration with vertical polarization.



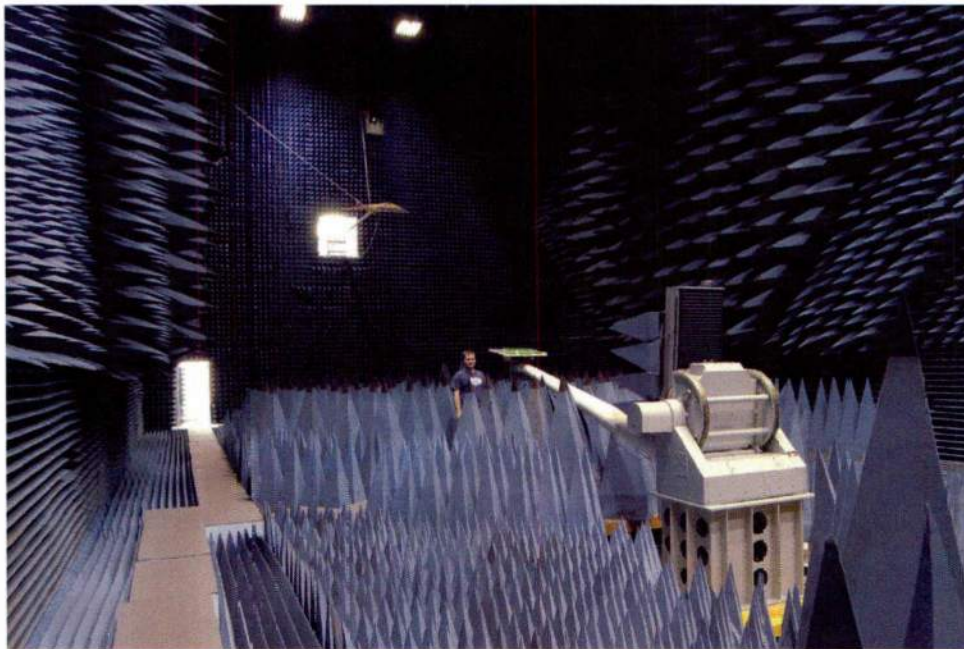
# Appendix C

## Metamaterial Antenna Characterization

A view of the antenna chamber, which is 100 ft. long, 40 ft. wide, and 40 ft. tall, and rated for frequencies down to 100 MHz. The tallest RF absorbing cones are 72 in. tall.

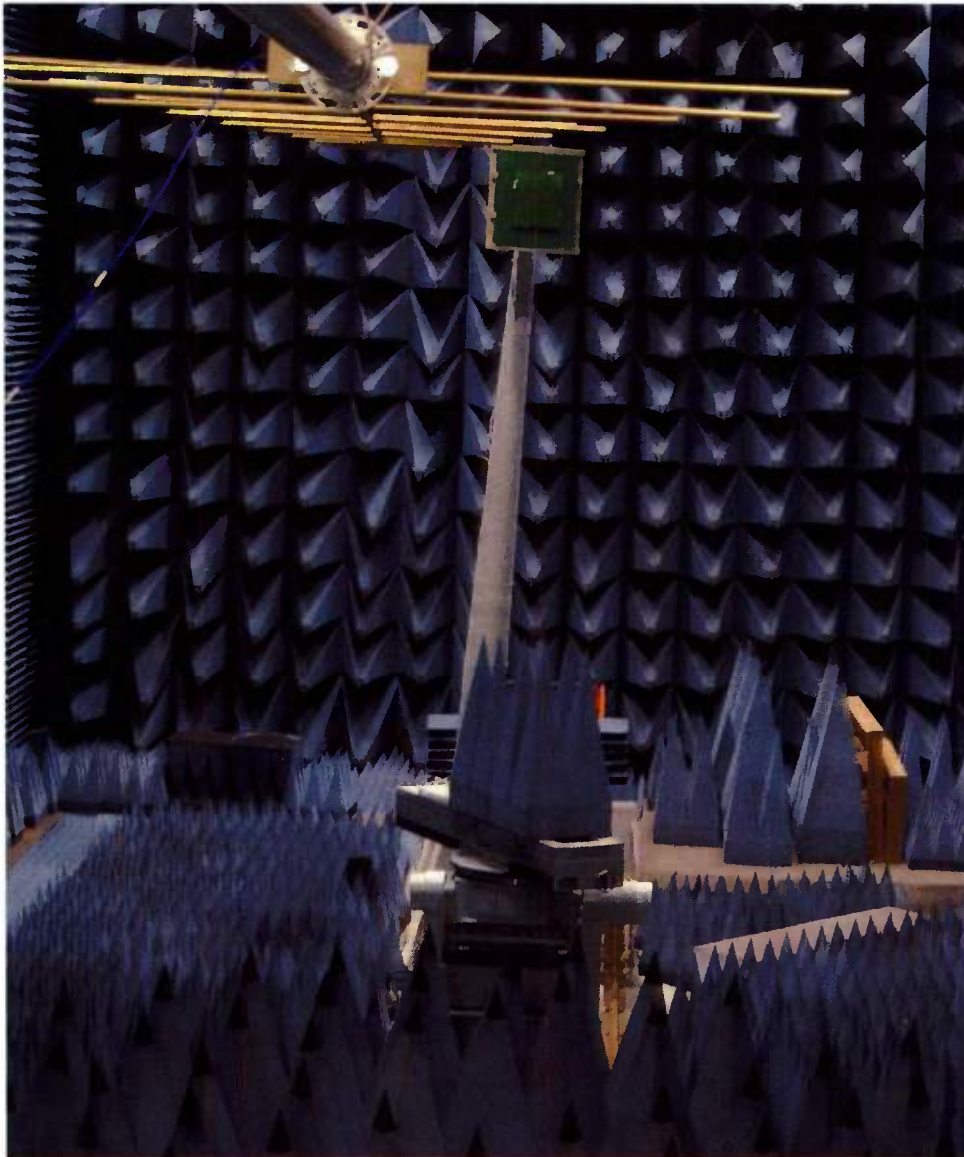


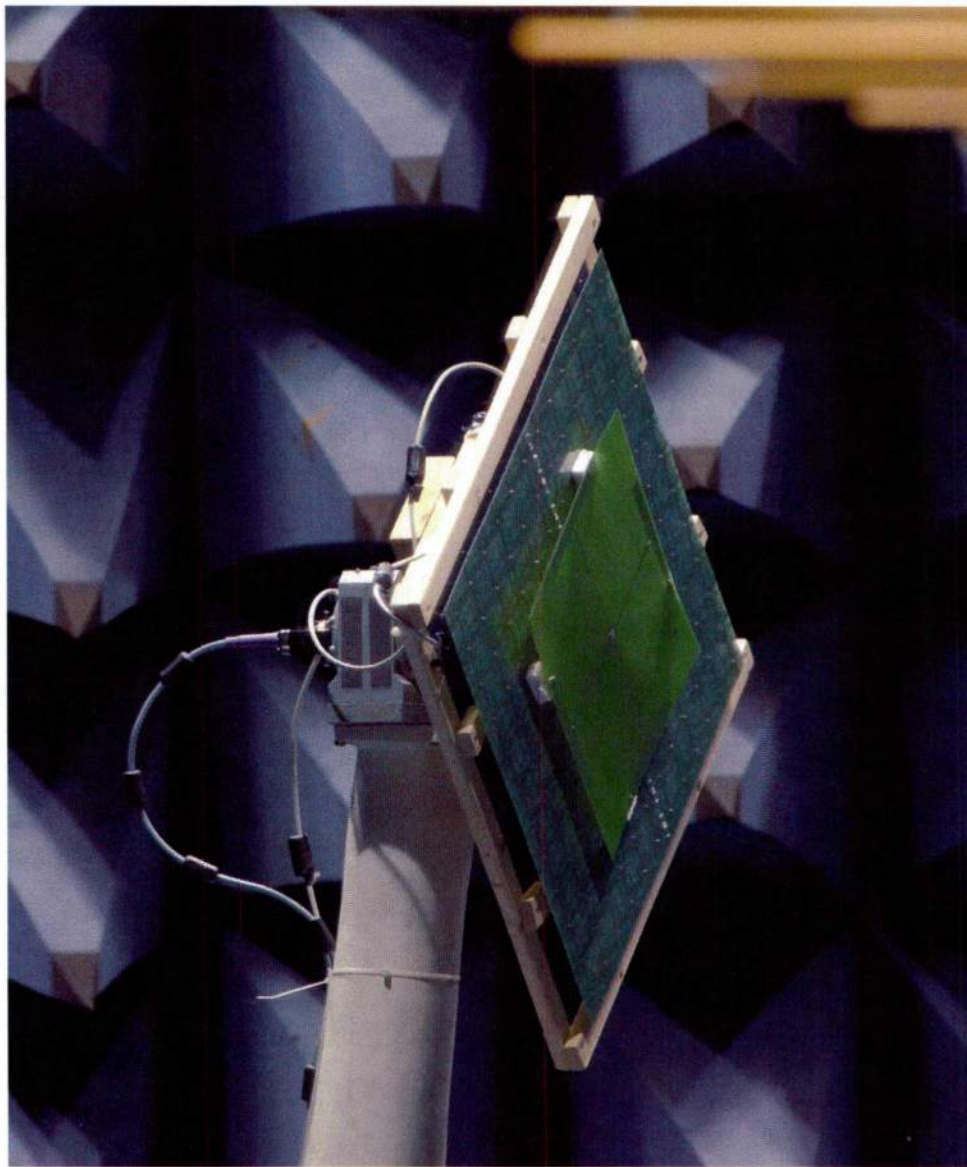
The author after mounting the metamaterial antenna on the model tower





Views of the chamber from the control room, including a view of the log-periodic standard antenna used as the transmitter for radiation pattern measurements.



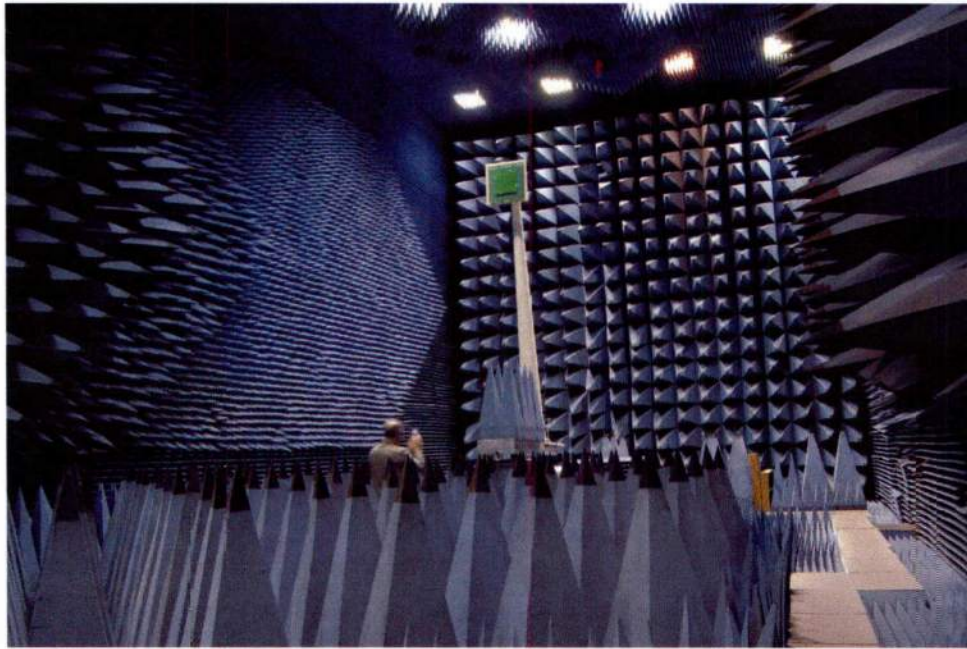


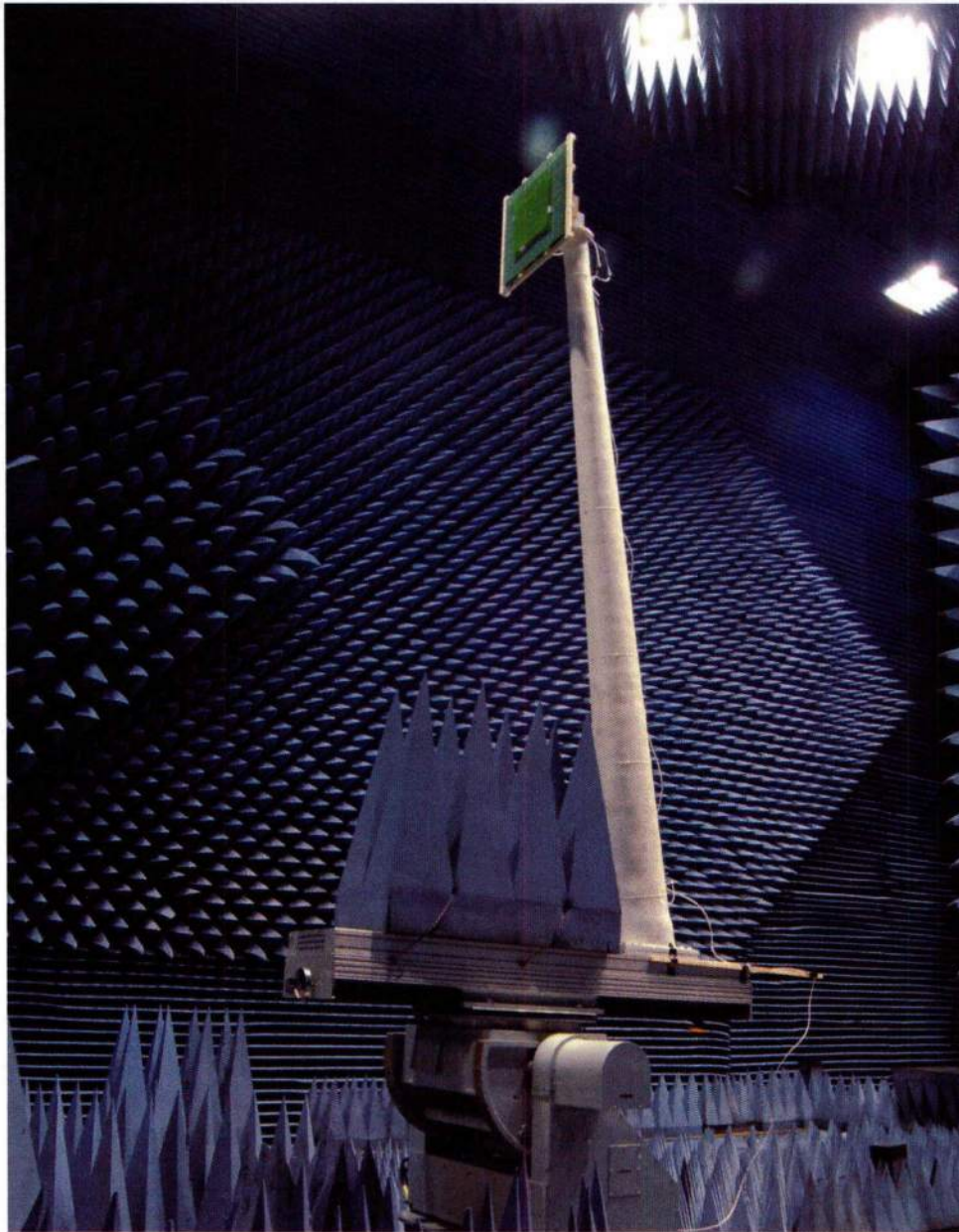


The author in the control room of the antenna chamber.

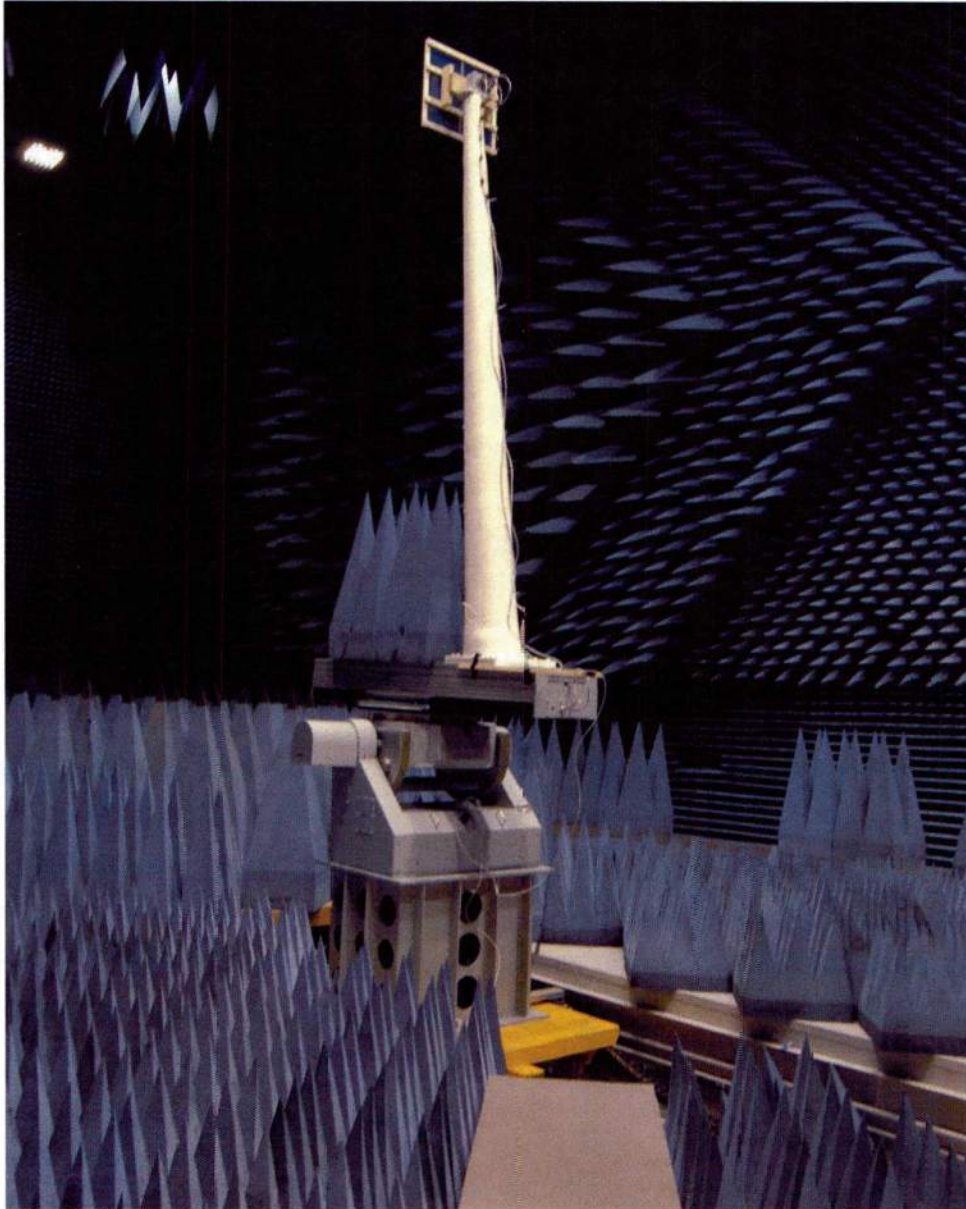


The metamaterial antenna mounted on the model tower for measurements.

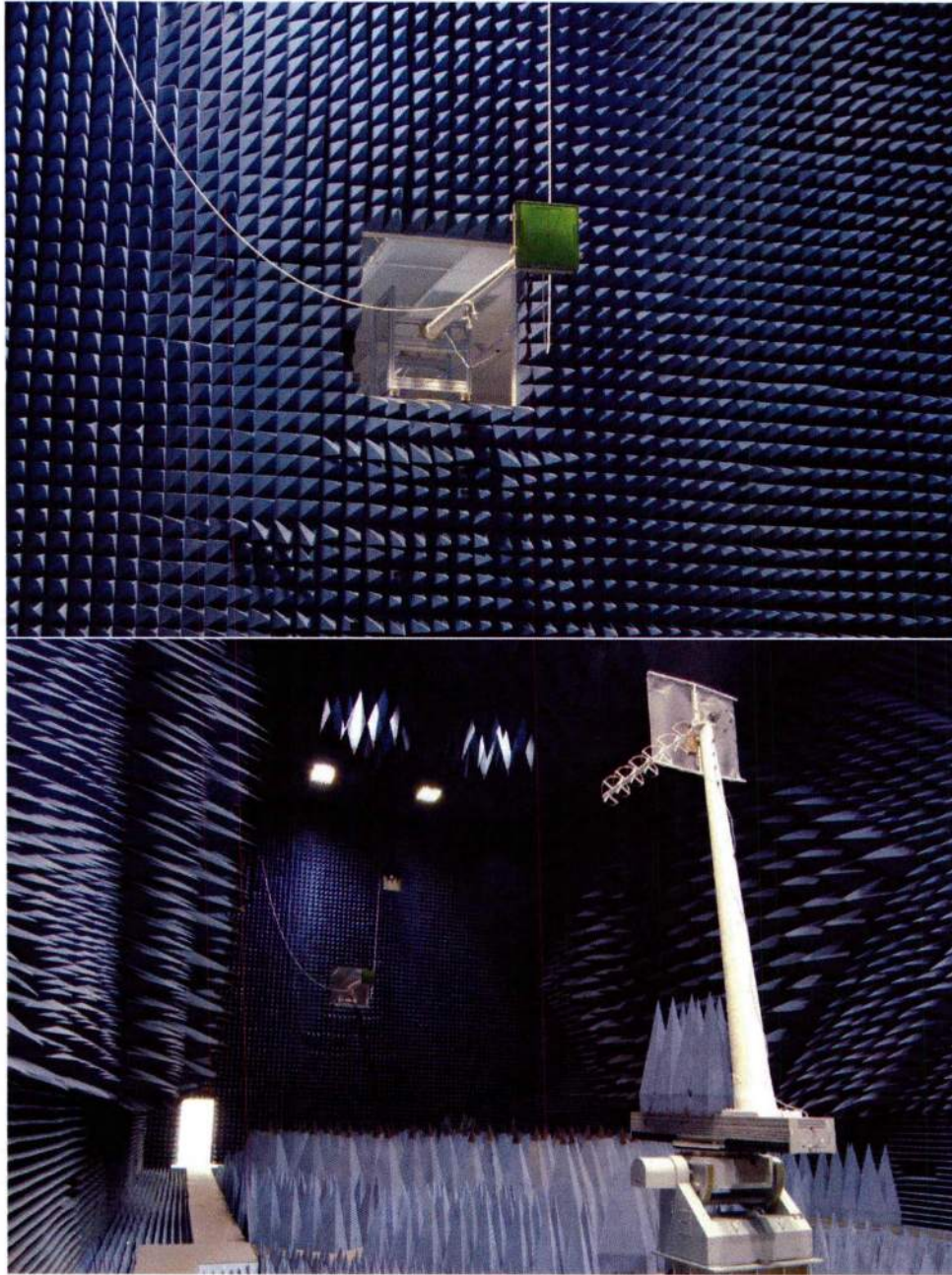






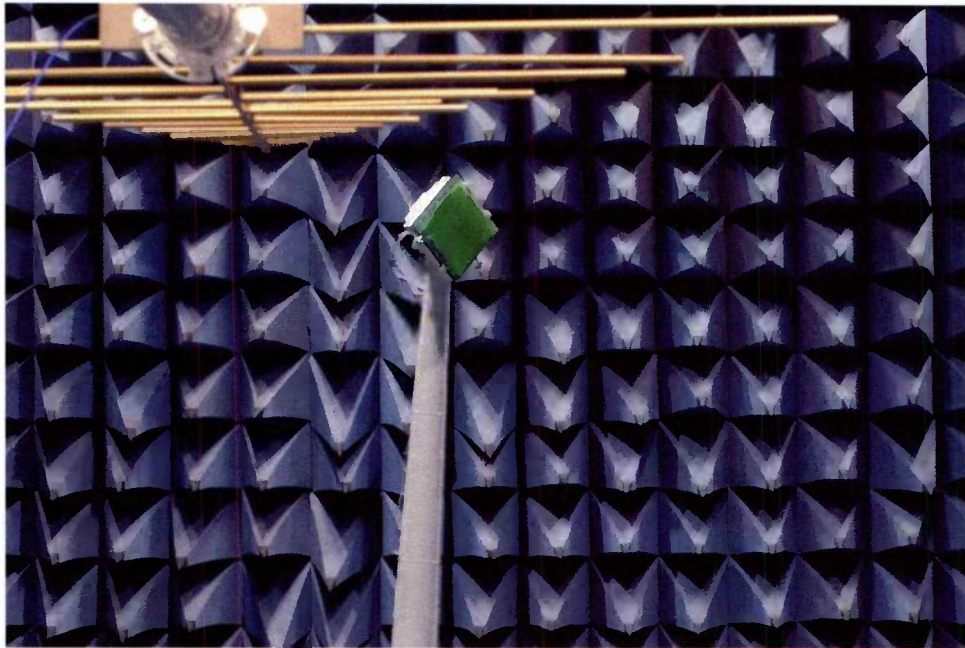


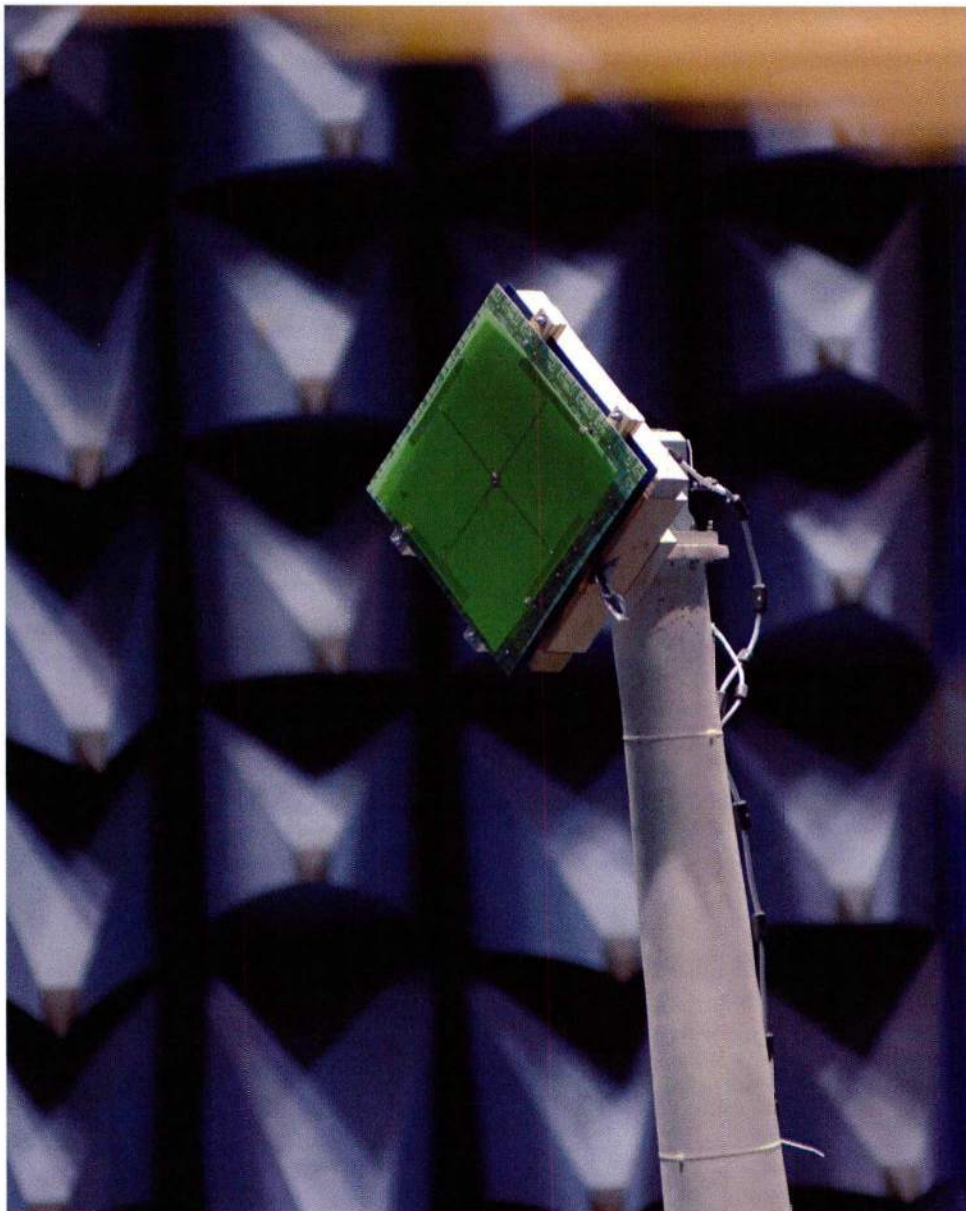
The second iteration of the metamaterial antenna in the process of finding its tuning voltages with the help of the helical antenna.

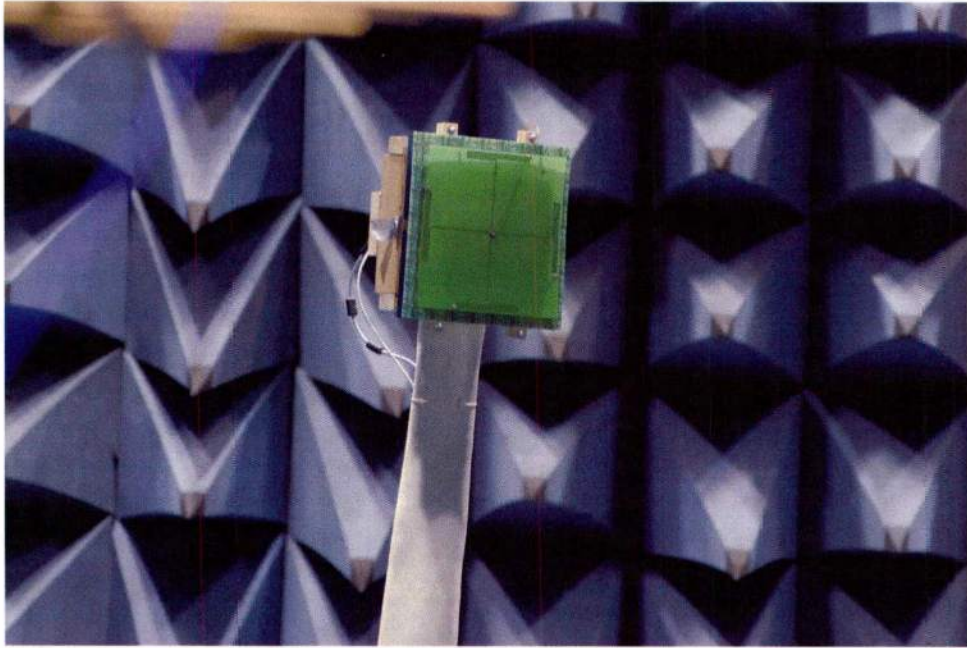




The second iteration of the metamaterial antenna in the midst of pattern characterization on the model tower.







## References

- [1] W. E. Kock, "Metal-lens antennas," *Proceedings of the IRE*, vol. 34, no. 11, pp. 828–836, Nov. 1946.
- [2] —, "Metallic delay lenses," *Bell System Technical Journal*, vol. 27, no. 1, pp. 58–82, Jan. 1948.
- [3] A. J. Simmons and A. F. Kay, "The scalar feed—a high performance feed for large paraboloid reflectors," *Design and Construction of Large Steerable Aerials*, pp. 213–217, 1966.
- [4] H. Minnett and B. Thomas, "A method of synthesizing radiation patterns with axial symmetry," *Antennas and Propagation, IEEE Transactions on*, vol. 14, no. 5, pp. 654–656, 1966.
- [5] V. Rumsey, "Horn antennas with uniform power patterns around their axes," *IEEE Transactions on Antennas and Propagation*, vol. 14, no. 5, pp. 656–658, Sep. 1966.
- [6] V. G. Veselago, "Electrodynamics of materials with simultaneously negative values of epsilon and mu," *Sov. Phys. Usp*, 1968.
- [7] F. Yang and Y. Rahmat-Samii, *Electromagnetic band gap structures in antenna engineering*. Cambridge University Press Cambridge, 2009.
- [8] B. A. Munk, *Frequency selective surfaces: theory and design*. Wiley-Interscience, 2005.
- [9] J. B. Pendry, "Negative refraction makes a perfect lens," *Phys. Rev. Lett.*, vol. 85, no. 18, pp. 3966–3969, Oct. 2000.
- [10] J. B. Pendry, D. Schurig, and D. R. Smith, "Controlling electromagnetic fields," *Science*, vol. 312, no. 5781, pp. 1780–1782, Jun. 2006.
- [11] D. Schurig, J. J. Mock, B. J. Justice, S. A. Cummer, J. B. Pendry, A. F. Starr, and D. R. Smith, "Metamaterial electromagnetic cloak at microwave frequencies," *Science*, vol. 314, no. 5801, pp. 977–980, Nov. 2006.

- [12] E. Lier, D. H. Werner, C. P. Scarborough, Q. Wu, and J. A. Bossard, "An octave-bandwidth negligible-loss radiofrequency metamaterial," *Nature Materials*, vol. 10, no. 3, pp. 216–222, Jan. 2011.
- [13] D. Sievenpiper, L. Zhang, R. F. J. Broas, N. G. Alexopolous, and E. Yablonovitch, "High-impedance electromagnetic surfaces with a forbidden frequency band," *IEEE Transactions on Microwave Theory and Techniques*, vol. 47, no. 11, pp. 2059–2074, Nov. 1999.
- [14] F.-R. Yang, K.-P. Ma, Y. Qian, and T. Itoh, "A uniplanar compact photonic-bandgap (UC-PBG) structure and its applications for microwave circuits," *IEEE Transactions on Microwave Theory and Techniques*, vol. 47, no. 8, pp. 1509–1514, Aug. 1999.
- [15] C. L. Holloway, A. Dienstfrey, E. F. Kuester, J. F. O'Hara, A. K. Azad, and A. J. Taylor, "A discussion on the interpretation and characterization of metafilms/metasurfaces: the two-dimensional equivalent of metamaterials," *Metamaterials*, vol. 3, no. 2, pp. 100–112, Oct. 2009.
- [16] C. R. Simovski, "Material parameters of metamaterials (a review)," *Opt. Spectrosc.*, vol. 107, no. 5, pp. 726–753, Nov. 2009.
- [17] F. Capolino, *Metamaterials Handbook: Theory and phenomena of metamaterials*. CRC PressI Llc, 2009, vol. 1.
- [18] G. Goussetis, A. P. Feresidis, and J. C. Vardaxoglou, "Tailoring the AMC and EBG characteristics of periodic metallic arrays printed on grounded dielectric substrate," *IEEE Transactions on Antennas and Propagation*, vol. 54, no. 1, pp. 82–89, Jan. 2006.
- [19] D. F. Sievenpiper, J. H. Schaffner, H. J. Song, R. Y. Loo, and G. Tandonan, "Two-dimensional beam steering using an electrically tunable impedance surface," *IEEE Transactions on Antennas and Propagation*, vol. 51, no. 10, pp. 2713–2722, Oct. 2003.
- [20] F. Yang and Y. Rahmat-Samii, "Reflection phase characterizations of the EBG ground plane for low profile wire antenna applications," *IEEE Transactions on Antennas and Propagation*, vol. 51, no. 10, pp. 2691–2703, 2003.
- [21] D. Jackson and A. Oliner, "A leaky-wave analysis of the high-gain printed antenna configuration," *IEEE Transactions on Antennas and Propagation*, vol. 36, no. 7, pp. 905–910, 1988.
- [22] A. Feresidis, G. Goussetis, S. Wang, and J. Vardaxoglou, "Artificial magnetic conductor surfaces and their application to low-profile high-gain planar antennas," *IEEE Transactions on Antennas and Propagation*, vol. 53, no. 1, pp. 209–215, 2005.



- [23] Y. Ge, K. Esselle, and T. Bird, "The use of simple thin partially reflective surfaces with positive reflection phase gradients to design wideband, low-profile EBG resonator antennas," *IEEE Transactions on Antennas and Propagation*, vol. 60, no. 2, pp. 743–750, 2012.
- [24] F.-R. Yang, K.-P. Ma, Y. Qian, and T. Itoh, "A novel TEM waveguide using uniplanar compact photonic-bandgap (UC-PBG) structure," *IEEE Transactions on Microwave Theory and Techniques*, vol. 47, no. 11, pp. 2092–2098, Nov. 1999.
- [25] F. Yang and Y. Rahmat-Samii, "Microstrip antennas integrated with electromagnetic band-gap (EBG) structures: a low mutual coupling design for array applications," *IEEE Transactions on Antennas and Propagation*, vol. 51, no. 10, pp. 2936–2946, Oct. 2003.
- [26] D. J. Kern, D. H. Werner, A. Monorchio, L. Lanuzza, and M. J. Wilhelm, "The design synthesis of multiband artificial magnetic conductors using high impedance frequency selective surfaces," *IEEE Transactions on Antennas and Propagation*, vol. 53, no. 1, pp. 8–17, Jan. 2005.
- [27] D. J. Kern and D. H. Werner, "A genetic algorithm approach to the design of ultra-thin electromagnetic bandgap absorbers," *Microwave and Optical Technology Letters*, vol. 38, no. 1, pp. 61–64, 2003.
- [28] X. Liu, T. Starr, A. F. Starr, and W. J. Padilla, "Infrared spatial and frequency selective metamaterial with near-unity absorbance," *Phys. Rev. Lett.*, vol. 104, no. 20, p. 207 403, May 2010.
- [29] Z. H. Jiang, S. Yun, F. Toor, D. H. Werner, and T. S. Mayer, "Conformal dual-band near-perfectly absorbing mid-infrared metamaterial coating," *ACS Nano*, vol. 5, no. 6, pp. 4641–4647, Jun. 2011.
- [30] D. Kern, D. Werner, and M. Lisovich, "Metaferrites: using electromagnetic bandgap structures to synthesize metamaterial ferrites," *IEEE Transactions on Antennas and Propagation*, vol. 53, no. 4, pp. 1382–1389, 2005.
- [31] Z. Bayraktar, M. Gregory, X. Wang, and D. Werner, "Matched impedance thin planar composite magneto-dielectric metasurfaces," *IEEE Transactions on Antennas and Propagation*, vol. 60, no. 4, pp. 1910–1920, Apr. 2012.
- [32] J. Bossard, X. Liang, L. Li, S. Yun, D. Werner, B. Weiner, T. Mayer, P. Cristman, A. Diaz, and I. Khoo, "Tunable frequency selective surfaces and negative-zero-positive index metamaterials based on liquid crystals," *IEEE Transactions on Antennas and Propagation*, vol. 56, no. 5, pp. 1308–1320, May 2008.
- [33] P. D. Potter, *A new horn antenna with suppressed sidelobes and equal bandwidths*. Jet Propulsion Laboratory, California Institute of Technology, 1963.

- [34] H. E. Bartlett and R. E. Moseley, "Dielguides - highly efficient low noise antenna feeds(antenna feed eliminating compromise between antenna illumination and spillover efficiencies by placing dielectric guiding structures between primary feed and reflector)," *Microwave Journal*, vol. 9, pp. 53–58, 1966.
- [35] P. J. B. Clarricoats, A. D. Olver, and M. Rizk, "A dielectric loaded conical feed with low cross-polar radiation," in *Proc. URSI Symp. on Electromagnetic Theory, Spain*, 1983, pp. 351–354.
- [36] E. Lier and J. A. Aas, "Simple hybrid mode horn feed loaded with a dielectric cone," *Electronics Letters*, vol. 21, no. 13, pp. 563–564, 1985.
- [37] E. Lier and T. Schaug-Pettersen, "The strip-loaded hybrid-mode feed horn," *Antennas and Propagation, IEEE Transactions on*, vol. 35, no. 9, pp. 1086–1089, 1987.
- [38] S. F. Mahmoud and M. Aly, "A new version of dielectric lined waveguide with low cross-polar radiation," *Antennas and Propagation, IEEE Transactions on*, vol. 35, no. 2, pp. 210–212, 1987.
- [39] E. Lier and A. Kishk, "A new class of dielectric-loaded hybrid-mode horn antennas with selective gain: design and analysis by single mode model and method of moments," *Antennas and Propagation, IEEE Transactions on*, vol. 53, no. 1, pp. 125–138, 2005.
- [40] G. M. Peace and E. E. Swartz, "Amplitude compensated horn antenna," *Microwave J*, vol. 7, no. 2, p. 66, 1964.
- [41] K. K. Chan and S. Rao, "An accurate model for rectangular trifurcated horns," *Antennas and Propagation, IEEE Transactions on*, vol. 55, no. 12, pp. 3706–3710, 2007.
- [42] E. Lier and R. K. Shaw, "Design and simulation of metamaterial-based hybrid-mode horn antennas," *Electronics Letters*, vol. 44, no. 25, pp. 1444–1445, 2008.
- [43] P.-S. Kildal, "Definition of artificially soft and hard surfaces for electromagnetic waves," *Electronics Letters*, vol. 24, no. 3, pp. 168–170, 1988.
- [44] —, "Artificially soft and hard surfaces in electromagnetics," *Antennas and Propagation, IEEE Transactions on*, vol. 38, no. 10, pp. 1537–1544, 1990.
- [45] E. Lier and P.-S. Kildal, "Soft and hard horn antennas," *Antennas and Propagation, IEEE Transactions on*, vol. 36, no. 8, pp. 1152–1157, 1988.
- [46] Q. Wu, C. Scarborough, D. Werner, E. Lier, and X. Wang, "Design synthesis of metasurfaces for broadband hybrid-mode horn antennas with enhanced radiation pattern and polarization characteristics," *IEEE Transactions on Antennas and Propagation*, vol. 60, no. 8, pp. 3594–3604, Aug. 2012.

- [47] C. Scarborough, Q. Wu, D. Werner, E. Lier, R. Shaw, and B. Martin, "Demonstration of an octave-bandwidth negligible-loss metamaterial horn antenna for satellite applications," *IEEE Transactions on Antennas and Propagation*, vol. 61, no. 3, pp. 1081–1088, Mar. 2013.
- [48] Q. Wu, C. Scarborough, B. Martin, R. Shaw, D. Werner, E. Lier, and X. Wang, "A ku-band dual polarization hybrid-mode horn antenna enabled by printed-circuit-board metasurfaces," *IEEE Transactions on Antennas and Propagation*, vol. 61, no. 3, pp. 1089–1098, Mar. 2013.
- [49] P. J. B. Claricoats and A. D. Oliver, *Corrugated horns for microwave antennas*. IET, 1984.
- [50] D. M. Pozar, *Microwave Engineering*, 2nd ed. Addison-Wesley, 1998.
- [51] M. Thumm, "Computer-aided analysis and design of corrugated TE<sub>11</sub> to HE<sub>11</sub> mode converters in highly overmoded waveguides," *Int J Infrared Milli Waves*, vol. 6, no. 7, pp. 577–597, Jul. 1985.
- [52] S. Maci, G. Minatti, M. Casaletti, and M. Bosiljevac, "Metasurfing: addressing waves on impenetrable metasurfaces," *IEEE Antennas and Wireless Propagation Letters*, vol. 10, pp. 1499–1502, 2011.
- [53] E. Lier, "Review of soft and hard horn antennas, including metamaterial-based hybrid-mode horns," *IEEE Antennas and Propagation Magazine*, vol. 52, no. 2, pp. 31–39, 2010.
- [54] W. Rotman, "Plasma simulation by artificial dielectrics and parallel-plate media," *IRE Transactions on Antennas and Propagation*, vol. 10, no. 1, pp. 82–95, 1962.
- [55] J. B. Pendry, A. J. Holden, D. J. Robbins, and W. J. Stewart, "Low frequency plasmons in thin-wire structures," *J. Phys.: Condens. Matter*, vol. 10, no. 22, p. 4785, Jun. 1998.
- [56] O. Luukkonen, C. R. Simovski, A. V. Raisanen, and S. A. Tretyakov, "An efficient and simple analytical model for analysis of propagation properties in impedance waveguides," *IEEE Transactions on Microwave Theory and Techniques*, vol. 56, no. 7, pp. 1624–1632, Jul. 2008.
- [57] G. L. James, "Design of wide-band compact corrugated horns," *IEEE Transactions on Antennas and Propagation*, vol. 32, no. 10, pp. 1134–1138, 1984.
- [58] G. H. Brown, "The turnstile antenna," *Electronics*, vol. 9, pp. 14–17, Apr. 1936.
- [59] M. Bolster, "A new type of circular polarizer using crossed dipoles," *IRE Transactions on Microwave Theory and Techniques*, vol. 9, no. 5, pp. 385–388, Sep. 1961.

- [60] R. F. Harrington, "Effect of antenna size on gain, bandwidth, and efficiency," *J. Res. Nat. Bur. Stand.*, vol. 64, no. 1, pp. 1–12, 1960.
- [61] R. Hansen, "Fundamental limitations in antennas," *Proceedings of the IEEE*, vol. 69, no. 2, pp. 170–182, Feb. 1981.
- [62] J. L. Volakis, C.-C. Chen, and K. Fujimoto, *Small Antennas*. New York: McGraw-Hill, 2010.
- [63] T. Spence and D. Werner, "A novel miniature broadband/multiband antenna based on an end-loaded planar open-sleeve dipole," *IEEE Transactions on Antennas and Propagation*, vol. 54, no. 12, pp. 3614–3620, Dec. 2006.
- [64] J. Ludwig, C. Cato, and S. Lim, "Design of an electrically small, circularly polarized planar cross dipole," in *2014 IEEE International Symposium on Antennas & Propagation and USNC/URSI National Radio Science Meeting*, Memphis, TN, Jul. 2014, pp. 287–288.
- [65] C. P. Scarborough, D. H. Werner, and D. E. Wolfe, "Low-profile metamaterial antenna with near-arbitrary tunable polarization," in *2014 IEEE International Symposium on Antennas & Propagation and USNC/URSI National Radio Science Meeting*, Memphis, TN, Jul. 2014, pp. 1451–1452.
- [66] P. de Maagt, R. Gonzalo, Y. C. Vardaxoglou, and J. -.-M. Baracco, "Electromagnetic bandgap antennas and components for microwave and (sub)millimeter wave applications," *IEEE Transactions on Antennas and Propagation*, vol. 51, no. 10, pp. 2667–2677, Oct. 2003.
- [67] M. G. Bray and D. Werner, "A broadband open-sleeve dipole antenna mounted above a tunable EBG AMC ground plane," in *2004 IEEE Antennas and Propagation Society International Symposium*, vol. 2, Jun. 2004, pp. 1147–1150.
- [68] M. Bray, Z. Bayraktar, and D. Werner, "GA optimized ultra-thin tunable EBG AMC surfaces," in *2006 IEEE Antennas and Propagation Society International Symposium*, Jul. 2006, pp. 410–413.
- [69] M. Bray and D. Werner, "Fast simulation of lumped-element loaded AMC antenna systems using embedded element theory," in *2010 IEEE Antennas and Propagation Society International Symposium*, 2010, pp. 1–4.
- [70] D. H. Werner, P. L. Werner, and M. J. Wilhelm, "High-selectivity electromagnetic bandgap device and antenna system," 7 042 419, U.S. Classification: 343/909, May 2006.
- [71] H.-J. Lee, K. Ford, and R. Langley, "Independently tunable low-profile dual-band high-impedance surface antenna system for applications in UHF band," *IEEE Transactions on Antennas and Propagation*, vol. 60, no. 9, pp. 4092–4101, Sep. 2012.

- [72] S. Martin, D. H. Werner, M. Bray, E. Lier, and B. Cleaveland, "Versatile design technique for customizable electromagnetic band gap structures," in *2012 IEEE Antennas and Propagation Society International Symposium (APSURSI)*, Jul. 2012, pp. 1–2.
- [73] S. Martin, I. Martinez, J. Turpin, D. Werner, E. Lier, and M. Bray, "The synthesis of wide- and multi-bandgap electromagnetic surfaces with finite size and nonuniform capacitive loading," *IEEE Transactions on Microwave Theory and Techniques*, vol. 62, no. 9, pp. 1962–1972, Sep. 2014.



# Publications

In addition to the following publications, at least two journal articles are being prepared for submission based on the tunable ELD and AMC work described here.

## Journal Articles

- [1] E. Lier, D. H. Werner, C. P. Scarborough, Q. Wu, and J. A. Bossard, "An octave-bandwidth negligible-loss radiofrequency metamaterial," *Nature Materials*, vol. 10, no. 3, pp. 216–222, Jan. 2011.
- [2] Q. Wu, C. Scarborough, D. Werner, E. Lier, and X. Wang, "Design synthesis of metasurfaces for broadband hybrid-mode horn antennas with enhanced radiation pattern and polarization characteristics," *IEEE Transactions on Antennas and Propagation*, vol. 60, no. 8, pp. 3594–3604, Aug. 2012.
- [3] C. P. Scarborough, Z. H. Jiang, D. H. Werner, C. Rivero-Balcine, and C. Drake, "Experimental demonstration of an isotropic metamaterial super lens with negative unity permeability at 8.5mhz," *Applied Physics Letters*, vol. 101, no. 1, pp. 014 101–014 103, Jul. 2012.
- [4] Q. Wu, C. Scarborough, B. Martin, R. Shaw, D. Werner, E. Lier, and X. Wang, "A ku-band dual polarization hybrid-mode horn antenna enabled by printed-circuit-board metasurfaces," *IEEE Transactions on Antennas and Propagation*, vol. 61, no. 3, pp. 1089–1098, Mar. 2013.

- [5] C. Scarborough, Q. Wu, D. Werner, E. Lier, R. Shaw, and B. Martin, "Demonstration of an octave-bandwidth negligible-loss metamaterial horn antenna for satellite applications," *IEEE Transactions on Antennas and Propagation*, vol. 61, no. 3, pp. 1081–1088, Mar. 2013.
- [6] Q. Wu, C. Scarborough, D. Werner, E. Lier, and R. Shaw, "Inhomogeneous metasurfaces with engineered dispersion for broadband hybrid-mode horn antennas," *IEEE Transactions on Antennas and Propagation*, vol. 61, no. 10, pp. 4947–4956, Oct. 2013.

## Conference Proceedings

- [7] C. P. Scarborough, Q. Wu, M. D. Gregory, D. H. Werner, R. K. Shaw, and E. Lier, "Broadband metamaterial soft-surface horn antennas," in *Antennas and Propagation Society International Symposium (APSURSI), 2010 IEEE, 2010*, pp. 1–4.
- [8] Q. Wu, C. P. Scarborough, M. D. Gregory, D. H. Werner, R. K. Shaw, and E. Lier, "Broadband metamaterial-enabled hybrid-mode horn antennas," in *Antennas and Propagation Society International Symposium (APSURSI), 2010 IEEE, 2010*, pp. 1–4.
- [9] E. Lier, R. K. Shaw, D. H. Werner, Q. Wu, C. P. Scarborough, and M. D. Gregory, "Status on meta-horn development-theory and experiments," in *Antennas and Propagation Society International Symposium (APSURSI), 2010 IEEE, 2010*, pp. 1–4.
- [10] C. Scarborough, Q. Wu, D. Werner, E. Lier, B. Martin, and R. Shaw, "A square dual polarization metahorn design," in *2011 IEEE International Symposium on Antennas and Propagation (APSURSI), 2011*, pp. 1065–1068.
- [11] Z. H. Jiang, C. Scarborough, D. Werner, P. Werner, C. Rivero-Balcine, and C. Drake, "An isotropic 8.5 MHz magnetic meta-lens," in *2011 IEEE International Symposium on Antennas and Propagation (APSURSI), 2011*, pp. 1151–1154.

- [12] E. Lier, B. Martin, R. Shaw, S. Yang, D. H. Werner, Q. Wu, and C. P. Scarborough, "Demonstration of soft meta-horn with printed circuit board (PCB) wall liners," Spokane, WA USA, Jul. 2011.
- [13] Q. Wu, C. Scarborough, D. Werner, E. Lier, and R. Shaw, "A broadband soft horn antenna with inhomogeneous metasurface coatings," in *2012 IEEE Antennas and Propagation Society International Symposium (APSURSI)*, 2012, pp. 1–2.
- [14] D. Werner, Z. H. Jiang, C. P. Scarborough, Q. Wu, M. D. Gregory, and J. P. Turpin, "Broadband low-loss metamaterial-enabled devices," Baltimore, MD, USA, May 2012.
- [15] D. H. Werner, Z. H. Jiang, J. P. Turpin, C. P. Scarborough, M. D. Gregory, Q. Wu, and P. L. Werner, "Broadband low-loss metamaterial-enabled antennas," Bordeaux, France, Sep. 2013.
- [16] C. P. Scarborough, D. H. Werner, and D. E. Wolfe, "Miniaturized tunable metamaterial antenna design and modeling in the low UHF band," Orlando, FL, USA, Jul. 2013.
- [17] J. A. Bossard, C. P. Scarborough, Q. Wu, D. H. Werner, and P. L. Werner, "High-power considerations in metamaterial antennas," in *2014 IEEE International Symposium on Antennas & Propagation and USNC/URSI National Radio Science Meeting*, Memphis, TN, Jul. 2014, pp. 539–540.
- [18] C. P. Scarborough, D. H. Werner, and D. E. Wolfe, "Low-profile metamaterial antenna with near-arbitrary tunable polarization," in *2014 IEEE International Symposium on Antennas & Propagation and USNC/URSI National Radio Science Meeting*, Memphis, TN, Jul. 2014, pp. 1451–1452.
- [19] K. L. Morgan, C. P. Scarborough, M. D. Gregory, D. H. Werner, and P. L. Werner, "Metasurface with reconfigurable reflection phase for high-power microwave applications," in *2014 IEEE International Symposium on Antennas & Propagation and USNC/URSI National Radio Science Meeting*, Memphis, TN, Jul. 2014, pp. 1230–1231.

## **Vita**

### **Clinton Post Scarborough**

#### **Education**

M.S. Electrical Engineering, Specializing in Electromagnetics - August 2011  
The Pennsylvania State University Graduate School - University Park, PA  
Thesis: Low-loss Radio-frequency Electromagnetic Metamaterials Applied to Antennas and Imaging  
Advisor: Dr. Douglas Werner

B.S. Electrical Engineering, Minor in Mathematics - May 2009  
Grove City College - Grove City, PA  
Summa Cum Laude, Highest Honors in Electrical Engineering  
Advisor: Dr. Frank Duda

#### **Awards**

- 2014 IEEE Antennas and Propagation Society Harold A. Wheeler Applications Prize Paper Award
- 2014 Pontano Family Scholarship in Electrical Engineering
- 2014 Joseph R. and Janice M. Monkowski Graduate Fellowship in Electrical Engineering
- 2013 Luther B. and Patricia A. Brown Graduate Fellowship in Electrical Engineering
- 2012 James R. and Barbara R. Palmer Graduate Fellowship in Electrical Engineering
- 2011 Society of Penn State Electrical Engineers (SPSEE) Graduate Fellowship
- 2011 Anthony J. Ferraro Graduate Research Award, Electrical Engineering
- 2010 Paul F. Anderson Graduate Fellowship in Electrical Engineering
- Applied Research Laboratory (ARL) Exploratory and Foundational (E&F) Graduate Fellow
- Grove City College Scroll and Key Academic Honor Society
- Grove City College Dean's List

## **Distribution List**

- (a) Applied Research Laboratory  
The Pennsylvania State University  
Attn: Dr. Douglas E. Wolfe  
PO Box 30  
University Park, PA 16804  
Email: [dew125@arl.psu.edu](mailto:dew125@arl.psu.edu)
  
- (b) Defense Technical Information Center (DTIC)  
Attn: DTIC-BSC  
8725 John J. Kingman Road, Suite 0944  
Fort Belvoir, VA 22060-0944  
Email: [TR@dtic.mil](mailto:TR@dtic.mil)
  
- (c) The Pennsylvania State University  
Attn: Douglas H. Werner  
0121 Electrical Engineering East  
Dept. of Electrical Engineering  
University Park, PA 16802  
Email: [dhw@psu.edu](mailto:dhw@psu.edu)